TAILORING LIGHT FOR RAMAN MICROSPECTROSCOPY

DIPL.-PHYS. SVEN DOBNER

Inaugural-Dissertation
zur Erlangung des Doktorgrades
der Naturwissenschaften im Fachbereich Physik
der Mathematisch-Naturwissenschaftlichen Fakultät
der Westfälischen Wilhelms-Universität Münster

June 16, 2014

Westfälische
Wilhelms-Universität
Münster

Parts of this work have been published elsewhere (see list of publications).

Dekan:	Prof. Dr. Markus Donath
Erster Gutachter:	Prof. Dr. Carsten Fallnich
Zweiter Gutachter:	Prof. Dr. Klaus Boller
Tag der Prüfung:	11.4.2014
Tag der Promotion:	11.4.2014

ABSTRACT

This thesis is about the development of coherent Raman scattering techniques to be applied to microspectroscopy and an associated development of a specialized light source. The light source is designed to deliver pulses with sufficient power to efficiently generate a nonlinear Raman response, which was exploited as a contrast mechanism for microscopy, at a high repetition frequency for fast signal acquisition. Indeed current broad-bandwidth femtosecond stimulated Raman scattering (FSRS) spectroscopy methods allow the extraction of the full Raman spectrum, but are still limited in sensitivity and thus speed. Rectifying this drawback, the here presented novel interferometric advancements in FSRS, by the means of a Sagnac interferometer (iFSRS) or an in-line interferometer (II-FSRS), not only increase the sensitivity of the scheme, but also grant access to spectral phase information. These improvements of the spectroscopic scheme in combination with the highly adapted light source enable the acquisition of hyperspectral images, applicable to a wide range of questions in the life-sciences.

ZUSAMMENFASSUNG

Ziel dieser Arbeit ist die Weiterentwicklung einer kohärenten Raman Spektroskopiemethode für die Anwendung in der mikroskopischen Bildgebung und eine damit verbundene Entwicklung einer spezialisierten Lichtquelle. Die Lichtquelle wurde konzipiert, um mit einer hohen Impulsleistung effizient nichtlineare Prozesse treiben zu können und die erzeugten Signale gleichzeitig mit einer hohen Wiederholrate aufzunehmen. Besonders geeignet für die Anwendung in der mikroskopischen Bildgebung ist die kohärente Ramanstreuung, da sie einen chemisch selektiven Kontrast erzeugt. Bisherige breitbandige Ansätze um zu jedem Bildpunkt die vollständige spektrale Information zu extrahieren sind allerdings limitiert in ihrer Sensitivität und damit in ihrer Geschwindigkeit. Die neue interferometrische Erweiterung von Femtosekunden stimulierter Ramanstreuung (FSRS) mithilfe eines Sagnac-Interferometers (iFSRS), beziehungsweise eines kollinearen Interferometers (II-FSRS) erhöht nicht nur deren Sensitivität, sondern ermöglicht nun auch den Zugriff auf spektrale Phaseninformationen. Insgesamt zeigt das entwickelte Gesamtkonzept eine vielversprechende Anwendbarkeit, um vielfältige Fragestellungen in den Lebenswissenschaften zu untersuchen.

CONTENTS

1 MOTIVATION 1

2 LIGHT SOURCE 5
- 2.1 Master Oscillator and Power Amplifier System . . . 7
  - 2.1.1 Master Oscillator . . . 7
  - 2.1.2 Chirped Pulse Amplification . . . 9
  - 2.1.3 Pulse Shaping . . . 14
- 2.2 Broad-Bandwidth Supercontinuum Generation . . . 17
  - 2.2.1 Experimental Considerations . . . 19
  - 2.2.2 Parameter Study in Various Laser Host Materials . . . 20
- 2.3 Narrow-Bandwidth Optical Parametric Amplifiers . . . 23
  - 2.3.1 Periodically Poled Lithium Niobate . . . 23
  - 2.3.2 Silver Thiogallate . . . 25
  - 2.3.3 Lithium Indium Selenide . . . 26
- 2.4 Further Development and Applications . . . 28

3 RAMAN SCATTERING SPECTROSCOPY 31
- 3.1 Spontaneous Raman Scattering . . . 34
- 3.2 Femtosecond Raman-Induced Kerr-Effect Spectroscopy . . . 35
- 3.3 Femtosecond Stimulated Raman Scattering . . . 37
- 3.4 Discussion about the Applicability to Microscopy . . . 39

4 INTERFEROMETRIC COHERENT RAMAN SCATTERING 41
- 4.1 Interferometric Femtosecond Stimulated Raman Scattering . . . 42
  - 4.1.1 Working Principle, Experimental Setup and Model . . . 43
  - 4.1.2 Experimental Results . . . 46
- 4.2 In-line Interferometric Femtosecond Stimulated Raman Scattering 49
  - 4.2.1 Experimental Setup . . . 50
  - 4.2.2 Working Principle and Model . . . 51
  - 4.2.3 Experimental Results . . . 55
- 4.3 Hyperspectral Imaging . . . 59
  - 4.3.1 Experimental Microspectroscopy Setup . . . 61
  - 4.3.2 Experimental Results . . . 63
- 4.4 Current Limitations and Further Improvements . . . 67
- 4.5 Summary and Conclusion . . . 68

5 SUMMARY OF THE THESIS 71

ACKNOWLEDGEMENTS 75

BIBLIOGRAPHY 77

LIST OF PUBLICATIONS 91

1 MOTIVATION

The microscopic observation of samples is of fundamental interest in a wide range of scientific disciplines ranging from biology to medicine. Although the highest spatial resolution is achievable with an electron microscope or an atomic force microscope, these have the drawback to work either only in vacuum or on surfaces of a sample. Microscopy based on light exhibits only a spatial resolution in the range of hundreds of nanometers [1], but is almost universally applicable. The contrast mechanism in every microscopic study determines the degree of discriminability of different constituents within the sample. Simply exploitable contrasts within light microscopy are for example based on a change of the optical density or reflectivity, but the possibility for an identification of ingredients in a sample is limited. In comparison, spectroscopy in general describes a method, which is used to observe and detect the absorbed or emitted electromagnetic radiation of a sample under investigation in order to gain a detailed insight into its chemical and molecular composition and thus enables a chemical specificity. Combined with a microscope, spectroscopic methods allow for the determination of the spatial distribution of the diverse constituents in a sample, whereat this combination is also called microspectroscopy [2, 3]. There is a huge variety of different types of optical spectroscopy, ranging from simple absorption [4] or scattering measurements, over ellipsometry [5] to fluorescence spectroscopy [6], all applicable in spectral ranges from x-ray and ultraviolet radiation over the visible to the infrared or even the terahertz spectral range.

A special type of spectroscopy, which is particularly interesting for biological applications, namely the Raman scattering spectroscopy, makes use of the inelastic scattering of photons on vibrational resonances of molecules [7]. Here, the deposition of energy and thus the probability of an optically induced damage on the sample is minimal, compared to e. g. direct absorption spectroscopy with ultraviolet radiation. For Raman scattering experiments, light sources with a wavelength located in the visible and infrared region are of particular interest, because here, most materials exhibit a high degree of transparency and a low susceptibility towards damage, as long as the intensity is low enough, not to induce any multi-photon ionization. In spontaneous Raman scattering spectroscopy, typically a continuous-wave laser in the visible spectral region is used to excite the vibrational states of molecules, and the spontaneously scattered, frequency-shifted photons are detected [8]. The spectral characteristics of the scattering medium, related to the multitude of molecular bonds with their individual resonances, are imprinted onto the detected light field. The resulting Raman spectrum allows for an identification of the involved molecules

and gives rise to a high chemical specificity [9]. In order to implement spontaneous Raman scattering as a contrast mechanism into microscopy, the incident laser needs to be scanned across the sample, and for three-dimensional imaging the detection of the spectrum needs to be performed confocally point by point within the volume. In this way, so called hyperspectral images can be acquired, in which every spatially scanned point contains its full spectroscopic information [10]. A limiting factor however, is the low scattering cross-section and the low signal yield, which results in an acquisition time in the order of seconds per scanned point.

Nevertheless, this drawback can be resolved by a nonlinear excitation of a transition. In general, nonlinear spectroscopy is recognized as a powerful tool to overcome the limitations set by Doppler broadening or to use multiphoton processes to excite atomic or molecular transitions [11, 12, 13, 14]. Since about two decades, nonlinear spectroscopy has thus gained importance in biomedical research, to access vibrational resonances via multiphoton excitation for imaging, as in coherent anti-Stokes Raman scattering (CARS [15, 16]) or stimulated Raman scattering (SRS [17, 18]). These narrow-bandwidth coherent Raman scattering (CRS) techniques usually are probing a spectrally narrow portion of the imaginary part of the material's third-order nonlinear susceptibility $\chi^{(3)}$ with two synchronous narrow-bandwidth pulses. In order to change this contrast to another spectral portion, meaning another Raman resonance, one of the driving lasers needs to be tuned in its central wavelength in order to acquire so called multi-spectral images [19].

As an alternative, if one of the two involved pulses is a broad-bandwidth femtosecond pulse, it stimulates all Raman resonances within its bandwidth simultaneously. This is exploited either with SRS resulting in the so-called femtosecond stimulated Raman scattering (FSRS [20]) or with the Raman-induced Kerr-effect, which is called femtosecond Raman-induced Kerr-effect spectroscopy (FRIKES [21, 22]). These broad-bandwidth CRS schemes are of particular interest, because they allow – in principle – for the acquisition of hyperspectral images, i. e. images containing the full spectroscopic information as it is the case with spontaneous Raman scattering [23]. Additionally, the application of a femtosecond probe pulse enhances the signal generation, because in this case the peak power is considerably higher, compared to the picosecond probe pulse used in narrow-bandwidth CRS schemes.

All these CRS techniques require a highly adapted light source that satisfies various demands: due to the nonlinear nature of the light-matter interaction, a pulsed operation of the light source is favorable. A high peak power in the order of kilowatt, owing to a short pulse duration in the order of picoseconds, is desired for an efficiently induced nonlinearity. A careful balance between average power and peak power allows to avoid optically induced damage in the sample. Additionally, the CRS schemes require a second synchronous pulse, which

either needs to be of narrow bandwidth with a tunable central wavelength or of broad bandwidth. The scope of this thesis is to present the development of the combination of a highly adapted light source and a specialized spectroscopic scheme to generate a molecular specific contrast for the application to microscopic imaging. All requirements for CRS measurement schemes are addressed in Chap. 2 and fulfilled with the master oscillator power amplifier system (Sec. 2.1), the subsequent generation of a broad-bandwidth supercontinuum (Sec. 2.2) and the development of narrow-bandwidth optical parametric amplifiers (Sec. 2.3).

In Chap. 3 different existing broad-bandwidth CRS schemes were experimentally implemented and compared to one another in order to investigate their individual suitability for the application to hyperspectral imaging. Independent of the applied light source, there are certain constrains with the different schemes (Sec. 3.4). Consequently, Chap. 4 is focused on the advancement of FSRS through the implementation of purely optical interferometric approaches in order to enhance the sensitivity and to extract even more information from the stimulated Raman interaction: interferometric FSRS (iFSRS, Sec. 4.1) employs an unbalanced Sagnac interferometer and achieved an unprecedented background reduction of 17 dB over a broad bandwidth of 60 THz (2000 cm^{-1}), resulting in a significant increase in sensitivity. Apart from raising the signal-to-background ratio in the measurement of the Raman intensity spectrum, this interferometric method granted access to the spectral phase of the resonant $\chi^{(3)}$ contribution. The spectral phase became apparent as a dispersive lineshape and was reproduced numerically with a simple oscillator model. With in-line interferometric femtosecond stimulated Raman scattering (II-FSRS, Sec. 4.2), another new method to measure the spectral Raman intensity and phase over a broad spectral range has been introduced. Also here, an analytic model is developed, that excellently reproduced the measured spectra. Additionally, the performance of II-FSRS is directly compared in experiments to two established techniques, namely FSRS and FRIKES. The consequential application of this broad-bandwidth CRS method to imaging is presented in Sec. 4.3 and allows for the measurement of hyperspectral images.

2 LIGHT SOURCE

CONTENTS

2.1 Master Oscillator and Power Amplifier System 7
2.1.1 Master Oscillator 7
2.1.2 Chirped Pulse Amplification 9
2.1.3 Pulse Shaping 14
2.2 Broad-Bandwidth Supercontinuum Generation 17
2.2.1 Experimental Considerations 19
2.2.2 Parameter Study in Various Laser Host Materials 20
2.3 Narrow-Bandwidth Optical Parametric Amplifiers 23
2.3.1 Periodically Poled Lithium Niobate 23
2.3.2 Silver Thiogallate 25
2.3.3 Lithium Indium Selenide 26
2.4 Further Development and Applications 28

This chapter introduces the light source that has been designed to be applied for coherent Raman scattering (CRS) methods combined with microscopy, as presented in Chap. 3 and Chap. 4. These methods impose several requirements for the light source: one of the most important premises is a pulsed operation of the light source, as all later exploited effects are nonlinear, so the efficiency scales with the peak power of the applied light field. Additionally, a stable train of pulses is required, because in general noise is undesired and the acquisition of the Raman signal is realized in recording subsequent pulse interactions, such that fluctuations would distort the signal, especially when the signal amplitude is small.

For the application of the generated pulses to nonlinear microscopy two contradictory traits, namely the repetition frequency and the peak power, should be balanced, because they dictate the efficiency of the nonlinear signal yield. Fig. 1 shows a sketch, which illustrates two major limitations that need to be considered for balancing the efficiency of the signal generation (scales quadratic to the pulse energy) and the frequency of a generated signal (proportional to the repetition frequency of the light source) depending on the applicable pulse energy and the repetition frequency. On the one hand, a high repetition frequency is favored for a frequent signal generation. However, the thermal impact through heat accumulation by absorption in the sample under investigation impairs especially rather delicate biological samples [24, 25], suggesting the application of a reduced repetition frequency. In the later presented microscopic setup, us-

ing a microscope objective with a numerical aperture of 0.6, optically induced thermal damage in samples became visible by applying continuous-wave radiation with an average power of about 10 mW. Consequently, common oscillator systems that emit pulses with a repetition frequency of about 40 to 100 MHz [26] are limited in the applicable pulse energy to about 100 to 250 pJ, which is highlighted with a green rectangle in Fig. 1. On the other hand, the generated nonlinear signal power scales quadratically with the peak power of the applied pulses, such that a high pulse energy and a short pulse duration are desired. As will be shown later, the pulse duration of about one picosecond is optimal for the stimulation of Raman transitions. With this pulse duration, the critical power density of about $10^{11}\,\mathrm{W/cm^2}$ [27] for nonlinear destructive effects like multi-photon ionization is reached at a pulse energy of about 10 nJ, again assuming a microscope objective with a numerical aperture of 0.6, independently of the repetition frequency. This pulse energy is commonly available and far exceeded with laser systems exhibiting a low repetition frequency in the range of kilohertz, like regenerative amplifiers [28, 29, 30], which is also marked with a green rectangle in Fig. 1. With these systems nonlinear signals can easily be generated, but only at a low repetition frequency. In order to level the aforementioned issues, the laser system should feature a mediocre repetition frequency and moderate pulse energy, but such a system is not commercially available. The exact optimal operation point strongly depends on the individual sample under investigation, in terms of whether the thermal or nonlinear damage threshold is reached first. An operation at a repetition frequency of about 1 MHz poses a promising balance in this context.

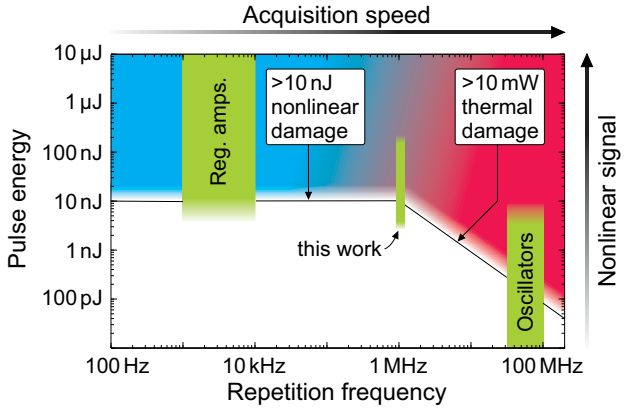

Figure 1: Limitations of the applicable pulse energy depending on the repetition frequency, by applying a pulse with a duration of 1 ps and focusing optics with a numerical aperture of 0.6. For details see text.

A further prerequisite for the application to CRS is the generation of a stable and synchronous second pulse, that needs to be tunable in its central wavelength for the narrow-bandwidth CRS schemes. This is commonly done by electronic stabilization of two independent oscillator systems [31], by synchronous

pumping of an optical parametric oscillator [32, 33, 34], or by subharmonically synchronized oscillators [18]. Apart from the aforementioned limitation of the low pulse energy available with these high repetition frequency systems, these systems are rather complex. In contrast, regenerative amplifier systems provide sufficient pulse energy to perform nonlinear frequency conversion in optical parametric amplifiers rather easily, the application of the generated slowly repeating pulses is undesired in spectroscopic schemes, because it would result in tremendous averaging times if the noise of a single shot measurement is too dominant [23]. A solution to the addressed issues is presented in this thesis with the concept of a unique custom-build light source: one primary oscillator is used from which all required pulses are derived from all-optical techniques, via amplification and nonlinear frequency conversion. Consequently, all pulses are intrinsically synchronized to one another, with a precision that is only limited by the mechanical stability of the experimental setup.

The fundamental master oscillator and power amplifier (MOPA) is presented in Sec. 2.1[1] and consists of an all-normal-dispersion femtosecond fiber laser (Sec. 2.1.1), followed by a chirped pulse amplifier (Sec. 2.1.2). Due to linear as well as nonlinear distortions within the amplification process, the pulses need to be shaped in their spectral phase (Sec. 2.1.3), so that they possess sufficient peak power not only for the application to CRS, but also to drive the generation of broad-bandwidth supercontinua in bulk media, as shown in Sec. 2.2[2]. The supercontinua are excellently suited to seed optical parametric processes in nonlinear crystals, which will be presented in Sec. 2.3[3]. As a conclusion of this chapter, Sec. 2.4 discusses further developments of the light source and the applicability of the broad-bandwidth supercontinuum pulses together with the MOPA pulses for the coherent Raman scattering experiments presented in the later Chap. 3 and Chap. 4.

2.1 MASTER OSCILLATOR AND POWER AMPLIFIER SYSTEM

2.1.1 Master Oscillator

The first constituent of the light source is the master oscillator, which dictates the general pulse characteristics and stability of the whole system. The concept of the master oscillator was adapted from Chong et al., who presented a passively mode-locked Ytterbium-doped fiber laser with a rather simple setup [38]

1 Parts of the experiments in this section have been performed in collaboration with Gerrit L. Hölscher in the frame of his Diploma thesis [35].

2 Markus Fischedick conducted parts of the presented experiments in the frame of his Bachelor thesis [36].

3 Gerrit L. Hölscher [35] and Christian Egelkamp [37] contributed to the work presented in this section through an experimental realization of optical parametric amplifiers in the frame of their Diploma and Bachelor thesis, respectively.

as it is shown in Fig. 2 (a). It operates in an all-normal dispersion regime, without the need to balance the cavity dispersion with anomalous dispersive elements like prisms [39], diffraction gratings [40] or chirped mirrors [41]. The mode-locking mechanism in this all-normal dispersion (ANDi) femtosecond fiber laser is based on nonlinear effects resulting in nonlinear polarization evolution (NPE), while an additional frequency filter induces self-amplitude modulation and stabilizes the mode-locked operation [42]. Due to the large normal dispersion of the cavity, the output pulses are highly chirped, but can be dechirped down to < 200 fs [43], while still containing high pulse energies of more than 10 nJ [44].

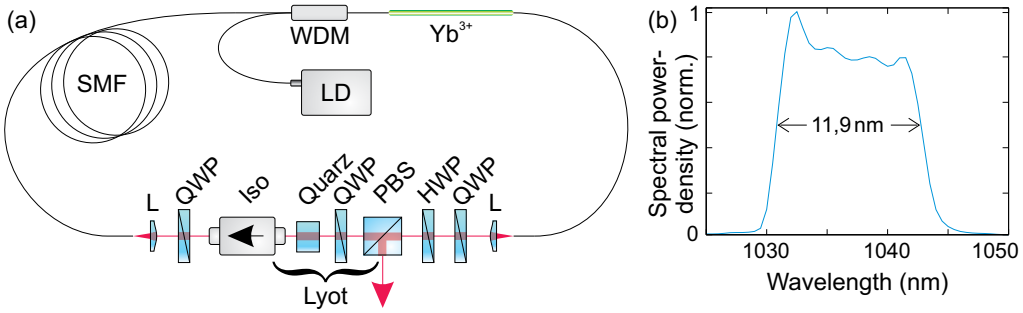

Figure 2: (a) Experimental setup of the all-normal dispersion fiber laser, comprised of a fiber part with about 10 m single-mode fiber (SMF), a wavelength division multiplexer (WDM), which couples light from a pump laser diode (LD) into the cavity to pump the active Ytterbium-doped fiber (Yb^{+3}). The free-space part includes quarter- and half-wave plates (QWP and HWP), a polarizing beam-splitter (PBS), a quarz plate (Quarz), collimating optics (L) and a free-space isolator (Iso). (b) Optical spectrum as a function of the wavelength from the output port of the PBS. For details see text.

The ANDi fiber laser (Fig. 2 (a)) consisted of a fully single-mode fiber part with a total length of approximately 10 m and a free space part of about 40 cm in length, which resulted in a measured cavity round trip time of about 50 ns. The central element within the fiber segment was the 30 cm long Ytterbium-doped fiber (LIEKKI Yb1200-4/125), which was pumped by a 976 nm laser diode in co-propagating direction via a fiber-based wavelength division multiplexer (WDM). The residual fiber part was comprised of a standard single-mode fiber (Corning Hi1060 flex), dominantly contributing to the large normal dispersion of the cavity. The free-space part included a quarter-wave plate (QWP), a half-wave plate (HWP) and a polarizing beamsplitter (PBS), which were necessary for the NPE mode-locking mechanism. A polarization-dependent optical isolator ensured an unidirectional lasing operation. A quartz plate in-between the two polarizing elements, namely PBS and isolator, formed a Lyot filter [45] that showed a sinusoidally modulated spectral transmission, which enhanced the self-amplitude modulation, as explained before. The included quarter-wave plate enabled a tuneability of the frequency filter and thus the tuning of the cen-

tral frequency of the laser. A third quarter-wave plate was used to adjust the ellipticity of the pulse polarization in the course of the transit through the fiber segment. An elliptical state of polarization was essential to allow for nonlinear polarization rotation, especially where the nonlinearity was highest, i. e. where the pulse peak power is highest within the resonator. The pulse contained the most energy in the fiber segment directly after the active fiber and therewith dominantly induced nonlinear effects at this point. In order to balance the nonlinearity, dispersion and out-coupling ratio per round-trip, the pump power and the orientation of the waveplates were adjusted for a stable pulsed operation.

Stable mode-locked operation was achieved with a pump power of about 440 mW and yielded 86.2 mW of average output power exiting from the PBS. Prorated with the measured repetition frequency of 20.013 MHz, one pulse contained 4.3 nJ pulse energy. The root mean square (RMS) pulse-to-pulse fluctuations amounted to less than 0.5 % and this highly stable operation was maintained over weeks, as long as the ambient conditions stayed constant. Especially the temperature seemed to affect the oscillator performance considerably, either by altering the free-space alignment or inducing refractive index changes in the long fiber part. Consequently, the whole setup was placed in an actively temperature stabilized box, which ensured a long term deviation of less than $\pm 1°$, as against $\pm 3°$ in the laboratory.

The output spectrum in Fig. 2 (b) is plotted against the wavelength and shows a full width at half maximum (FWHM) of 11.9 nm. It supports a bandwidth limited pulse duration of 175 fs, but the pulses are known to be chirped to a few picoseconds [38], due to the all-normal dispersion components in the oscillator. The exact duration is of minor interest at this point, as related to the unintended nonlinear effects with a subsequent fiber-based amplification, the pulses were dispersed even more during the applied CPA scheme.

2.1.2 Chirped Pulse Amplification

The power of the master oscillator was scaled by connecting an amplifier chain in series. In order to reach the desired repetition frequency of 1 MHz and for an efficient enhancement of the pulse energy, the repetition frequency of the pulse-train was reduced by means of an acousto-optic modulator (AOM), as schematically shown in Fig. 3 (b). Every twentieth pulse was diffracted into the first order by an acoustically induced Bragg-grating in a quarz-crystal. The measured average power of 3.08 mW in the first order at a repetition frequency of 1 MHz revealed a diffraction efficiency of more than 70 %.

Within the amplification process, the pulse energy and consequently the peak power was drastically increased. A measurement of the duration of the oscillator pulses was unsuccessful, but assuming a duration of 1.5 ps, as it was ob-

served in [38, 46], the pulses that emerged from the oscillator still possessed a peak power of almost 2 kW. This power level was sufficient to evoke nonlinearities like self-phase modulation (SPM [47]) or nonlinear polarization rotation (NPR [48]) in a standard single-mode fiber, even without any amplification. While these effects were necessary for the mode-locking mechanism for the fiber laser, they were undesired in the amplification process. The induced nonlinear phase shift could not be compensated for within a simple compressor. To minimize the occurrence of nonlinear effects in the first place, the pulses were highly dispersed, so the peak power was considerably reduced, before the amplification process, meaning the chirped pulse amplification (CPA [49]) scheme was applied.

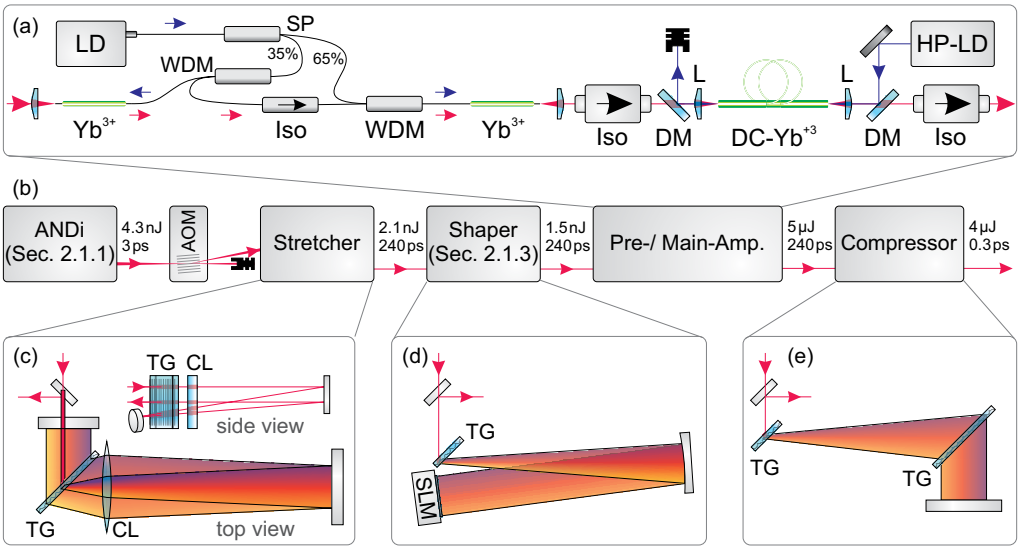

Figure 3: Schematic experimental setup of (a) the pre- and main-amplifier, (b) the MOPA-system, (c) the pulse-stretcher, (d) the pulse shaper and (e) the pulse-compressor. LD: pump laser diode, SP: splitter, WDM: wavelength division multiplexer, Iso: optical isolator, Yb^{+3}: Ytterbium-doped single-mode fiber, DC-Yb^{+3}: Ytterbium-doped double-clad fiber, DM: dichroic mirror, L: collimator lens, HP-LD: high-power pump laser diode, AOM: acousto-optic modulator, TG: transmission grating, CL: cylindrical lens, SLM: spatial light modulator. For details, see text.

A folded Martinez-type grating stretcher was built to increase the duration of the master oscillator pulses to more than 200 ps, as will be shown at the end of this section. Details of the working principle and design of this stretcher can be found in [50]. A schematic sketch of the stretcher is shown in Fig. 3 (c). Its key element was a transmission grating with a grating period of 1200 lines per millimeter (from Wasatch Photonics). The incident light beam was diffracted at an angle of 68 ° and spatially dispersed. Right after the grating, a cylindrical lens with a focal length of 300 mm was placed, followed by a mirror in its focal distance. It reflected the light back through the lens and the grating under

a small vertical angle, creating a spatial offset, which is depicted in the side view in Fig. 3 (c). A second mirror placed below the incident beam behind the grating, sent the light back the whole way, also with a slight spatial offset to be separated from the incident beam. In total, this assembly induced normal dispersion onto the pulse, which reduced the peak power more than 1200-fold, compared to the theoretical Fourier limit. The transmission through the whole stretcher was 68 % leaving 2.08 mW of average power.

The stretcher was followed by a pulse shaper, which will be used to make up for distortions of the pulse within the amplification process. Although a CPA scheme was applied, the peak power of the pulses was still sufficient to introduce undesired nonlinear effects. Together with dispersion of higher order, these were not compensable with a standard grating compressor, which was responsible for the recompression of the amplified pulses, as shown later. While here the experimental setup is presented, the detailed treatment of the shaper and its effect will be presented in Sec. 2.1.3. The setup of the shaper followed a standard design [51] and used a transmission grating of identical construction as in the stretcher. A spherical gold mirror was placed with a slight horizontal tilt in the distance of its focal length of 300 mm with respect to the grating and by that generated a Fourier plane right next to the grating. A one-dimensional spatial light modulator (SLM, Type 1x12,288 Linear Series from Boulder Nonlinear Systems) was placed in this plane, so that the spatially dispersed frequency components of the pulse illuminated individual pixels of the SLM. The pixelation of the liquid crystal is a result of narrow segments of electrodes, where a potential of ± 5 V can be applied individually, via a PC-driven controller. The liquid crystals change their orientation and by that their birefringence properties determined by the applied voltage. Choosing the correct polarization of the incident light, in this case p-polarized, the phase of the light was manipulated individually at every pixel and by that for every frequency component separately. The SLM works in reflection mode and induced a small spatial separation through a slight vertical tilt, so the exiting beam could be separated with a mirror placed below the incident beam. In this 4-f arrangement, the shaper itself did not induce any dispersion onto the pulse, only the phase induced by the SLM was impregnated onto the pulse. An average power of 1.46 mW (70 %) was transmitted through the shaper in total, so from the pulse energy extracted from the ANDi-oscillator of 4.3 nJ, there were 1.46 nJ (34 %) available as a seed for the amplification chain.

The stretched and shaped pulses were coupled into a pre-amplifier which was constructed using single-mode fibers only, as shown in Fig. 3 (a). The first active fiber segment with a length of 30 cm was pumped by a split portion of 35 % of a fiber-coupled pump diode with a central wavelength of 976 nm. It was merged with the pulses using a filter WDM in counter-propagating direction, resulting in an efficient amplification, while keeping the parasitic amplified

spontaneous emission (ASE) at a low level. At this point, the amplified signal was low enough, not to damage the rather delicate filter WDM, which in turn allowed for a high isolation against the signal light in this counter-propagating direction. The second active fiber was pumped with the residual 65 % of the pump light, now in co-propagating direction, combined with the signal with a fused WDM. This fused WDM withstood a higher power than the filter WDM, but possessed a much lower isolation for the amplified light, which – from experience – was not sufficient to avoid a damage to the pump diode if it was installed in a counter-propagating manner. To avoid self-lasing of the amplifier, a fiber-based, polarization-insensitive isolator (Iso) was installed between the two active segments. Additionally, both fiber ends of the amplifier were polished under an angle of eight degrees to avoid reflections back into the active components. Besides, experience has shown that the output port was prone to light-induced damage of the facet, so a pigtailed ferrule with an anti-reflection coating was used. At a rather moderate total pump power of 250 mW, the extracted average power was 24.9 mW. At this point, the light was transformed into an arbitrary state of polarization due to birefringence in the fiber, which could be accounted for by a combination of a quarter-wave plate (QWP) and a half-wave plate (HWP). Additionally, the effect of NPR was clearly apparent in the polarization properties of the emerging pulses, although the peak power of the amplified signal pulses with an estimated pulse duration of 240 ps was only at a level of 91 W; the effective nonlinearity was increased, because of the relatively long single-mode fiber at the end of the pre-amplifier. NPR resulted in a decreased polarization extinction ratio (PER), which was determined to be 1:5, meaning effectively 20 % of the pulse energy were nonlinearly rotated in polarization. Consequently, the state of polarization also changed over the spectrum, because highly chirped pulses were present. In this case, the instantaneous power, as well as the instantaneous wavelength were linked, so that the peak of the pulse and hence the central part of the spectrum experienced more NPR than the wings. A polarization-sensitive free-space isolator (Iso) separated the pre- and the main-amplifier, to prevent any reflections back into the single-mode part. A wavelength- and polarization-dependent transmission was observed, which confirmed the presence of NPR. In an optimal setting of the waveplates, an average power of 17.6 mW was transmitted through the isolator, to be available as a seed for the main-amplifier.

The main amplifier consisted of an Ytterbium-doped large mode area fiber with a double cladding (DC) structure (DC-Yb^{3+}, Liekki Yb1200-25/250DC). The large core reduced the power density considerably, resulting in a reduced nonlinearity by a factor of 17, compared to a single-mode fiber. The inner core had a diameter of 25 µm and thus supported multiple modes. Coiling the fiber around a cylinder with a diameter of 8 cm effectively increased the bending loss to all but the fundamental mode, so the output was almost single-mode. The

beam parameter M^2 [52], a measure for the Gaussian beam quality, was measured to be 1.4, which is not far from the ideal value of one. The pump light was guided in the outer core, which exhibited an octagonal shape to increase the interaction of the pump light with the doped inner core. The resulting peak pump absorption was specified to be 10.8 dB/m and was experimentally determined to 7.4 dB/m. This discrepancy was a result of the slightly detuned central wavelength of the pump diode. The length of the fiber was chosen to 2.3 m to absorb 98 % of the pump light. Up to 45 W of pump power were available from a multi-mode fiber coupled diode array (JOLD-45-CPFX from Jenoptik) and coupled into the counterpropagating direction into the DC fiber. A dichroic mirror (DM) was used to merge the beam path of the pump light sent through the fiber with the amplified pulses emerging from the fiber. On the seed entrance side another dichroic mirror (DM) was used to filter out the depleted pump light, to avoid damage to any previous optical elements.

In order to minimize the build-up of ASE and to avoid self-lasing, the entrance facet was hand-polished with an angle of 8°. Because the pulse power was highest at the output side of the fiber, the facet tended to suffer from optical induced damage, as experience showed. A fused end-cap reduced the surface power density at the interface between glass and air and thus the susceptibility to damage. To prevent an overstrain of the fiber and an excessive accumulation of undesired nonlinear effects, the pump power was kept below 14 W resulting in an extracted amplified pulse power of 5 W. The peak power of these chirped pulses amounted to 18 kW, while the magnitude of induced nonlinear effects was higher by a factor of 11 compared to a pulse with a peak power of 91 W in a single-mode fiber in the pre-amplifier. For this estimation, the peak power was prorated with the different core areas for a single-mode fiber with a core radius of 3 µm and the LMA fiber with a core radius of 12.5 µm. Nontheless, the PER measured behind the main amplifier was lower by a factor of two, compared to the pre-amplifier, because the interaction length in the LMA main amplifier was considerably shorter.

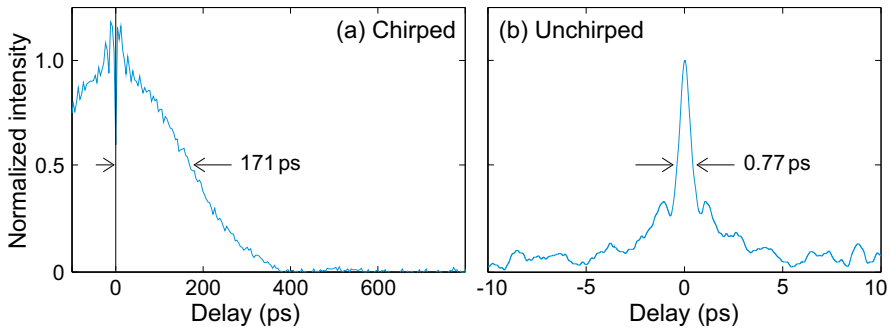

Figure 4: (a) Interferometric autocorrelation trace of the uncompressed pulse from the MOPA-system and (b) background-free intensity autocorrelation of the recompressed pulse.

Directly after the amplifier, a high power free-space isolator was used to keep any back reflections out of the fiber. A measured autocorrelation function of the emerging pulses is shown in Fig. 4 (a). Because of the long mechanical scanning ranges needed for such long pulses, the autocorrelator only measured a bit more than one half of the interferometric autocorrelation function and undersampled the interferometric signature around zero delay. Assuming a symmetric autocorrelation and a Gaussian shape, the measurement yielded a pulse duration of 240 ps. To recompress this pulse, a conventional transmission grating compressor was used. Two gratings, identical to the one used in the stretcher, were placed parallel in a distance of about 104 cm to one another. A slightly vertically tilted mirror sent the dispersed beam back through the compressor, with a slight spatial offset to the incident beam for a spatial separation. The transmission through the whole compressor was 80 %. A background-free intensity autocorrelation of the recompressed pulses is shown in Fig. 4 (b). It is far from being bandwidth-limited, as apparently higher-order dispersion and residual nonlinear phase distortions were not compensated with the grating compressor. On the one hand, the width of the central part of the autocorrelation function was larger, than expected from the bandwidth. On the other hand, there are clear indications of pre- or post-pulses, which are indistinguishable in an autocorrelation trace, at about ± 1 ps, additionally to a structured surrounding. The shape of these pulses is strongly limiting the applicability of the pulses for all nonlinear experiments.

2.1.3 Pulse Shaping

The aforementioned pulse shape deterioration due to the effects of higher-order dispersion and nonlinear effects required the implementation of a pulse shaper into the CPA system. Within this field, there has been a lot of development in the recent years. Femtosecond pulse shaping with programmable spatial light modulators in general, allows for almost arbitrary modifications in the amplitude and phase of a pulse [53]. The direct shaping of a pulse has been shown in, e.g., [54, 55, 56], but there are limitations in terms of a rather low throughput and a high susceptibility for optically induced damage of the spatial light modulator. To circumvent these issues, the shaper had to be incorporated before the amplifier chain [57, 58], because firstly, the losses were compensated for within the amplification process and secondly and most importantly, the optical power at this stage was low enough, not to induce any damage to the components. In this way, the contributions of uncompensated material and waveguide dispersion, nonlinearities and the non-uniform spectral gain of the Ytterbium fibers could be made up for. A direct approach to measure the spectral phase at the output and imprint it onto the pulse before the amplification was not applicable, because the transfer function of the amplifier was not linear. For this reason

an iterative approach with the aim to maximize the peak power of the output pulse was used for the spectral phase optimization. To serve this purpose, various algorithms have been used before, like parameterizing the search space using truncated Taylor series [59], applying genetic algorithms [60] or differential evolution [57]. Because of its simplicity, as well as efficiency, we applied the particle swarm optimization (PSO) approach [61] and adapted a corresponding code from [62] into a Matlab program.

The principle of PSO is to solve a problem by having a population of candidate solutions (in this case the spectral phase image being imprinted onto the SLM), called particles and to move these around in the search space. In order to reduce the complexity of the search space, whose dimensionality was made up from the 12288 pixels of the SLM, the phase image was comprised of 30 variable amplitudes with a linear interpolation between these points to fill all pixels. All particles were initialized with a random phase picture and organized in multiple swarms to avoid running into a local maximum. A measure of quality, also called fitness, was given experimentally by observing the intensity of the second harmonic radiation generated in a nonlinear crystal. Due to its nonlinear nature, the second harmonic generation (SHG) is sensitive to the peak power of the incident light field, which in turn depends on the pulse duration and spectral phase if the average power is kept constant.

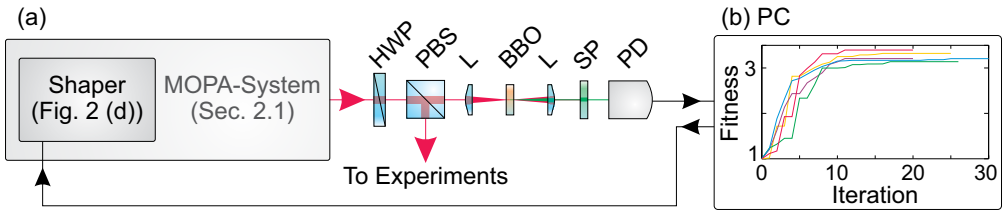

Figure 5: (a) Schematic experimental setup of the shaper. The pulse emerging from the MOPA-system was variably split with a combination of a half-wave plate (HWP) and a polarizing beamsplitter (PBS). One part was directed to the experiments and the other part focussed into a beta-Barium Borate crystal (BBO) with a lens (L) to generate the second harmonic, which was detected with a Photodiode (PD) after a short-pass filter (SP) and read out with a computer (PC). It evaluated the fitness and controled the shaper for the particle swarm optimization. (b) Evolution of the fitness for various PSO iterations.

As the scheme in Fig. 5 (a) depicts, the output of the MOPA-system was split variably with a half-wave plate (HWP) and a polarizing beam-splitter (PBS). One part was used for the actual experiments, while the other part was focused into a beta-Barium-Borate crystal (BBO) wherein SHG was generated. The fundamental light was blocked by a short-pass filter (SP) and the SHG light was detected with a photodiode (PD) which yielded the fitness of the currently shaped pulse. For every particle, in our case 25 particles in each of four swarms, the fitness was determined. Afterwards, the local and global fitness

values were compared and every particle was assigned a new solution, totalized by the sum of weighted phase pictures from their individual history, their swarm and the global optimum, combined with a random mutation. Optimally, after several iterations, all candidate solutions converged towards the global optimum. The fitness of the pulses evolved as shown in Fig. 5 (b) for several runs. After a strong increase at the first iterations, it stagnated at a three-fold increased fitness. A quantitative interpretation of this factor concerning the pulse improvement is limited, because of the complex pulse shape, but assuming a quadratic dependence of the SHG signal from the peak power a three times higher SHG signal indicates that the peak power of the shaped pulses has increased about $\sqrt{3}$-fold. To get an impression of the pulse shape, Fig. 6 (a) shows an interferometric autocorrelation trace of an unshaped pulse in blue. The resultant intensity autocorrelation function was calculated and shown as the red line. Its FWHM duration is 1.9 ps and the shape is highly structured, suggesting multiple sub-pulses as a result of the dispersion of higher order and residual nonlinearities in the amplifier. After applying the PSO routine, the autocorrelation trace (Fig. 6 (b)) is much cleaner and a dominant pulse with a autocorrelation width of 419 fs is clearly visible. This corresponds to a pulse width of 296 fs, assuming a Gaussian shape.

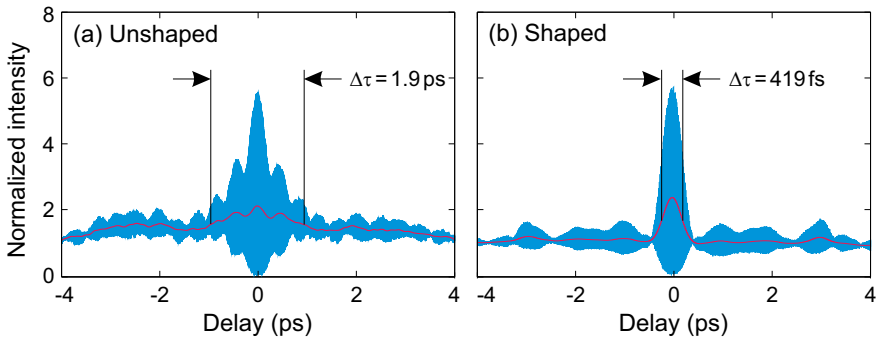

Figure 6: (a) Interferometric autocorrelation of an unoptimized pulse and (b) a pulse after the particle swarm optimization of the shaper.

Additionally to the autocorrelation measurement, a commercial FROG-device (pulseCheck with FROG option from APE GmbH) has been used to reveal more details of the pulse shapes. FROG stands for "frequency resolved optical gating" and is a technique to retrieve the full electric field, i. e., the amplitude and phase information of an ultrashort pulse [63, 64]. The measurement is in principle a spectrally resolved intensity autocorrelation, which is shown in Figs. 7 (a) and (c) in the case of an unshaped and an optimized pulse, respectively. The spectral SHG intensity is plotted versus the wavelength and the delay in false colors. The FROG trace of the unshaped pulse shows a highly distorted temporal allocation of the frequency components and the FROG reconstruction failed for this case, because the retrieved FROG trace shown in Fig. 7 (b) did not converge towards the measurement with the applied FROG algorithm provided by

APE. This failure is also reflected in the FROG error, a measure of the reliability of the reconstruction, which should be well below 5 % in trustworthy measurements under experimental conditions [65]. The FROG error of the measurement was 7.5 % and the retrieved FROG trace shows major deviations from the measurement, such that the reconstructed temporal intensity and phase shown in Fig. 7 (e) is not to be trusted, because of the failure of the algorithm.

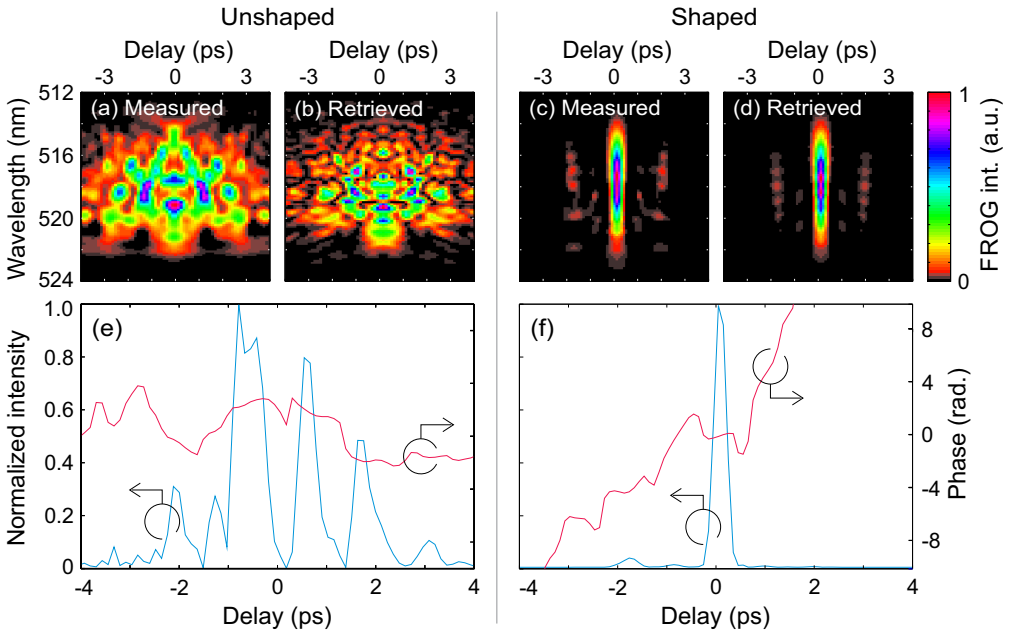

Figure 7: (a) Measured and (b) retrievd FROG trace of an unoptimized pulse. (c) Measured and (d) retrieved FROG trace of a pulse after the particle swarm optimization of the shaper. (e), (f) Retrieved temporal intensity and phase of the unshaped and shaped pulse, respectively.

In the shaped case however, the FROG trace shows a much simpler distribution, in which the main part of the pulse is temporally localized, expressed in a temporally narrow and spectrally wide oval. This results in a well reconstructed FROG trace through the iterative FROG algorithm, shown in Fig. 7 (d), with a FROG error of 0.6 %, which is one order of magnitude better than in the unshaped case. The temporal intensity distribution and the corresponding phase are shown in Fig. 7 (f). Here also rather small pre-pulses are visible around -1 ps and -2 ps, but the main pulse possesses a pulse with a duration of 296 fs, matching the estimation from the autocorrelation measurement in Fig. 6 (b). This yields a peak power of 3 MW, if the main pulse contains an energy of 1 µJ, which is suitable to drive various nonlinear processes with high efficiency.

2.2 BROAD-BANDWIDTH SUPERCONTINUUM GENERATION

The synthesis of an appropriate probe pulse with a high spectral bandwidth for the broadband coherent Raman methods, presented in Chaps. 3 and 4, was ac-

complished by the generation of a supercontinuum (SC). Supercontinuum generation (SCG) first observed by Alfano et al. in 1970 [66] describes the broadening of the spectrum of the initial pulse due to nonlinear effects. Since then, SCG was observed and investigated in various nonlinear media, ranging from gases [67], liquids [68] to bulk materials [69] and in different kinds of waveguides. Especially the advances in the fiber technology by the advent of the photonic crystal fiber [70] has led to new opportunities for the application of a SC. In general, the processes responsible for the SCG are highly nonlinear and mostly incorporate the use of ultrashort laser pulses.

The SCG in waveguides or in fibers is reviewed extensively in an article from Dudley et al. [71], wherein it is shown, that the SCG performance drastically decreases with the utilization of rather long pulses (>100 fs), as generated by the presented laser system in Sec. 2.1.2. In this regime, the spectral broadening process is dominated by modulation instabilities and four-wave mixing processes, wherein the initial dynamics are seeded from noise. As a result, the coherence properties of the SC deteriorate and pulse-to-pulse fluctuations increase dramatically. While an averaging over multiple pulses results in a smooth spectral appearance, every individual pulse exhibits a highly structured spectrum and varying temporal pulse characteristics.

However, in contrast to waveguides, bulk materials offer some favorable advantages, as therein continua with a broad and smooth spectrum, high temporal and spatial coherence, and very high stability are generated. However, in bulk media only a fraction of the pulse in the order of a few percent is converted into a supercontinuum, while in gases the full pulse experiences a spectral broadening [72], but only at a pulse energy in the order of millijoule. SCG in liquids, as another alternative, typically exhibit an exponential decrease of the spectral intensity with increasing distance to the pump wavelength [73].

SCG in bulk media is closely linked to self-focusing and filamentation. Compared to SCG in waveguides, it does therefore not depend on noise inducing processes like modulation instabilities at a higher pulse duration. The self-focusing process exhibits a threshold for the peak power of the pump pulse in the order of one megawatt, which is reached with the pulse characteristics of the applied laser system at about one microjoule of pulse energy. At this energy level, self-focusing based on the Kerr-effect induces a drastic reduction of the beam size, until multiphoton ionisation processes generate a plasma which describes an increased number of electrons promoted from the valence to the conduction band. The plasma density stays well below the critical density of 10^{21} electrons per cm^3 and typically reaches 10^{18} to 10^{20} electrons per cm^3 [74, 75]. The plasma density also has an effect on the index of refraction, just as the Kerr effect has, but with an opposite sign and a temporal retardation. Eventually, the plasma defocusing and Kerr self-focusing effects balance and a filament is formed, wherein the light is guided. The spatial confinement evokes

spectral broadening effects like self-phase modulation combined with temporal dynamic effects, as self-steepening and plasma dynamics, whose complex interplay is well described, e.g., in [75]. The filament only shows a limited length (in bulk in the order of a few millimeters), due to nonlinear absorption and dispersion.

In Sec. 2.2.1 the experimental approach for SCG is presented, together with general considerations. In the following Sec. 2.2.2 a parameter study is presented, to gain some more insight into the process of SCG in bulk media.

2.2.1 Experimental Considerations

The SCG in bulk media does in principle involve a rather simple experimental setup as shown in Fig. 8. The incident beam was variably split with a combination of a half-wave plate (HWP) and a polarizing beamsplitter (PBS) and focused with a lens (L) into the bulk medium (Bulk), wherein the filament was formed and consequently the SC was generated. When collimating the emerging SC, its large bandwidth had to be considered. Depending on the application, achromatic lenses (AL) or reflective off-axis parabolic mirrors were used. The achromatic lenses are easily adjustable, but these rather thick lenses induce a pulse lengthening by chromatic dispersion, which is undesired in certain applications. The parabolic mirrors are difficult to be adjusted properly, but show neither chromatic aberrations, nor dispersion.

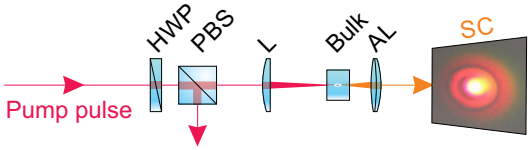

Figure 8: Experimental setup for SCG in a bulk medium. HWP: half-wave plate, PBS: polarizing beamsplitter, L: lens, Bulk: bulk medium, AL: achromatic lens. The inset shows a photograph of an emerging SC.

For an optimal SCG process, there are several experimental parameters to be considered. The most important element is the bulk medium itself, which has to exhibit a high damage threshold and a sufficient nonlinearity that is needed for the self-focusing and filamentation to occur. Laser-host materials do not share the high nonlinearity of crystals typically used for nonlinear frequency conversion, like, e. g. lithium niobate (LN) with a nonlinear index of refraction of $20{\cdot}10^{-16}\,\mathrm{cm}^2/\mathrm{W}$ [76], but exhibit a considerably higher damage threshold (compare e. g. LN with a damage threshold of $10\,\mathrm{J/cm}^2$ [77] to YAG with a damage threshold of $100\,\mathrm{J/cm}^2$ [78]). Correspondingly, laser-host materials are excellently suited for the application to SCG. Among these host materials are sapphire, yttrium aluminum garnet (YAG), potassium-gadolinium tungstate (KGW), yttrium vanadate (YVO_4) and gadolinium vanadate ($GdVO_4$),

sorted ascending by their nonlinear index of refraction, ranging from $1.2{\cdot}10^{-16}$ to $15{\cdot}10^{-16}\,\mathrm{cm}^2/\mathrm{W}$. A good introduction and overview of the SCG with these crystals is given by Bradler et al. [79], wherein the investigations focus on the spectral energy density distribution, pulse-to-pulse stability, pump energy thresholds, continuum beam profiles in dependence on the focusing conditions, crystal thickness, pump pulse energy, and pump wavelength. Bradler et al. found optimal SC properties, when the incident light was focused with a lens with a focal length of 80 mm into a crystal of at least 4 mm thickness. The optimization of the crystal position, pulse power and numerical aperture (with an iris placed before the focusing lens) yielded stable SC with a high coherence and low pulse-to-pulse fluctuations. With the present laser system in this work, the pulse parameters, i. e. the peak power and pulse duration, are just sufficient to enable SCG in bulk media, such that there is not one single optimum to be found with the aforementioned optimization procedure. Consequently, the next section presents a summary of a more detailed parameter study for an optimal SCG process.

2.2.2 Parameter Study in Various Laser Host Materials

The parameter study focused on the quality, i. e., the spectral width, energy content and power stability, of the SC generated in different laser host materials with the laser system presented in Sec. 2.1. Although sapphire is widely applied, e.g., to generate seed pulses for optical parametric amplifiers [80] or for transient absorption spectroscopy [81], it is not suitable with the present pulse parameters, namely the pulse duration, as no SCG was observable. It was found, that $GdVO_4$ is an excellent candidate, if a high performance in the infrared region is of interest. This is especially important for the realized narrow-bandwidth optical parametric amplifiers, presented in the next Sec. 2.3, were the SC was used as a seed. There was a critical pump energy-dependence on the SCG, which can be seen in Fig. 9 (a), where the spectral energy density is plotted in false color against the wavelength and the incident pump energy on a logarithmic scale. A notch filter was used in this measurement to filter out the pump wavelength, because its energy density was three orders of magnitude higher, than the actual SC, which could not be resolved by the applied spectrometer. In total, typically only a fraction in the order of a few percent was converted into the new wavelength range. Just below a pump energy of 0.6 µJ a visible bright blue filament formed in the crystal, whereas at higher pulse energies the actual spectral broadening set in and reached the spectrometers detection limit in the infrared at 1700 nm at about 1 µJ of pump energy. Note that in this measurement for this crystal there was almost no extension into the visible spectral region apparent. Above about 1 µJ of pump energy, the spectrum in the infrared region started to exhibit a periodical modulation, which is

a clear indication of multiple filaments forming inside the crystal. These arise, as soon as twice the critical self-focusing power is reached, so that two individual filaments occur and produce two independent, but coherent SC. This effect is often accompanied by the alteration of the beam profile of the SC, so that in most applications a single filament is preferred.

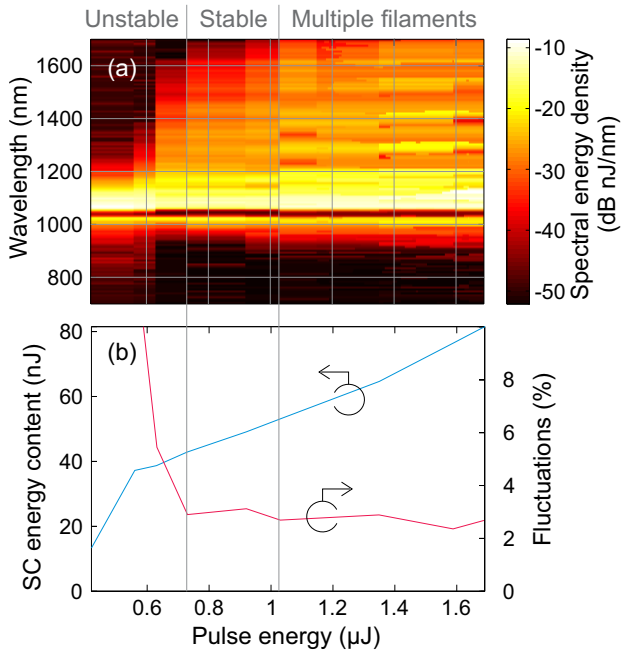

Figure 9: (a) Spectral energy density depending on the wavelength and incident pump pulse energy, plotted in false color on a logarithmic scale. (b) Absolute pulse energy contained within the supercontinuum (blue line) and the RMS pulse-to-pulse fluctuations (red-dashed line) depending on the incident pump pulse energy.

Fig. 9 (b) shows the corresponding evolution of the average power contained within the SC and the RMS pulse-to-pulse fluctuations in the infrared region above 1100 nm, depending on the incident pump energy. Although the region below a pump energy of 0.6 μJ where the spectral broadening set in already contained some portion of energy, its pulse-to-pulse fluctuations were extremely high. This is because around the threshold of the self-focusing relatively small pump pulse fluctuations (~0.5 %) induce such a large effect. Increasing the pump energy above the threshold also increased the energy content within the SC linearly, while the fluctuations stayed roughly constant at a low level. This was even the case in the region, where multiple filaments arose, indicating that multiple filaments share the stability properties of single filaments. These experiments have been performed at one optimized focal position in the crystal, but the position itself was also investigated.

The results of this investigation is shown in Fig. 10 (a), where the crystal position was varied, while keeping the pump energy constantly at 1 μJ. The resulting spectral energy density is plotted in false color against the wavelength

on a logarithmic scale. As can be seen, an efficient spectral broadening was achieved within a crystal position between 0.8 and 3.8 mm (the crystal length is 4 mm), so apparently the self-focusing effect was only sufficiently strong after the pulse traveled a distance of a few hundred micrometer inside the crystal. Below this distance, the diffraction surpassed the self-focusing. Behind a position of 3.8 mm, the crystal ended, before the filament reached its full length, so that no considerable spectral broadening was visible. In between this range, there was a clear tendency of a most efficient broadening into the infrared region at the beginning of the crystal, with a maximum extension at about 1 mm. On the contrary, the widest expanse into the visible was found further backwards in the crystal at about 2.8 mm, reaching down to 650 nm. The reason for this observation can be found when considering the effects responsible for the spectral broadening, which differ for the visible and the infrared side. The spectral components on the blue shifted side originate from self-steepening, meaning that the trailing edge of the pulse experiences a nonlinear induced steepening, so that consequently self-phase modulation induces an asymmetric spectral broadening with a stronger blue shift. These effects take place at the beginning of the filamentation, while the red-shift occurs over the propagation through the filament, due to plasma defocusing.

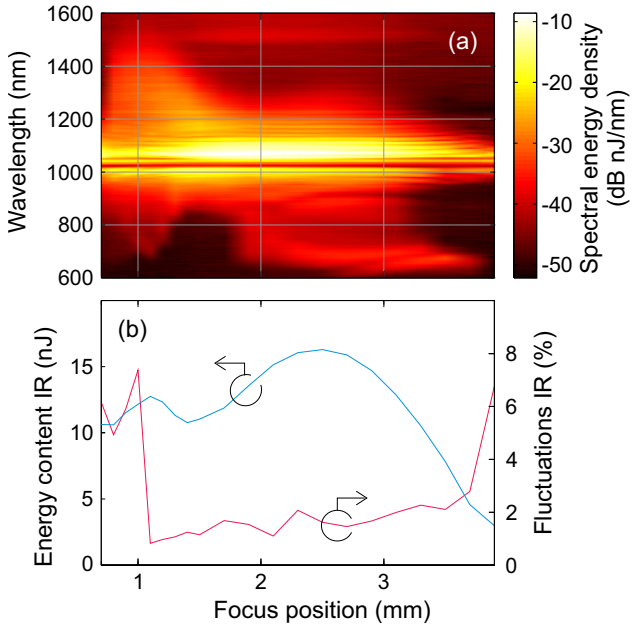

Figure 10: (a) Spectral energy density depending on the wavelength and focus position, plotted in false color on a logarithmic scale. (b) Absolute pulse energy contained within the infrared part of the supercontinuum >1000 nm (blue line) and the RMS pulse-to-pulse fluctuations (red-dashed line) depending on the focus position.

Fig. 10 (b) shows the position-dependence of the energy content in the infrared part (above 1100 nm) of the SC as a blue line and the corresponding

RMS fluctuations as a red-dashed line. The most stable point of operation in the infrared region was located just at the broadest extension of the spectrum, slightly above a focal position of 1 mm, with RMS fluctuations below 1 %. At the position of about 2.8 mm, at which the extent into the visible region was the widest, the energy content in the infrared was highest, but the spectrum only extended to about 1300 nm and showed slightly higher fluctuations.

All the other crystals had individual advantages, but also disadvantages. KGW showed the lowest threshold for the SCG, but did only cover a spectral region of 780 to 1300 nm. YVO_4 showed a performance very comparable to $GdVO_4$, but the spectrum only extended to 1350 nm, while containing the same amount of energy, which might be preferable when an absolute higher spectral power density is of interest. YAG certainly had the highest threshold and a rather poor performance in the infrared region, but was superior in the visible region, concerning energy content and spectral extent, reaching down to 615 nm. For this reason, YAG was chosen as the bulk material to generate the SC for all coherent Raman scattering experiments in Chaps. 3 and 4, while $GdVO_4$ was chosen as a seed source for the optical parametric amplifiers in the next Sec. 2.3 due to its superior performance in the infrared region.

2.3 NARROW-BANDWIDTH OPTICAL PARAMETRIC AMPLIFIERS

One important development of the presented light source aims towards narrow-bandwidth, tunable pulses for the application in nonlinear spectroscopic coherent Raman scattering schemes as discussed in Chap. 3. These schemes all use two synchronized pulses to coherently drive one narrow Raman resonance, corresponding to the frequency difference between the applied pulses. The high repetition frequency combined with the high pulse energy of the presented laser system makes a perfect foundation for nonlinear frequency conversion in a nonlinear crystal to generate tailored pulses with optical parametric amplification [82]. The following sections summarize previous work on optical parametric generation and amplification with different nonlinear crystals.

2.3.1 Periodically Poled Lithium Niobate

In order to generate a synchronized pulse in the spectral region around 1500 nm, a periodically poled lithium niobate (PPLN [83]) crystal was used. Compared to critically phase-matched crystals, periodically poled quasi-phase-matched crystals allow for a high gain due to high effective nonlinear coefficient and no spatial walk-off. Within the framework of a Bachelor thesis of Christian Egelkamp [37], a PPLN crystal with a fan-out structure [84] enabled optical parametric generation of a tunable signal pulse ranging from 1480 to 1620 nm. In combination with the broad-bandwidth supercontinuum emerging from a

bulk gadolinium vanadate ($GdVO_4$) crystal as a seed pulse, optical parametric amplification was achieved with an efficiency of up to 13 %, yielding stable pulses with a pulse power of up to 15 nJ. At a poling period of 29.7 µm the spectrum of the optical parametric generated light with an incident pump power of 87 nJ is depicted in Fig. 11 (a) in green on a logarithmic scale. A peak at a central wavelength of 1480 nm was apparent, which contained 220 pJ of energy. The seed supercontinuum (SC) is depicted in blue and shows a typical trend as discussed in Sec. 2.2. Together with a pump pulse with an energy of 87 nJ, optical parametric amplification shown in red is clearly visible, as the wavelength components around 1480 nm from the supercontinuum are amplified by 28 dB. The width of this peak amounts to 16 nm (~ 73 cm^{-1}), with a slight asymmetry on the lower wavelength side. The variation of the poling period and by that the variation of the central frequency of the OPG/OPA signal was simply realized by laterally shifting the fan-out PPLN crystal. Fig. 11 (b) shows the spectral energy density of the optically parametric amplified signal pulses plotted versus the wavelength and the poling period of the PPLN in false colors. Additionally, a calculated tuning curve is shown as a blue line, which matches the experimental data well. It was calculated with the software SNLO [85].

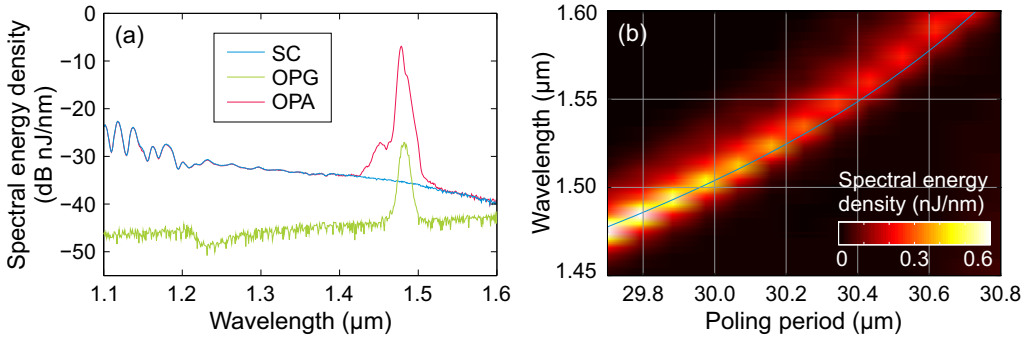

Figure 11: (a) Spectral energy density plotted versus the wavelength of optical parametric generation (OPG, green line) and optical parametric amplification (OPA, red line) of a seed supercontinuum (SC, blue line) in PPLN. (b) Spectral energy density depending on the wavelength and the poling period of the PPLN on a linear false color scale and respective calculated tuning curve [85] in blue.

The main limitation within these experiments was the limited applicable pump pulse energy. Raising it above 100 nJ resulted in highly distorted signal pulse spectra, which is most likely attributable to nonlinear interactions between the pump and signal pulse along the crystal length. Additionally, the spectral bandwidth of the signal radiation exceeded the expectations by a factor of five, which is most likely due to the temporal walk-off between the pump and the signal pulse inside the PPLN due to its dispersion. The achieved conversion efficiency of 13 % lies below reported values of 30 % [84], because of the same reason. The spectral bandwidth of the emerging pulses also limits the applica-

bility to spectroscopy, because the bandwidth of the pulses dictates the spectral resolution of the narrow-bandwidth coherent Raman scattering schemes. In order to increase the interaction length inside the crystal, picosecond pump pulses will have to be implemented in the future.

Apart from this, the signal pulse covered in combination with the MOPA pulse the range of 2900 to 3500 cm^{-1} in their difference frequency, which is just enough to reach the interesting C-H stretch region around 3000 cm^{-1} in a spectroscopic application (see Chap. 3). A new PPLN crystal with an adapted poling periodicity will shift the generated signal pulses even more into the appropriate region of interest. Additionally, the simultaneously generated idler pulses will be investigated for future applications [86, 87], because its central wavelength is located in the mid-infrared spectral region. In the current configuration, the idler pulse theoretically has a tunable central wavelength of 2860 to 3450 nm. Shifting the frequency difference between the fundamental pump pulse and the signal pulse into the C-H stretch region, will consequently increase the central wavelength of the idler pulse even further. A fundamental limitation provides the transparency of the PPLN, which decreases considerably starting at 4000 nm. This also affects the efficiency of the parametric process, because all three waves (pump, signal and idler) contribute to the conversion. Especially reaching down to the so called fingerprint region around 1200 cm^{-1}, with a corresponding idler wavelength around 8333 nm is not feasible inside a PPLN. Hence, the next two sections present results obtained in crystals with a broad transmission beyond 12000 nm.

2.3.2 Silver Thiogallate

The wide transmission window of Silver Thiogallate ($AgGaS_2$ or AGS) together with its nonlinear and birefringent properties [88, 89] are well suited for parametric conversion [90]. It is mostly used in difference frequency generation [91], but also in optical parametric oscillators [92]. In regard of his Diploma thesis, Gerrit Hölscher showed successful critically phase matched optical parametric amplification in AGS of narrow spectral parts of a SC generated in bulk $GdVO_4$ [35]. Fig. 12 (a) shows the spectral energy density of the seed supercontinuum (SC) in blue, plotted against the wavelength. Keeping the incident pump power below the damage threshold of AGS at about 200 nJ, yielded the optical parametric amplification as shown in red. At an incidence perpendicular to the surface of the AGS crystal, which was cut at $\varphi = 48.5°$, the SC was amplified at a wavelength of 1374 nm within a width of 13 nm ($\sim 68\ cm^{-1}$). A rotation of the crystal, such that the internal angle was varied from 41 to 54°, resulted in a tuning of the central wavelength of the emerging signal pulse from 1240 to 1670 nm, as shown in Fig. 12 (b). The crystal mount prevented a continuous tuning of the full angle-range, wherefore the measurement had to be performed in

two series, represented in open circles and dots. The theoretical tuning curve shown as a blue line was calculated with the software SNLO [85] and describes the measurement well.

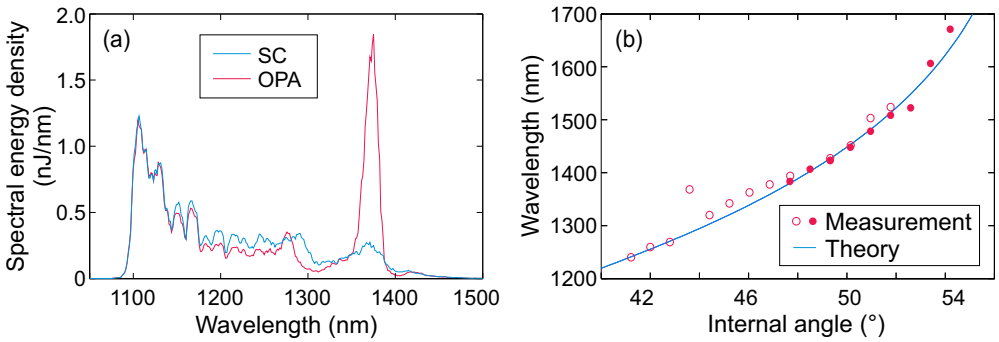

Figure 12: (a) Spectral energy density plotted versus the wavelength of optical parametric generation (OPG, green line) and optical parametric amplification (OPA, red line) of a seed supercontinuum (SC, blue line) in AGS. (b) Measured central wavelength of the amplified signal (red dots and circles), depending on the internal crystal angle and respective calculated tuning curve [85] in blue.

With a pump wavelength of 1064 nm, a conversion efficiency of 0.2 % has been shown for optical parametric generation of a signal pulse with wavelength around 1265 nm [93]. The reason, no parametric generated light was detectable with the presented work, was again accountable for the application of femtosecond pump pulses and the resulting limited effective interaction length inside the crystal due to the temporal walk-off. Although the AGS crystal allowed for an impressive tuning range, covering 1600 to 3670 cm^{-1} in the signal wavelength, the main limitation was the high susceptibility towards optically induced damage and thus restricts a further scaling of the output power. The crystal presented in the next section shares many characteristics of AGS, but promises a higher damage threshold.

2.3.3 Lithium Indium Selenide

With comparable beneficial features of AGS, lithium indium selenide ($LiInSe_2$ or LISE) was used as a nonlinear crystal for optical parametric amplification. The LISE crystal has only been developed in 2005 for the application in nonlinear frequency conversion [94, 95]. LISE has been successfully applied in an optical parametric oscillator [96] and for parametric downconversion of a pump pulse with a duration of 220 fs and a central wavelength of 820 nm [97]. As this crystal became commercially available in an good optical quality, it was also implemented in the present work. Two differently cut LISE crystals were used, the first cut at an angle of $\Theta = 90°$ and $\varphi = 45°$, while the second one was cut at $\Theta = 90°$ and $\varphi = 79°$, both with a thickness of 3 mm. A result of OPA in the

second crystal is depicted in Fig. 13 (a), where the spectral energy density of the seed-SC (blue line) and the OPA spectrum (red line) is plotted versus the wavelength on a linear scale. The amplification amounted to a factor of 40 and was located at a central wavelength of 1512 nm with a width of 17.6 nm (~77 cm^{-1}). The tuning range of both crystals is depicted in Fig. 13 (b), wherein a tuning across 1146 to 1379 nm (open red circles) and 1414 to 1512 nm (red dots) was achieved for the first and second crystal, respectively. The theoretical tuning curve was calculated with the software SNLO [85] and is shown in Fig. 13 (b) as a blue curve.

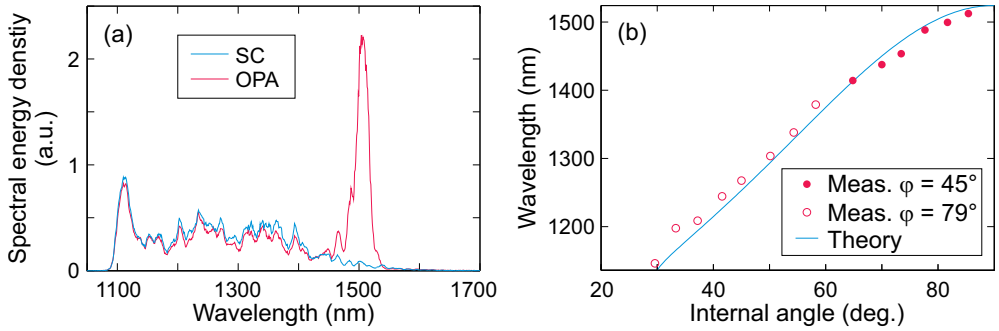

Figure 13: (a) Spectral energy density plotted versus the wavelength of optical parametric amplification (OPA, red line) of a seed supercontinuum (SC, blue line) in LISE. (b) Measured central wavelength of the amplified signal in crystal one (red circles) and crystal two (red dots), depending on the internal crystal angle and respective calculated tuning curve [85] in blue.

The performance of the first crystal is of special interest, because the generated signal pulses, combined with a MOPA pulse, cover a range in their frequency difference of about 935 to 2410 cm^{-1}, which is suitable for spectroscopic applications, as it matches the so called fingerprint region (see Chap. 3). At the same time, the idler pulses are located in the mid-infrared region between 4150 and 10700 nm, which is of high interest for applications like for example SCG in chalcogenide fibers.

Still, there are two restrains with the current setup. Firstly, the spectral bandwidth of the signal pulses are too high for spectroscopic applications, because of the aforementioned temporal walk-off between the pump and signal pulses, limiting the effective crystal length. Secondly, the conversion efficiency is rather poor and limited by the onset of filamentation inside the crystal at a pump energy of a few hundred nanojoule. Although in this work, only the generated signal energy was determined to be in the order of tens of nanojoule, an idler energy in the order of nanojoule can be assumed, taking the reduced energy content of a mid-IR idler photon compared to a near-IR signal photon into account. The generation of idler pulses with a central wavelength of 7 µm in a LISE-based OPA have been reported [97], using comparable pulse properties and surface power densities. The efficiency was lower by two orders of mag-

nitude, compared to the work presented here. Nontheless, both, the efficiency and the spectral bandwidth will benefit from the implementation of picosecond pump pulses, as these increase the effective interaction length in the crystal and also increase the threshold of filamentation. Lastly, a new crystal cut at an angle of $\Theta = 90°$ and $\varphi = 40°$ is under investigation, to cover a lower central wavelength of the signal pulses and consequently a higher central wavelength of the idler wavelength up to the transparency limit of LISE at 12000 nm.

2.4 FURTHER DEVELOPMENT AND APPLICATIONS

The properties of the presented light source are very specific and adapted to the requirements of CRS and cannot simply be bought off-the-shelf. Although several custom designed light sources have been developed in the past for CRS experiments, the individual systems do not meet all requirements simultaneously. Exemplary and representative systems for narrow-bandwidth CRS experiments have been presented in [16], where an optical parametric oscillator was synchronously pumped with pulses from a Nd:vanadate oscillator with a repetition frequency of 76 MHz, or in [98], where an Erbium-doped fiber oscillator with a repetition frequency of 40 MHz was generating tunable pulses in PPLN crystals via spectral focusing. Both approaches rely on a high repetition frequency and are thus limited in their applicable average power. In [99] four wave mixing is exploited in a photonic crystal fiber to generate picosecond pulses with a repetition frequency in the range of MHz, but the phasematching conditions limit the tunability to the C-H stretch region. For the broad-bandwidth CRS methods, systems were introduced which either based on regenerative amplifiers [23] or on oscillators [100] with a repetition frequency of 1 kHZ and 75 MHz, respectively, both being not optimally adapted to balance the light induced damage, as discussed earlier. The light source presented in this work meets all critical criteria, namely the optimal repetition frequency of 1 MHz, the availability of synchronized, stable pulses, which are either narrow-band and tunable in their central wavelength or of broad bandwidth. Nontheless, there are several opportunities for improvements and applications, which are addressed in this section.

The ANDi-fiber laser sustains a stable mode-locked operation over weeks and a readjustments of the waveplates only became necessary if the ambient conditions changed. The day-to-day use of the output of the amplifier system involved an execution of the shaper-algorithm, because the characteristics of the amplified pulses were prone to changes in the temperature in the laboratory. Especially the state of polarization after the pre-amplifier and by that the seed pulse for the main-amplifier drifted notably. Considering that additionally the over-all performance of the pre-amplifier is relatively inefficient, a redesign

with polarization maintaining fibers and components is in order and part of future improvements.

Apart from these enhancements, the presented MOPA-system has a high potential to be employed in various applications with a high demand of pulse power and stable pulse trains at a moderate repetition frequency. In one application, Walbaum et al. [101] and Hellwig et al. [102, 103] exploited the high peak power for an experimental realization of transverse mode conversion in an optical few-mode fiber via an optical induced long period grating.

The application of the pulses generated in the different OPA systems presented in Sec. 2.3 for narrow-bandwidth spectroscopic coherent Raman scattering schemes will be implemented in future experiments. The rest of this thesis will focus on the application of the MOPA pulse in combination with a SC generated in a YAG crystal in various broad-bandwidth coherent Raman scattering schemes. A representative spectrum of the SC is depicted in Fig. 14 as a blue line, plotted against the wavelength. The sharp edge at about 950 nm corresponds to the cut-off wavelength of the short-pass filter, which also limits the extent into the visible region to approximately 600 nm. This spectrally filtered SC pulse contained an energy of about 2 nJ.

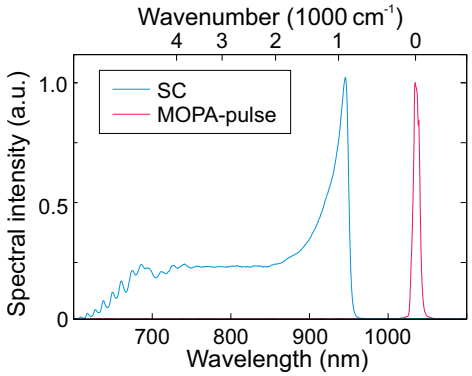

Figure 14: Spectra of a SC generated in a YAG crystal (blue line) and of the MOPA pulse (red line) plotted versus the wavelength and the wavenumber relative to the MOPA pulse. The steep edge of the SC spectrum at 950 nm is a result of the applied low-pass filter. These pulses are applied in the following broad-bandwidth coherent Raman scattering experiments.

The MOPA pulse spectrum is also shown in Fig. 14 as a red line and is centered at 1035 nm. The applicable pulse energy of the MOPA pulse is up to 2 µJ, whereof only a fraction is used in the actual experiments, in order to avoid damage to any sample. The relative frequency difference between this MOPA pulse and the SC is inserted above in wavenumbers, centered at 1035 nm. The focus in this work is concentrated on the C-H stretch region around 3000 cm^{-1}, corresponding to a SC wavelength of about 800 nm.

3 RAMAN SCATTERING SPECTROSCOPY

CONTENTS

3.1 Spontaneous Raman Scattering 34
3.2 Femtosecond Raman-Induced Kerr-Effect Spectroscopy 35
3.3 Femtosecond Stimulated Raman Scattering 37
3.4 Discussion about the Applicability to Microscopy 39

The spectroscopic schemes presented in this work all rely on an inelastic scattering of incident photons at vibrational states within molecules, called Raman scattering. It was firstly observed in the year 1928 by C. V. Raman [7], who received the Nobel price in 1930 for this discovery. The Raman effect describes the optical excitation of molecular vibrations, which exhibit specific resonances depending on the composition of the observed molecule. By probing these resonances with an optical light field, new frequency components are generated, or existing spectral components of the incident light are altered, such that a corresponding detection allows for a chemically specific analysis of the sample.

The wavelength region, in which typically Raman resonance frequencies are located, are depicted in Fig. 15 (a), which can be roughly divided into two main regions, namely the so-called "fingerprint" region as well as the "C-H stretch" region. The fingerprint region is located in the wavenumber range from 600 to 1600 cm^{-1} and contains, among others, a huge variety of stretch vibrations of carbon-based chemical bonds. Also many different bending motions of molecules possess resonances in this wavenumber region: in this region, the Raman spectra are often highly complex, especially when the molecules are comprised of many different chemical bonds. As a result, this so called fingerprint region is excellently suited for the characterization of molecules. Exemplary representatives with distinctive Raman resonances in the fingerprint region are proteins or nucleic acids [9]. The C-H stretch region is especially important in the life sciences, since the chemical bond of carbon and hydrogen is very common in many investigated samples and its Raman resonance is generally located around 3000 cm^{-1}, giving this region the name "C-H stretch" region. For example, Raman resonances of lipids are typically present in this region [104, 105], because of their abundance of chemical bonds of carbon and hydrogen. Adjacent to the C-H stretch region, at about 3300 cm^{-1}, is the rather broad resonance of water located [106], which is with only a few exceptions omni-present in biological samples.

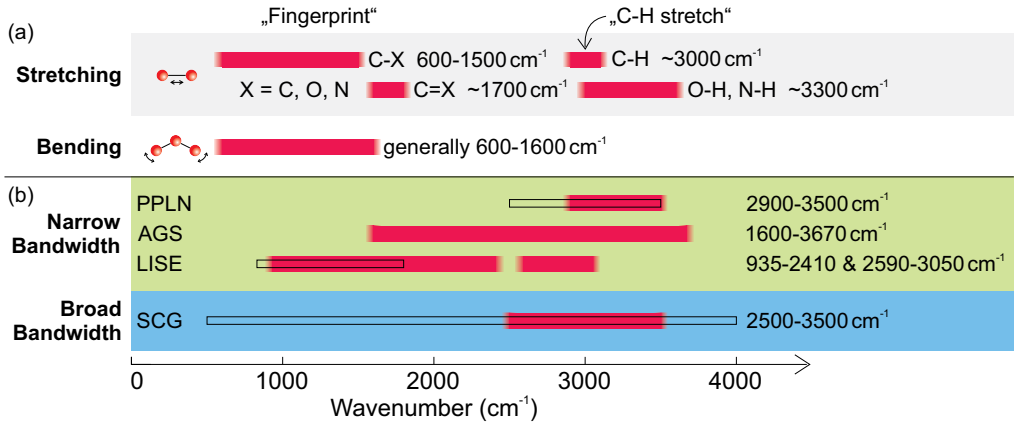

Figure 15: (a) Schematic representation of the interesting spectroscopic regions of stretching and bending motions of molecules, represented as red rectangles for common chemical bonds. (b) Spectral coverage of the presented MOPA system in combination with the narrow-bandwidth OPAs and the broad-bandwidth SC, represented as red rectangles. The open rectangles represent future developments of the light source to cover an even wider range. For details, see text.

The optical excitation of the Raman resonances was originally accomplished with narrow-bandwidth, continuous-wave light in an incoherent matter, called spontaneous Raman scattering [8]. The advent of the laser allowed for the development of schemes using a coherent or stimulated excitation of the Raman resonances. The design of the light source presented in Chap. 2 aimed to a great extent for the application of these coherent Raman scattering (CRS) spectroscopic schemes. There are a lot of different experimental implementations of CRS, which are always based on coherently driving the molecular vibrational resonances via a multi-photon process. In comparison to spontaneous Raman scattering, CRS does not only yield higher signal levels, but the signal generation is intrinsically confined to the focal volume of the excitation beams, since it is a nonlinear process. Thereby, confocal laser scanning techniques can be applied, which allow for high-speed, three-dimensional imaging, while basically the spectroscopic information is fully retained.

The existing CRS schemes can be categorized into two main groups concerning their excitation bandwidth: narrow-bandwidth and broad-bandwidth approaches. The idea behind the first one is the excitation of one narrow spectral feature or region with two narrow-bandwidth pulses, preferably bandwidth limited picosecond pulses. This allows to probe one specific narrow spectral region and to capture the Raman response at a high speed with a fast photodetector, because the acquisition time is not limited by a slow spectrometer as in broad-bandwidth schemes. The most prominent narrow-bandwidth CRS schemes are stimulated Raman scattering (SRS [107, 17]) and coherent anti-Stokes Raman scattering (CARS [108, 109, 110]), which have been successfully

applied to microscopy, by probing individual Raman resonances within a microscopic sample. Alternatively, the Raman-induced Kerr-effect (RIKE [21]) can be exploited to probe a pump pulse induced anisotropy through the Kerr-effect, which is resonantly enhanced in the vicinity of a Raman resonance. All these narrow-bandwidth approaches are viable with pulses generated with the different OPA systems presented in Sec. 2.3. As shown in Fig. 15 (b) schematically, the combination of the MOPA pulse with one of the OPA pulses already covers most of the relevant spectral regions, represented as red rectangles. The PPLN-based OPA generated tunable pulses in the vicinity of the C-H stretch region, which will be fully covered with the newly designed PPLN crystal (depicted with the open rectangle), as discussed in Sec. 2.3.1. Although the AGS-based OPA also operated in this region, it showed a rather poor performance concerning the efficiency and the susceptibility towards optically induced damage, as it was already discussed in Sec. 2.3.2. The fingerprint region is mostly covered with the LISE-based OPA system (Sec. 2.3.3), where also a newly designed crystal will extent further into the wavenumber region below 1000 cm^{-1}, as indicated by the open rectangle.

Recent broad-bandwidth CRS approaches gain access to more spectroscopic information by probing not only one but several vibrational frequencies, which has resulted in the demonstration of e.g., hyperspectral CARS imaging [111]. Employing a broadband excitation pulse, like a SC, the spectral amplitude across a resonance is acquired simultaneously in femtosecond SRS (FSRS [20]), ultrafast Raman loss spectroscopy (URLS [112]), or broadband RIKES [21], later called femtosecond RIKES (FRIKES [22]). The application of a femtosecond probe pulse in these schemes also enhances the signal generation, because in this case the peak power is considerably higher, compared to the picosecond probe pulse used in narrow-bandwidth CRS schemes. Alternatively, a rather complex phase-and-polarization control of a femtosecond pulse allows for the background-free acquisition of broad CARS spectra [113].

From here on, the thesis focuses on different broad-bandwidth approaches, except for spontaneous Raman scattering spectroscopy, which only serves as an independent reference approach (Sec. 3.1). The other presented schemes employ the combination of a MOPA pulse (Sec. 2.1) as the pump pulse and a spectrally filtered portion of a supercontinuum pulse (Sec. 2.2) as the probe pulse, which allows the extraction of a Raman spectrum over a broad wavenumber range. Two prominent and well-known representative broad-bandwidth CRS schemes are FRIKES, which is presented in Sec. 3.2 and FSRS, which is introduced in Sec. 3.3. The latter builds the foundation for the developed novel interferometric CRS approaches and will be examined in even more detail in the corresponding Chap. 4. The discussion about the applicability of the presented schemes in Sec. 3.4 concludes this chapter.

3.1 SPONTANEOUS RAMAN SCATTERING

The easiest way to measure a full Raman spectrum is the recording of the spontaneous Raman scattering [8] emission, whereat however all advantages of the nonlinear coherent methods are lost, like the intrinsic three-dimensional imaging capability and especially the higher signal levels [19]. In the context of this work, spontaneous Raman scattering is used as an independent reference measurement, to compare the spectra acquired with the coherent Raman scattering techniques to this independent reference.

A schematic respresentation of spontaneous Raman scattering is depicted in Fig. 16 (a) in form of an energy diagram. It shows the inelastic scattering of pump photons (red arrow) from the ground state via a virtual state, whereat the vibrational states in the sample are populated and photons with less energy are emitted. They are Stokes-shifted and appear on the low-energy side of the spectrum, relative to the pump light. As shown in Fig. 16 (b), pump photons (red arrows) can also be scattered from the vibrational states via virtual states, generating so-called anti-Stokes photons (green arrows). These anti-Stokes photons appear on the high-energy side of the spectrum. Assuming a classical Boltzmann energy distribution, the vibrational states are less populated than the ground state, resulting in a reduced probability of anti-Stokes scattering and thus a reduced spectral intensity, compared to the Stokes case.

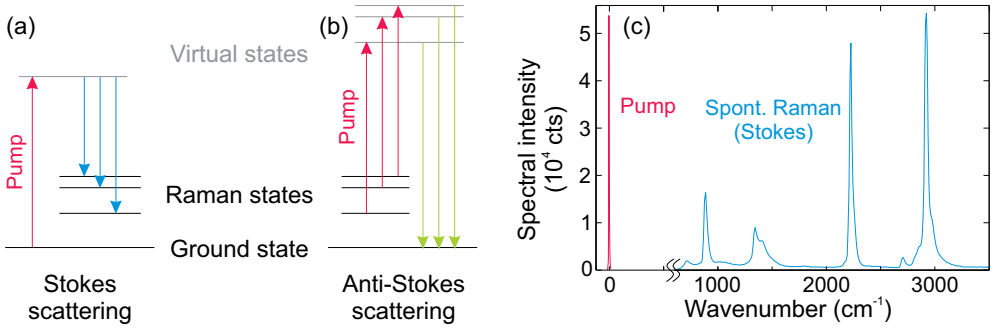

Figure 16: Schematic energy diagram of spontaneous Raman scattering for (a) the Stokes and (b) the anti-Stokes case. (c) Measured spontaneous Raman scattering spectrum of acetonitrile.

For this reason, we focus on the Stokes side of the spectrum for the presented spontaneous Raman scattering reference measurements. The spectrum of acetonitrile on a cover slip shown in Fig. 16 (c) was recorded with 2 s integration time, ten times averaging and with 0.51 W continuous-wave radiation of 532 nm wavelength incident on the sample. Several Raman transitions are clearly visible, with one being dominant at 2922 cm^{-1}. The width of this resonance is measured to be 34 cm^{-1}, which is close to the limit of the spectral resolution of the applied spectrometer (16 cm^{-1}). This rather poor resolution, together with an assumed measurement uncertainty of 1 CCD-array pixel (approx. 4 cm^{-1}), is cer-

tainly not suited to measure the position or width of the resonance with a high precision, but is sufficient for the referencing purpose. All other spontaneous Raman scattering spectra within this thesis were acquired under comparable conditions.

3.2 FEMTOSECOND RAMAN-INDUCED KERR-EFFECT SPECTROSCOPY

The Raman-induced Kerr-effect (RIKE [21, 114]) exploits the anisotropic, complex change of the refractive index of a sample induced by a strong narrow-bandwidth pump pulse by means of the optical Kerr-effect. It is resonantly enhanced in the vicinity of a Raman resonance at frequency Ω, such that a linearly polarized probe pulse matching the Raman resonance condition $\omega_{pr} - \omega_{pu} = \Omega$ experiences a change in its polarization. The induced alteration in polarization is conveniently measured with a crossed polarizer, which is set to solely transmit the polarization component perpendicular to the orientation of the initial probe pulse polarization. Employing a broad-bandwidth probe pulse results in a RIKE signal for all frequency components of the probe pulse, which fulfill the Raman resonance condition, such that consequently the measured spectrum resembles a spontaneous Raman spectrum. This scheme has been introduced in the early work of Heiman et al. [21] and has later been termed femtosecond Raman-induced Kerr-effect spectroscopy (FRIKES [22]).

As already mentioned, both, the pump and probe pulse for excitation of the RIKE process, were derived from the light source presented in Chap. 2. The MOPA pulse was spectrally filtered to a bandwidth of about 4 nm (30 cm^{-1}) to serve as the pump wave with up to 100 nJ pulse energy. The SC was generated in a YAG crystal and a combination of a long-pass and a short-pass filter was used to select a spectral band of 750 to 820 nm, containing up to 1.4 nJ pulse energy as the probe pulse. The combination of this broad-bandwidth probe pulse and the narrow-bandwidth pump pulse at 1035 nm covered a range of vibrational frequencies from 2500 to 3500 cm^{-1}.

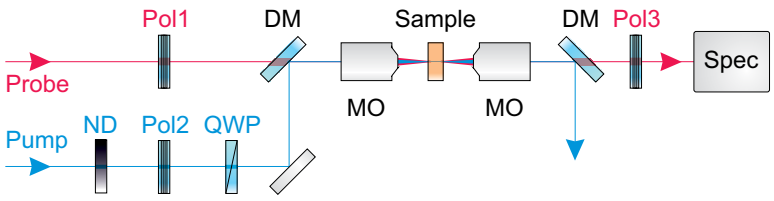

Figure 17: Schematic experimental setup of FRIKES. ND: neutral density filter, Pol#: polarizer, QWP: quarter-wave plate, DM: dichroic mirror, MO: microscope objective, Spec: spectrometer.

The schematic experimental FRIKES setup is shown in Fig. 17. The polarizer (Pol1) was used to ensure a linear state of polarization of the probe pulse, while the pump pulse polarization was adjusted to a circular state via a quarter-wave

plate (QWP) after polarizer Pol2. The circular polarization of the pump pulse was essential to suppress a nonresonant contribution within the FRIKES scheme [21]. In order not to damage the sample, a variable neutral density filter (ND) was used to adjust the power of the pump pulse, which was merged with a dichroic mirror (DM) into the beam path of the probe pulse. Both beams were focused with a microscope objective (MO) into the sample, which consisted for this demonstration purpose of acetonitrile on a cover slip. After a collimation behind the sample with a second MO, the residual pump pulse was separated from the probe pulse with another DM. Polarizer Pol3 was set perpendicular to Pol1 in order to transmit only the fraction of the probe pulse that was rotated due to RIKE. The spectrum of the probe pulse behind Pol3 was recorded with a spectrometer based on a silicon CCD-array with a spectral resolution of 0.8 nm at 800 nm (Stellarnet EPP2000). The maximum signal level was 65536 cts (16 bit ADC), while the zero level was 3000 cts. The noise of all measurements is dominated by the detector noise, which was calculated as the standard deviation of the zero level to 65 cts. Note that all presented measurements could have been easily improved by signal averaging. However, as all spectra should be comparable to each other we refrained from such post-processing. The signal strength in the FRIKES measurement was rather low (0.4 pJ), so accordingly, the spectrometer integration time had to be set to 250 ms.

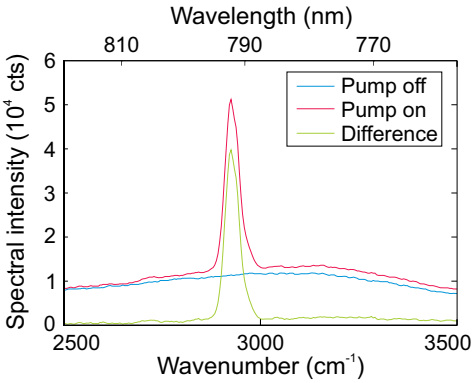

Figure 18: FRIKES measurement of acetonitrile: reference spectrum (pump off, blue-dashed curve) and the FRIKES spectrum (pump on, red curve) showing a strong peak on top of a broad background signal. The difference (green curve) corresponds to a Raman intensity spectrum.

The recorded spectra are shown in Fig. 18. A reference probe pulse measurement, i. e. with the pump pulse blocked (pump off, blue-dashed curve), shows the residual background, which results from the limited polarization extinction ratio (approx. 10000:1) of the applied polarizers. The measurement with the pump turned on (red curve) shows the dominant Raman scattering peak of acetonitrile at 792.4 nm, corresponding to a wavenumber of 2921 cm^{-1} relative to the pump pulse. The peak is situated on top of the residual background with a signal-to-background ratio (S/B-ratio) of 3:1. By subtracting the reference spec-

trum a very clean Raman scattering intensity spectrum is obtained, which can be seen as the green curve in Fig. 18. The width of the Raman peak is determined to be 37 cm^{-1}, which is insignificantly wider than the spontaneous Raman scattering trace. The small discrepancy of the position and the width of the peak in the spontaneous measurement (Fig. 16 (c)) is due to the observational error of the poorly resolving spectrometer. Apart from this, a slight increase in width can be expected due to the fact that the pump pulse exhibits a width of 30 cm^{-1}, which artificially broadens the width in the CRS spectra. The signal level of the peak is 40000 cts, resulting in a signal-to-noise ratio (S/N-ratio) of 615:1, which is close to the S/N-limit of the detector of 1000:1.

3.3 FEMTOSECOND STIMULATED RAMAN SCATTERING

Femtosecond stimulated Raman scattering (FSRS [20]) is a technique related to stimulated Raman scattering (SRS [107]), wherein a vibrational resonance with frequency Ω is driven by two light waves with frequencies ω_{pu} (pump pulse) and ω_{pr} (probe pulse), such that their difference frequency matches the vibrational resonance, $\omega_{pr} - \omega_{pu} = \Omega$. From here on, the notation of pump and probe pulse follows Ref. [20] and [23], which termed the strong, narrow-bandwidth light field pump pulse and the weak, broad-bandwidth light field probe pulse. When the resonance condition is fulfilled, energy is transferred from one light wave (ω_{pr}) to the other (ω_{pu}), leading to a measurable loss at ω_{pr}, if the probe pulse is located on the high-energy side, relative to the pump pulse. Correspondingly, the probe pulse experiences a gain, if it is located on the low-energy side of the spectrum [17]. In 2003 McCamant et al. demonstrated that when using femtosecond, broad-bandwidth pulses as one of the driving light waves a number of vibrational resonances that are located within the spectral pulse width can be covered simultaneously, while the spectral resolution is determined by the spectral bandwidth of the second pulse [20]. This scheme is termed femtosecond stimulated Raman scattering (FSRS) and its corresponding level scheme is depicted in Fig. 19 (a). All vibrational resonances Ω that fulfill the condition $\omega_{pr} - \omega_{pu} = \Omega$, whereat ω_{pr} lies within the spectral bandwidth of the probe wave, lead to a loss that can be measured as a dip in the probe spectrum (see the schematic sketch of the spectra in Fig. 19 (b)). With this FSRS technique, a Raman loss or gain spectrum can be extracted easily from a difference measurement in a single shot [23]. A mathematical treatment of FSRS will be presented in Chap. 4.

The experimental FSRS setup applied for this thesis is shown in Fig. 20 and was basically the same setup as in the FRIKES experiment in Sec. 3.2, except for the polarizaion optics. For the FSRS measurement the pump and probe pulse polarizations were set linearly and parallel to one another, ensured by polarizer Pol2 and Pol1, respectively. They were adjusted along the x-axis, which is

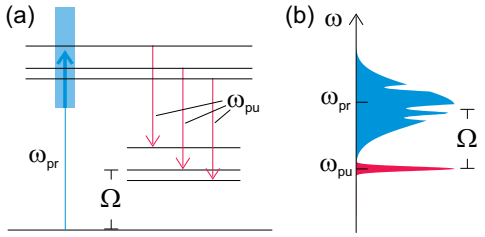

Figure 19: (a) FSRS energy level scheme and (b) corresponding spectrum displaying a Raman loss spectrum of the probe wave on the anti-Stokes side.

defined as the horizontal direction. The power of the pump pulse was attenuated with a neutral density filter (ND), in order not to damage the sample. A dichroic mirror (DM) was used to merge the MOPA pulse and the SC, which were both focused with a microscope objective (MO) into the sample, which again consisted of acetonitrile on a cover slip. The emerging light is collimated, using another MO and a second DM is used to filter out the residual pump light. The spectrum was recorded with the identical spectrometer as in the FRIKES measurements.

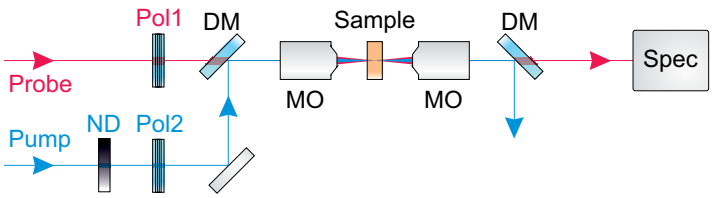

Figure 20: Schematic experimental setup of FSRS. ND: neutral density filter, Pol#: polarizer, DM: dichroic mirror, MO: microscope objective, Spec: spectrometer.

The measured probe pulse reference spectrum, is shown in Fig. 21 as the blue-dashed curve (pump off). If the pump pulse is turned on (red curve, pump on), a dip becomes visible at a wavelength of 792.4 nm, corresponding to the dominant spectral feature of acetonitrile at a Raman shift of 2921 cm^{-1}. The signal level (depth of the dip) is 2500 cts, while the background amounts to 40000 cts, resulting in a S/B-ratio of 1:15. The difference between the blue-dashed reference and the red curve is plotted in green and multiplied by a factor of five for illustration purposes and corresponds to the Raman scattering intensity spectrum.

The probe pulse energy incident to the spectrometer amounted to 0.7 nJ and had to be reduced with a 45 dB neutral density filter, in order not to saturate the spectrometer (set to a minimum integration time of 20 ms). The low signal level resulted in a S/N-ratio of 40:1, which was just sufficient to render the resonance visible.

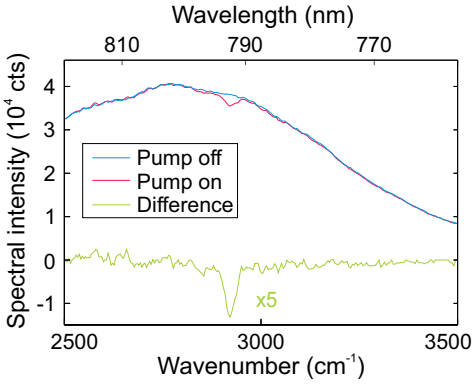

Figure 21: FSRS measurement of acetonitrile: reference spectrum (pump off, blue-dashed curve) and the SRS modulated spectrum (pump on, red curve) showing a small dip at 2921 cm^{-1}. The difference (green curve) corresponds to an inverted Raman intensity spectrum.

3.4 DISCUSSION ABOUT THE APPLICABILITY TO MICROSCOPY

Raman scattering is well suited to be applied as a contrast mechanism for microscopy. With spontaneous Raman scattering being the most mature method, it dominated the field of hyperspectral microscopic imaging for a long time. As already mentioned, spontaneous Raman scattering has considerable disadvantages over CRS, namely the need to apply a confocal approach to allow for three-dimensional imaging, and its rather slow detection, because of the low scattering cross-section. Also, the often apparent disturbance by fluorescent signals in the spectral region of the detection limits the applicability of spontaneous Raman scattering. As already discussed in the introduction of this chapter, the most applied CRS schemes in microscopy up to now are the narrow-bandwidth schemes CARS and SRS.

The broad-bandwidth schemes presented in this section all allow the extraction of the full intensity Raman scattering spectrum at once, which is superior to the narrow-bandwidth approaches, as these are limited by the tunability of the relative frequency between pump and probe pulse. Admittedly, in terms of the acquisition time per image, the narrow-bandwidth approaches are faster, because they do not rely on slow spectrometers with a read out time in the order of milliseconds per pixel, but on fast photodiods combined with lock-in techniques with an acquisition time in the order of microseconds per pixel. Together with the required frequency tuning of the laser and the subsequent recording of images at different narrow spectral bands, the acquisition time of a full broadband hyperspectral data-set increases dramatically. As a consequence, the application of a broad-bandwidth scheme is beneficial, if the full Raman response is desired, for example, if the Raman spectrum of both, the fingerprint region as well as the C-H stretch region is of interest in microscopic investigations.

So far, FRIKES has not been applied to microscopy. The broad-bandwidth approach FSRS has been successfully implemented into a microscopic setup [23], but was apart from this proof-of-principle work mainly employed to spectroscopic tasks, such as presented in [115, 116, 117]. One of the most important limitations of FSRS measurements is its intrinsically noisy retrieved spectrum, which is dominated by detector noise, because a low signal is measured on a huge background, as could be seen in Fig. 21. The novel interferometric developments of the FSRS scheme presented in the next chapter are simple but yet effective extension of the standard FSRS setup, resulting in a superior signal-to-background ratio, as they reduce the background considerably, before actually measuring the Raman scattering spectrum.

4 INTERFEROMETRIC COHERENT RAMAN SCATTERING

CONTENTS

4.1 Interferometric Femtosecond Stimulated Raman Scattering 42
4.1.1 Working Principle, Experimental Setup and Model 43
4.1.2 Experimental Results 46
4.2 In-line Interferometric Femtosecond Stimulated Raman Scattering 49
4.2.1 Experimental Setup 50
4.2.2 Working Principle and Model 51
4.2.3 Experimental Results 55
4.3 Hyperspectral Imaging 59
4.3.1 Experimental Microspectroscopy Setup 61
4.3.2 Experimental Results 63
4.4 Current Limitations and Further Improvements 67
4.5 Summary and Conclusion 68

A variety of different spectroscopic and microscopic techniques are based on coherent Raman scattering (CRS), all of which correspondingly probe the material's third-order nonlinear susceptibility $\chi^{(3)}$. In principle, the two-photon resonant interaction of the incident light fields with molecular vibrational resonances grant access to the amplitude and phase of the probed resonances, which are connected to the imaginary and the real part of $\chi^{(3)}$, respectively. The phase information can greatly improve the spectral resolution and thus the selectivity of CRS, regardless whether the amplitude and phase information are viewed separately [118] or together [119], yielding characteristic dispersive lineshapes with a linewidth below half the natural linewidth of the resonance [120].

Up to the work of the present PhD thesis, the acquisition of the phase information was only realized in narrow-bandwidth CRS schemes, as in optical heterodyne-detection RIKES (OHD-RIKES [121]) or the recently developed balanced-detection RIKES (BD-RIKES [122]). The majority of the CRS schemes is restricted to probing the imaginary part of $\chi^{(3)}$, such as stimulated Raman scattering (SRS [17]), Raman-induced Kerr-effect spectroscopy (RIKES [114]), and coherent anti-Stokes Raman scattering (CARS [110]). In order to utilize the improved resolution and selectivity for hyperspectral scanning microscopy applications, the acquisition of amplitude and phase spectra can be performed by using a broad excitation spectrum, as it was presented in Chap. 3. A narrow-

band laser wavelength scanning approach yields up to video-rate microscopic images [123], but the spectral information is limited to only one single frequency per image. In a broadband scheme, however, the full spectroscopic information is recorded for each pixel, avoiding the necessity to record the same image with different excitation wavelengths, which is beneficial, if the full Raman spectrum is of interest.

Another common limitation encountered with nonlinear spectroscopic investigations is the inherently low signal strength of nonlinear optical processes. The efficiency of parametric processes increases with increasing intensity of the driving laser, however, such scaling is often impossible, because of the damage threshold of the sample under investigation. Nonetheless, a number of techniques routinely enable the utilization of the nonlinear response, such as amplitude modulation of the driving laser and detection with a lock-in amplifier, which relies on subtracting an electronic background signal [17, 18, 124], or optical methods such as heterodyne detection [125, 126]. These methods have been applied to narrow-bandwidth CRS schemes only.

Both issues, the acquisition of the phase information and the restrictions of the narrow-bandwidth approaches are resolved with the two novel interferometric extensions of FSRS, which are presented in this chapter, namely interferometric femtosecond stimulated Raman scattering (iFSRS, Sec. 4.1) and in-line interferometric femtosecond stimulated Raman scattering (II-FSRS, Sec. 4.2). Both share an interferometric approach to reduce the background of the FSRS measurement and additionally give access to phase information of the Raman resonance, in the first case with a Sagnac interferometer and in the second case with an in-line interferometer. The latter realization is actually capable of being incorporated into a microscopic setup, to perform hyperspectral imaging, which will be presented and discussed in Sec. 4.3.

4.1 INTERFEROMETRIC FEMTOSECOND STIMULATED RAMAN SCATTERING

In interferometric femtosecond stimulated Raman scattering (iFSRS) the background of a FSRS measurement is reduced by means of a Sagnac interferometer (SI). SIs are not only used to precisely detect rotation rates [127, 128], or to potentially measure ultrasmall phase shifts in gravitation wave detection [129], but also to improve the observation of ultrafast dynamics [130], or to determine nonlinearities [131], even at the single photon level [132]. Compared to other interferometers, the SI has the advantage that the two interfering beams counter-propagate along the same path, such that all reciprocal phase and amplitude changes cancel out. Only nonreciprocal modulations which are – in our case – due to nonlinear frequency conversion in an unbalanced configuration are detected as a signal at the output port. The application of an interferometric

reduction is the first demonstration of purely optical background suppression for FSRS.

In the following Sec. 4.1.1, firstly the Lorentzian oscillator model is introduced, in order to allow for a theoretical insight into the SRS interaction of the involved pulses. Subsequently, the experimental setup of iFSRS is presented and the performance of the Sagnac interferometer is evaluated experimentally. Sec. 4.1.2 presents experimentally measured iFSRS spectra and compares these to FSRS spectra, which were acquired under the same conditions. Additionally, the aforementioned model is used to calculate the corresponding FSRS and iFSRS spectra for comparison.

4.1.1 Working Principle, Experimental Setup and Model

In order to explain coherent Raman interaction of the pump and probe pulses, we adopt a simple oscillator model [133]. In this frame, the complex third-order susceptibility around a resonance at frequency Ω is described by

$$\chi^{(3)}(\omega) = \frac{A}{\omega - (\omega_{pu} + \Omega) + i\Gamma}, \tag{1}$$

where A is the amplitude, ω_{pu} is the pump frequency and Γ the spectral width of the resonance. Any nonresonant contribution from other processes than the considered Raman transition is neglected in this case. Note that in SRS or FSRS experiments usually only the imaginary part $\mathrm{Im}(\chi^{(3)})$, corresponding to an amplitude change, is detected as gain or loss [17, 18]. In Fig. 22, the real (red curve) and imaginary part (blue curve) of the third-order nonlinear susceptibility $\chi^{(3)}$ are shown for a Raman resonance with a width of Γ = 1.2 THz (40 cm^{-1}) at the central frequency of Ω = 88.35 THz (2957 cm^{-1}). Due to the application of an interferometric, i. e., a phase-sensitive approach for background suppression, an influence of the phase shift inflicted by the resonance (i. e., the real part $\mathrm{Re}(\chi^{(3)})$, red curve in Fig. 22) in the signal detected in iFSRS is expected.

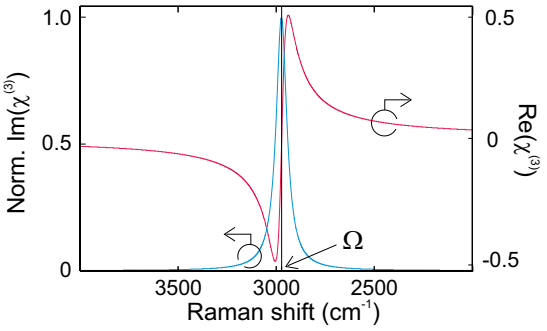

Figure 22: Normalized imaginary part (blue curve) and real part (red curve) of the nonlinear susceptibility $\chi^{(3)}$. The imaginary part corresponds to a Lorentzian shape with width Γ and amplitude A, centered at frequency Ω.

The low magnitude of the third-order susceptibility requires to maintain a careful balance of pulse peak power and average power for a sufficiently high signal yield while avoiding damage to the sample. Even with an optimized ratio, the efficiency is low, leading to signals consisting of a small (~1 %) intensity variation on a large background, i. e., the probe pulse [23]. In contrast, we show that using iFSRS sufficient background suppression can be achieved to facilitate measurement of even lower signal levels. Note that the interferometric method can be used *in addition* to other methods commonly used in SRS, like lock-in techniques, such that the potential for further sensitivity enhancement is fully retained.

The applied pulses had the same properties as the ones used in the FRIKES and FSRS experiments shown in Secs. 3.2 and 3.3. Accordingly, here also loss spectra on the high energy side were measured.

The experimental setup of the SI is shown schematically in Fig. 23. The sample was placed between two lenses (L_1, L_2) of 25 mm focal length inside a three-mirror ring resonator. The probe pulse was split into two counter-propagating parts by a beamsplitter which consisted of two right-angle prisms. The distance between their touching bases was adjusted precisely by a piezo translator (PZT) to control the frustrated total internal reflection (FTIR) at the interface in order to achieve a splitting ratio as equal as possible for the clockwise (cw) and the counter-clockwise (ccw) propagating pulse. The (cw) beam gathered a total phase shift of π during the two reflections at the beamsplitter while the (ccw) beam was transmitted unaffectedly twice, resulting in destructive interference at the output port, rendering it dark.

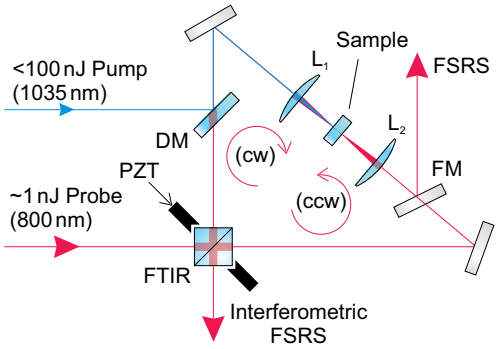

Figure 23: Sagnac interferometer setup for iFSRS measurements. DM: dichroic mirror, L_1, L_2: lenses, FM: flip mirror, (cw): clockwise beam path direction, (ccw): counter-clockwise beam path direction, FTIR: 50:50 beamsplitter (based on frustrated total internal reflection) comprised of two right angle prisms being pressed together with a piezo translator (PZT), shown schematically as the black elements. For details, see text.

The intensity emerging from the SI exit port can be calculated as

$$\begin{aligned} |E_{out}|^2 &= |E_{cw} + E_{ccw}|^2 \\ &= |r^2(\omega)E_{in} \cdot e^{i(\pi+kz)} + t^2(\omega)E_{in}|^2, \end{aligned} \tag{2}$$

where E_{out} is the emerging electric field, E_{in} is the incident electric field, E_{cw} and E_{ccw} are the electric fields after propagation in the clockwise and counter-clockwise direction, respectively. The frequency-dependent reflection and transmission coefficients of the beamsplitter $r(\omega)$ and $t(\omega)$ fulfill the condition $r(\omega) = 1 - t(\omega)$. The Raman contribution is included in the phase term (kz) in the exponent, with the propagation distance z. The wavevector k can be expressed as:

$$\begin{aligned} k &= \frac{\omega}{c} = \omega\sqrt{\mu\epsilon} = \omega\sqrt{\mu_0\epsilon_0(1+\chi)} \\ &= k_0\sqrt{1+\chi} = k_0\sqrt{1+\chi^{(3)}|E_{pu}|^2}, \end{aligned} \tag{3}$$

wherein $|E_{pu}|$ is the pump pulse intensity, $c = 1/\sqrt{\mu\epsilon}$, $\epsilon = \epsilon_0(1+\chi)$, $\mu \approx \mu_0$, $c_0 = 1/\sqrt{\mu_0\epsilon_0}$ and $k_0 = \omega/c_0$ were used. The susceptibility χ is assumed to consist of a third order nonlinearity ($\chi^{(3)}|E|^2$) only.

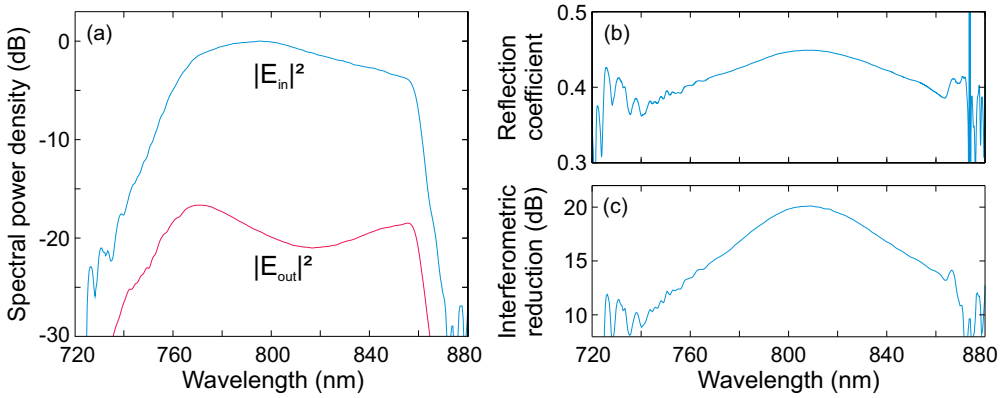

Figure 24: (a) Spectral power density of the probe pulse before the SI ($|E_{in}|^2$, blue curve) and at the exit port of the SI ($|E_{out}|^2$, red curve), (b) the reflection coefficient calculated by Eq. 4 and (c) interferometric reduction achieved by the Sagnac setup on a logarithmic scale.

Fig. 24 (a) shows the measured residual spectral intensity of the probe pulse emerging from the SI exit port ($|E_{out}|^2$) as the red curve on a logarithmic scale. The emerging pulse energy amounted to 12 pJ. Care was taken not to saturate the spectrometer at this intensity, so neutral density filters were inserted in front of the spectrometer. The probe pulse spectrum incident to the SI ($|E_{in}|^2$) is shown as a blue curve for comparison. The shape of the residual probe spectrum was a result of the wavelength-dependent splitting ratio of the FTIR beamsplitter and of other imperfections in the setup. The reflection coefficient $r(\omega)$,

which is depicted in Fig. 24 (b), was derived from the measured spectra in Fig. 24 (a) by:

$$r(\omega) = \frac{1}{2}\left(1 - \sqrt{\frac{|E_{out}(\omega)|^2}{|E_{in}(\omega)|^2}}\right). \tag{4}$$

The resulting interferometric reduction shown in Fig. 24 (c), reached its maximum value of 21 dB at 805 nm and decreased to both sides of the spectrum. The overall background suppression of the Sagnac interferometer amounted to 17 dB, which was measured as the power suppression at the SI output port, compared to the input probe pulse power of 0.6 nJ. Note that in a different context, namely the observation of the Kerr-effect in a fiber with a SI, an even stronger suppression has been obtained with narrow-bandwidth pulses, enabling measurements at the single photon level [132]; for the broad bandwidth of the probe spectrum of about 100 nm and the corresponding difficulties with, e. g., the equal as possible splitting ratio of the beamsplitter, however, 17 dB is a considerable overall performance.

The pump pulse was coupled into the SI via a dichroic mirror (DM), which was highly reflective for the pump wavelength and transmissive for the probe wavelength. The pump pulses were spatially and temporally overlapped with the (cw) probe pulse, while temporal overlap with the (ccw) probe pulse in the sample was avoided. SRS could occur only in the (cw) direction, thereby generating an imbalance of the SI. Furthermore, a flip mirror (FM) was installed behind the sample and lens L_2, which could be used to redirect the cw-propagating probe pulse to measure conventional FSRS for comparison. Both, FSRS as well as iFSRS spectra were acquired using a spectrometer based on a silicon CCD-array with a spectral resolution of 0.8 nm (Stellarnet EPP2000).

4.1.2 Experimental Results

Demonstration measurements of FSRS and iFSRS were performed with a bulk sample of Poly(methyl methacrylate) (PMMA) of unknown purity and of 6 mm thickness. PMMA shows a strong Raman-active resonance in the C-H stretch region at 2957 cm^{-1}, such that the Raman loss was expected to appear in the probe spectrum at a wavelength of about 792 nm. The FSRS measurement is shown in Fig. 25 (a) as the red curve, while the blue curve shows the reference spectrum of the unaltered probe pulse behind the sample. The latter was measured not by blocking the pump pulse, but with the pump pulse delayed from temporal overlap, such that distortions, e.g., due to thermal lensing occurred in both measurements with an identical amount and were not misinterpreted as gain or loss.

The Raman loss induced by the PMMA resonance is visible near the maximum of the probe spectrum in Fig. 25 (a). By calculating the difference between

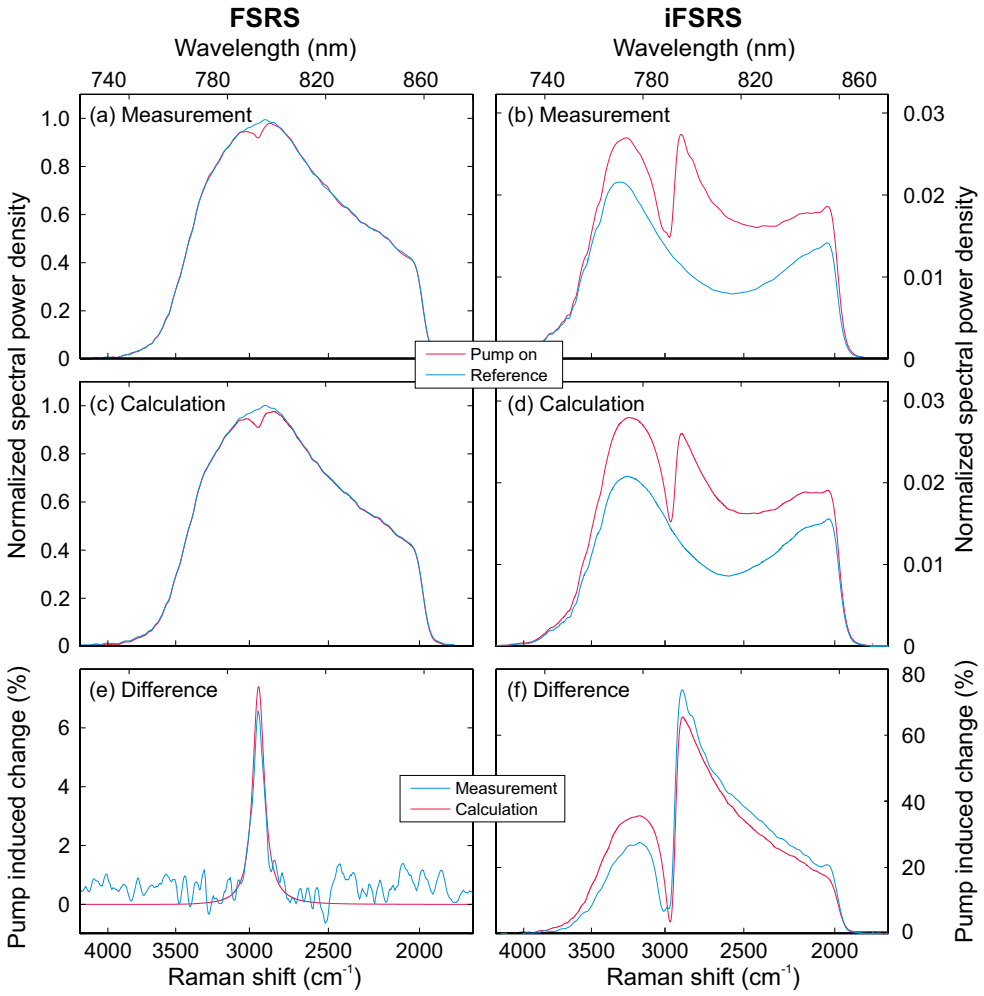

Figure 25: FSRS (left column) and iFSRS (right column) spectra of PMMA: (a, b) measured spectra and (c, d) spectra recreated by applying the Lorentzian resonance to the measured probe pulse. For all cases the probe spectrum is displayed without (blue curve) and with temporal overlap with the pump pulse (red curve). (e, f) The pump induced change of the measurement (red curve) and the calculation (blue curve).

the reference spectrum and the FSRS spectrum the Raman intensity spectrum was retrieved and is shown as the blue curve in Fig. 25 (e). A main Raman peak at 792 nm (2957 cm^{-1}) is well resolved. The magnitude of the Raman loss, i. e. the signal-to-background ratio (S/B-ratio) was approximately 0.06:1 in this measurement. This relatively high signal strength and low noise level were a result of the high peak power of the laser system in combination with a high repetition frequency of 1 MHz, which resulted in clearly resolved spectra. In comparison, reported results where comprised of 1000 single spectra, which were averaged and thereby created comparable results [23]. The signal-to-noise ratio (S/N-ratio) was dominated by the detector noise and could be estimated from Fig. 25 (e) to be ~6:1. Note that a further enhancement of the S/N-ratio with post-processing techniques like averaging or numerical smoothing is possible.

For comparison, we calculated a FSRS spectrum by applying the simple model for a Lorentzian shaped resonance (Eq. 1) with Γ = 1.2 THz (40 cm^{-1}) to the measured probe spectrum from Fig. 25 (a), which is shown in Fig. 25 (c). The probe spectrum ($|E_{in}|^2$, blue curve) now displays a symmetric loss profile ($|E_{in}|^2 \cdot e^{i(\pi+kz)}$, red curve) at the central frequency of Ω = 2957 cm^{-1}. By taking the difference of both curves (shown in Fig. 25 (e) as the red curve), the Raman intensity spectrum is clearly visible, which corresponds to the imaginary part of the assumed Lorentzian resonance. The resemblance of both, the loss spectra in Figs. 25 (a) and (c) and the direct comparison of the difference spectra in Fig. 25 (e) shows that the shape of the absorptive loss spectrum is well approximated by the simple Lorentzian oscillator model.

The iFSRS spectra were recorded with the flip mirror removed, such that the SI ring was forming a closed path, while all the other experimental parameters were kept identical to the FSRS measurement. A PMMA spectrum measured at the SI output port is shown in Fig. 25 (b) as the red curve and the probe pulse spectrum (with the pump pulse delayed) is plotted as the blue curve for comparison. The background suppression by the SI led effectively to an increase of the signal-to-background ratio from 0.06:1 to about 1:1 and to an increased signal-to-noise ratio from approximately 6:1 to about 160:1. The latter was possible, because iFSRS enabled the exploitation of the dynamic range of the spectrometer to its full capacity. The background spectrum could be easily subtracted (see the blue curve in Fig. 25 (f)).

In addition to the achieved improvement in sensitivity, and in contrast to the FSRS measurements, the interferometrically measured Raman loss spectrum revealed a dispersive lineshape, which is the typical phase signature of a resonance. In order to reproduce this signature, the model of a Lorentzian shaped resonance was applied to the measured probe pulse ($|E_{in}|^2$) and the resulting spectrum ($|E_{in} \cdot e^{i(\pi+kz)}|^2$, i. e., the one plotted in Fig. 25 (c) as the red curve) was further processed together with the unaltered probe spectrum ($|E_{in}|^2$, the

blue curve in Fig. 25 (c)) to generate the SI output according to Eq. 2 (where the reflection coefficient r from Fig. 24 (b) was used). It can be seen from the result shown in Fig. 25 (c) that not only the shape of the reduced spectrum (blue curve), but also the shape of the spectral modulation (red curve) was reproduced in good agreement with the measurement. The direct comparison in Fig. 25 (f) is a clear demonstration that the interferometric detection of FSRS measurements grants access to the phase of a nonlinear resonance, i. e., to the real part of $\chi^{(3)}$, and that the shape of this dispersive phase function can be modeled with the help of the simple model for a Lorentzian oscillator.

4.2 IN-LINE INTERFEROMETRIC FEMTOSECOND STIMULATED RAMAN SCATTERING

The iFSRS scheme does in principle allow single-shot measurement of the spectral amplitude and additionally of the phase, but the experimental setup involving a Sagnac interferometer is quite sensitive to wavefront distortions, which are likely to occur in a microscopic setup, such that the applicability of iFSRS to imaging is limited. Related techniques like optical heterodyne-detection RIKES (OHD-RIKES [121]) or the recently developed balanced-detection RIKES (BD-RIKES [122]) also grant access to the phase, but the shape of the resonance is obtained only by scanning the excitation wavelength, because both schemes are narrow-bandwidth CRS schemes.

Here, this gap is closed and potentially a single-shot access to the amplitude as well as the phase of the Raman spectrum over a wide wavenumber range of 1000 cm^{-1} is provided, which can additionally be applied to imaging applications: in-line interferometric FSRS (II-FSRS) combines the advantages of the phase-sensitive heterodyne- or balanced-detection schemes (as applied in OHD-RIKES or BD-RIKES) and of the broadband femtosecond schemes (like FSRS and FRIKES). Additionally, the accompanying background reduction yields results comparable to the schemes (F)RIKES, ASTERISK [134], the aforementioned background-free CARS [113] and iFSRS [119]. The main idea of II-FSRS is to use two identical probe pulses, which share a common path and are only separated by their polarization. The perpendicularly polarized probe pulse components experience different nonlinear contributions from the pump-probe interaction and are brought into interference afterwards. This technique has already been used in an optical switching experiment [135] or later for the detection of the full complex response of gold nanoparticles [136]. The information that can be gained from the II-FSRS spectrum depends on the polarization configuration of the complete setup: in one configuration, the spectrum corresponds to a Raman intensity spectrum like in FSRS, but with a strongly reduced background. In the other configuration, the phase information of the resonance becomes apparent in characteristic dispersive lineshapes.

In the next Sec. 4.2.1, the experimental setup for II-FSRS is laid out. To examine the different possible contributions to the II-FSRS spectra, an analytic model is introduced in Sec. 4.2.2, which is also based on the Lorentzian oscillator model and which is calculated with the Jones matrix formalism. In Sec. 4.2.3, our new II-FSRS scheme is compared to the common nonlinear Raman scattering spectroscopy methods FSRS (see Sec. 3.3) and FRIKES (see Sec. 3.2), which are both applicable with only slight changes of the setup. The measured II-FSRS spectra are also reproduced by the analytic model. The excellent agreement between experiment and theory allows for the retrieval of the Raman intensity and phase spectrum from the measurement.

4.2.1 Experimental Setup

In order to measure both, the amplitude and the phase of the spectrum, FSRS was realized within an in-line interferometric setup as shown in the schematic sketch in Fig. 26 (a). The experimental scheme was based on the FSRS experiment from Sec. 3.3, which we employed by detecting the loss spectrum on the anti-Stokes side. The pump and probe pulses were both identical to the ones used in these experiments. In Fig. 26 (b) the polarization states of the involved pulses are indicated. The probe pulse (red) was initially set to linear polarization along the x-axis, which was ensured by a polarizer (Pol1). It was then separated into two components by an achromatic quarter-wave plate (QWP1) where the fast axis was aligned at +45° with respect to the x-axis (here and in the following, all angles are given with respect to the x-axis, i. e., to the horizontal direction in Fig. 26). The two probe pulse components then had orthogonal polarizations (at $\pm 45°$) and were delayed with respect to each other by $\pi/2$ (corresponding to a circular polarization).

The pump pulse energy was adjusted by a variable neutral density filter (ND). The pump pulses passed a polarizer (Pol2), a quarter-wave plate (QWP2) and a half-wave plate (HWP) such that any arbitrary polarization state could be accomplished. The pump and probe pulses were superimposed to spatially and temporally overlap using a dichroic mirror (DM). A 20× microscope objective (MO) created a focus in the sample to initiate a polarization-dependent coherent Raman scattering interaction, and the light was collected behind the sample by a second 20× MO. Afterwards, the pump pulse was filtered out using a second DM, while the achromatic QWP3 transformed the probe pulse back into a linear polarization state, now at 90°. The light was detected behind a polarizer (Pol3) which was set to transmit polarization components at 0° only. The spectrum of the probe pulse behind Pol3 was recorded with a spectrometer based on a silicon CCD-array with a spectral resolution of 0.8 nm at 800 nm (Stellarnet EPP2000), identical to the one used in Secs. 3.2 and 3.3.

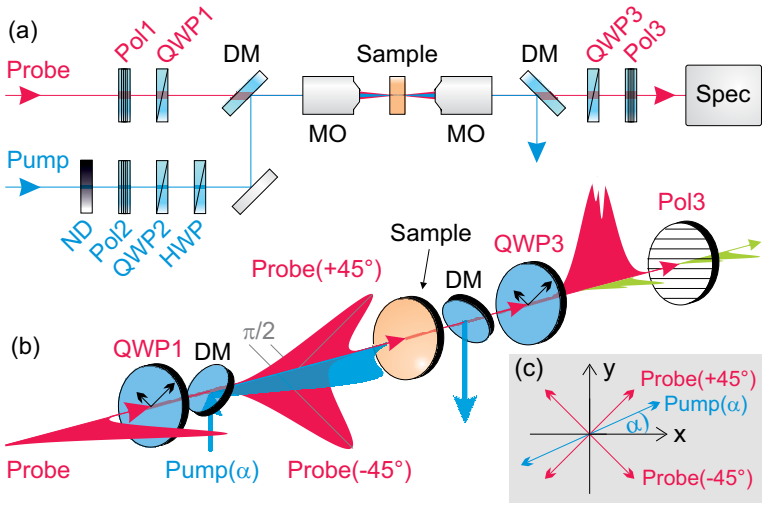

Figure 26: (a) Schematic experimental setup. ND: neutral density filter, Pol#: polarizer, QWP#: quarter-wave plate, HWP: half-wave plate, DM: dichroic mirror, MO: microscope objective, Spec: spectrometer. (b) Schematic sketch of the II-FSRS scheme. (c) The inset shows the polarization orientations of the pump and probe pulse components in the sample (details see text).

With no pump pulse and thus no nonlinear interaction being present, the polarization of the probe pulse before Pol3 should be at exactly 90°, i. e., vertical, and there should be no signal detectable behind Pol3, which is set to 0°. However, in presence of the linearly polarized pump beam, polarization-dependent FSRS was introduced in the sample, i. e., a nonlinear amplitude and phase modulation of the two differently polarized probe pulse components occurred. This corresponded to a change of the polarization state of the probe pulse from the original circular polarization before QWP3 and consequently from the vertical polarization behind QWP3.

In addition to the intended polarization change due to FSRS, we have identified two additional parasitic contributions to a signal behind Pol3: firstly, there were imperfections of the setup. Especially the quarter-wave plates showed a wavelength-dependent retardation error, resulting in a wavelength-dependent state of polarization of the probe pulse and thus an unavoidable linear background signal in the experiment. Secondly, cross-phase modulation (XPM) altered the state of polarization of the probe beam. All these contributions to the II-FSRS spectra, the intended as well as the parasitic ones, are individually addressed in the following section 4.2.2.

4.2.2 Working Principle and Model

In this section the described II-FSRS scheme will be evaluated theoretically using the Jones matrix formalism. The goal of this process is to identify the accessible spectral information for different polarization configurations. Furthermore,

by reconstructing every process in the setup that changes the phase and/or amplitude, the II-FSRS spectra will be reproduced theoretically, and so the verification of the validity of our approach is possible.

The II-FSRS scheme is based on the amplitude and phase modulation of the probe pulses by stimulated Raman scattering, which depends on the polarization angle of the pump pulse. In a simple approximation, this resonant Raman scattering contribution can be described by an oscillator model for the complex third-order susceptibility $\chi_r^{(3)}$ around a resonance at frequency Ω. Here we follow Ref. [133] and neglect the tensor characteristics of the susceptibility, which leads to a reasonable comparability to our experiment, indicating that the influence of the neglected components of the tensor is rather weak.

As stated above, XPM [137] can contribute to a polarization rotation of the probe pulse, besides the resonant stimulated Raman scattering in II-FSRS. XPM occurs due to a nonresonant, wavelength-independent third-order nonlinearity $\chi_{nr}^{(3)}$ and can be described as a phase shift experienced by each of the two polarization components E_x and E_y of the probe pulse. For isotropic media, XPM contributes a relative phase shift of $2/3$ to the polarization parallel to the pump pulse, and of $1/3$ to the perpendicular polarization [137]. The resulting phase difference means that XPM acts on the probe pulse polarization like a retardation plate. A combination with a circular pump polarization like in FRIKES would result in an evenly distributed nonlinear effect, including the nonresonant, but also the resonant contributions, on both probe pulse polarization components and would cancel out. Because the resonant contribution is of interest, the II-FSRS measurements need to be carried out with a linear pump polarization, resulting in an unavoidable nonlinear, but nonresonant XPM background, which has already been observed in BD-RIKES [122].

The influence of the nonlinearities (Eq. 1 and XPM) on a pulse can be calculated by including the contributions of the third-order susceptibilities into the wavevector k in the phase term $\Phi = \exp(ikz)$ and multiplying it to the electric field E_{in}, where z is the propagation distance. We distinguish between two cases: first, if the electric field experiences resonant Raman scattering as well as nonresonant XPM, the wavevector $k_{\parallel}$ can be expressed as

$$\begin{aligned} k_{\parallel} &= \frac{\omega}{c} = \omega\sqrt{\mu\epsilon} = \omega\sqrt{\mu_0\epsilon_0(1+\chi)} \\ &= k_0\sqrt{1+\chi} = k_0\sqrt{1+(\chi_r^{(3)} + 2/3\cdot\chi_{nr}^{(3)})|E_{pu}|^2}. \end{aligned} \tag{5}$$

Here, $|E_{pu}|$ is the pump pulse intensity, $c = 1/\sqrt{\mu\epsilon}$ as the velocity of light within the medium, $\epsilon = \epsilon_0(1+\chi)$, $\mu \approx \mu_0$, $k_0 = \omega/c_0$ and $c_0 = 1/\sqrt{\mu_0\epsilon_0}$ were used, and the susceptibility χ was assumed to consist of a third order nonlinear contribution ($\chi^{(3)}|E|^2$) only.

In the second case the electric field only experiences XPM and the wavevector $k_\perp$ can be written as

$$k_\perp = k_0\sqrt{1+1/3\cdot\chi_{nr}^{(3)}|E_{pu}|^2}. \tag{6}$$

In the Jones-matrix formalism [138], the electric field is written in the form

$$E = \begin{bmatrix} E_x \\ E_y \end{bmatrix}, \tag{7}$$

where E_x and E_y are the aforementioned polarization components in x- and y-direction, respectively. The nonlinear interaction in the sample is modeled by the matrix

$$M_{Raman} = \begin{bmatrix} \exp(ik_\parallel z) & 0 \\ 0 & \exp(ik_\perp z) \end{bmatrix} = \begin{bmatrix} \Phi_\parallel & 0 \\ 0 & \Phi_\perp \end{bmatrix}. \tag{8}$$

Applying M_{Raman} to an electric field E_{in}, i. e., calculating $E_{out} = M_{Raman}\cdot E_{in}$ yields an electric field, where the x-component is modulated by $\Phi_\parallel$ and the y-component is modulated by $\Phi_\perp$. This corresponds to a case, where the pump polarization orientation coincides with the x-axis.

The effect of a QWP with a fixed orientation of the fast axis of 0° on the electric field is calculated by

$$M_{QWP} = \frac{1}{\sqrt{2}}\begin{bmatrix} 1-i & 0 \\ 0 & 1+i \end{bmatrix}. \tag{9}$$

In order to consider a QWP with the fast axis at 45°, as it was used in the setup, the electric field is rotated by -45° before the QWP, and rotated back (by +45°) after the QWP. This results in the sequence $M_R(\Theta)\cdot M\cdot M_R(-\Theta)$ with the rotation matrix M_R:

$$M_R(\Theta) = \begin{bmatrix} \cos(\Theta) & -\sin(\Theta) \\ \sin(\Theta) & \cos(\Theta) \end{bmatrix}. \tag{10}$$

The experimental setup, as presented in Fig. 26, is accordingly modeled by the following sequence of matrices acting on the incident probe pulse field E_{in} to calculate E_{out}:

$$\begin{aligned} E_{out} =& M_R(45°)\cdot t\cdot M_{QWP}\cdot M_R(-45°)\cdot M_R(\alpha)\cdot M_{Raman} \\ & \cdot M_R(-\alpha)\cdot M_R(45°)\cdot M_{QWP}\cdot M_R(-45°)\cdot E_{in} \\ =& -1/4\cdot E_{in} \\ & \cdot(\Phi_\perp\cdot(-i-1-t+it+2\cos^2(\alpha)(1+t)-i\sin(2\alpha)(1+t)) \\ & +\Phi_\parallel\cdot(-i+1+t+it-2\cos^2(\alpha)(1+t)+i\sin(2\alpha)(1+t))). \end{aligned} \tag{11}$$

Here, α is the pump polarization angle and $t = t(\lambda)$ is a transfer function including the imperfections of the waveplates in the experimental setup. Even though care was taken to choose achromatic QWPs, they still showed a wavelength-dependent retardation error, which led to the aforementioned unwanted contribution to the signal measured behind Pol3. The retardation error $t(\lambda)$ of the system could be determined from a measurement without a pump pulse. In this case, $\Phi_{\parallel} = \Phi_{\perp} = 1$ in Eq. 11, and we obtain

$$E_{out} = -1/2 \cdot i(t-1) \cdot E_{in} \quad \Leftrightarrow \quad t = \frac{2\,i\,E_{out}}{E_{in}} + 1. \tag{12}$$

In the following, we qualitatively explain the coherent Raman contributions to the probe pulse components and the expected observation for one exemplary case, namely for a pump pulse polarization at 45°, for $\alpha_{QWP2} = \alpha_{QWP3} = 45°$ and for detection behind polarizer Pol3 ($\alpha_{Pol3} = 0°$). In the case of an absent pump pulse, the two probe pulse components after QWP1 leave the sample unchanged, are recombined behind QWP3 to a pulse linearly polarized at 90°, and consequently no light is detected behind a polarizer rotated to 0°. With a pump pulse set to 45° ($\alpha_{QWP1} = 0°$ and $\alpha_{HWP1} = 22.5°$), however, the pump pulse polarization is parallel to one of the probe pulse components at +45° and perpendicular to the other at -45°, such that coherent Raman interaction is initiated only in the parallel case. This imbalance leads to a change of the polarization state of the total probe wave behind QWP3, such that Pol3 no longer blocks all light and a non-zero signal is detected by the spectrometer. Due to the interference of the two components, the transmitted light carries amplitude as well as phase information of the Raman resonance, which results in a dispersive lineshape in the spectrum, very similar to the ones observed in iFSRS presented in Sec. 4.1 and in [119].

By simply changing the pump pulse polarization in II-FSRS, the desired lineshape can be adjusted (Raman loss, Raman gain spectrum and dispersive lineshape signatures). These significant polarization settings are listed in Table 1, together with the applied settings for FRIKES and FSRS in Sec. 3.2 and Sec. 3.3, respectively.

Table 1: Waveplate and polarizer orientations (in degrees, with respect to x-axis, i. e. horizontal orientation) for the different schemes, * = not inserted, RL: Raman loss, RG: Raman gain, DL: dispersive lineshape.

Scheme	QWP1	HWP	QWP2	QWP3	Pol3
II-FSRS (RG / RL)	45	0 / 45	0	45	0
II-FSRS (DL / -DL)	45	22.5 / 67.5	0	45	0
FSRS	*	*	*	*	0
FRIKES	*	0	45	*	90

4.2.3 Experimental Results

This section describes the measurement of the Raman resonance of acetonitrile, as an exemplary sample, with different methods. First, the spontaneous Raman emission was recorded in the separate setup, as presented in Sec. 3.1, as an independent comparison to the nonlinear methods. The subsequently presented FSRS, FRIKES and II-FSRS measurements of acetonitrile were all recorded with the same pulse parameters and with pulse energies of 30 nJ and 1.4 nJ for the pump and the probe pulses, respectively. The setup was kept identical for all measurements. Only the detector integration time was adjusted for each measurement and the polarization optics were arranged for the individual methods as it was discussed in the theory Sec. 4.2.2.

For the II-FSRS measurement, the polarizer and waveplates were adjusted according to table 1. After a careful alignment of QWP1 and QWP3 to $\alpha_{QWP1} = \alpha_{QWP3} = 45°$ and with no pump pulse present, the probe pulse energy transmitted through Pol3 was as low as 4.2 pJ, compared to an incident probe pulse energy of 1.4 nJ before the sample. In order to avoid a saturation of the spectrometer at 20 ms integration time, the incident light had to be attenuated by a 10 dB neutral density filter.

Fig. 27 (a) displays the transmitted probe pulse spectrum together with the incident spectrum (red and blue curves, respectively) on a logarithmic scale, showing a background reduction of more than 25 dB over the whole spectral range from 750 to 840 nm. The shape of the transmitted probe pulse spectrum is a result of an imperfect setup, wherein the wavelength-dependent retardation error of the QWPs is most dominant. This error $t(\lambda)$ of the system was calculated from the measurement in Fig. 27 (a) according to Eq. 12 and is plotted in Fig. 27 (b). The minima of the function $t(\lambda)$ at the wavelengths around 755 nm and 832 nm are due to the two design wavelengths of the achromatic QWPs.

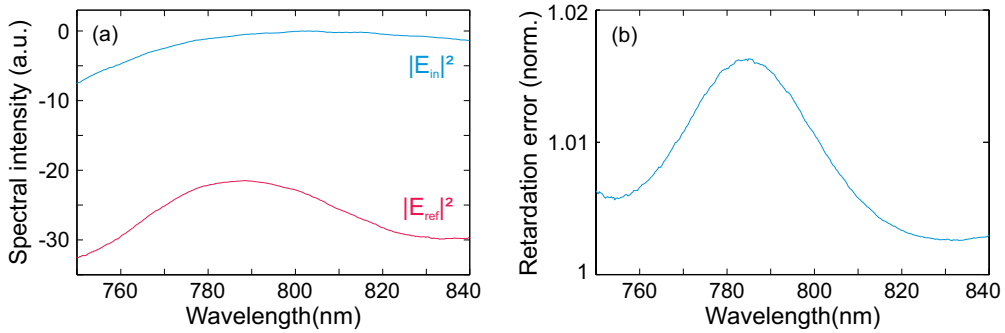

Figure 27: (a) Incident probe pulse spectrum (blue curve) and transmitted reference spectrum behind Pol3 (red curve) in the II-FSRS setup on a logarithmic scale. (b) Retardation error, normalized to a retardation of $\lambda/4$, of the experimental system calculated from (a) according to Eq. 12.

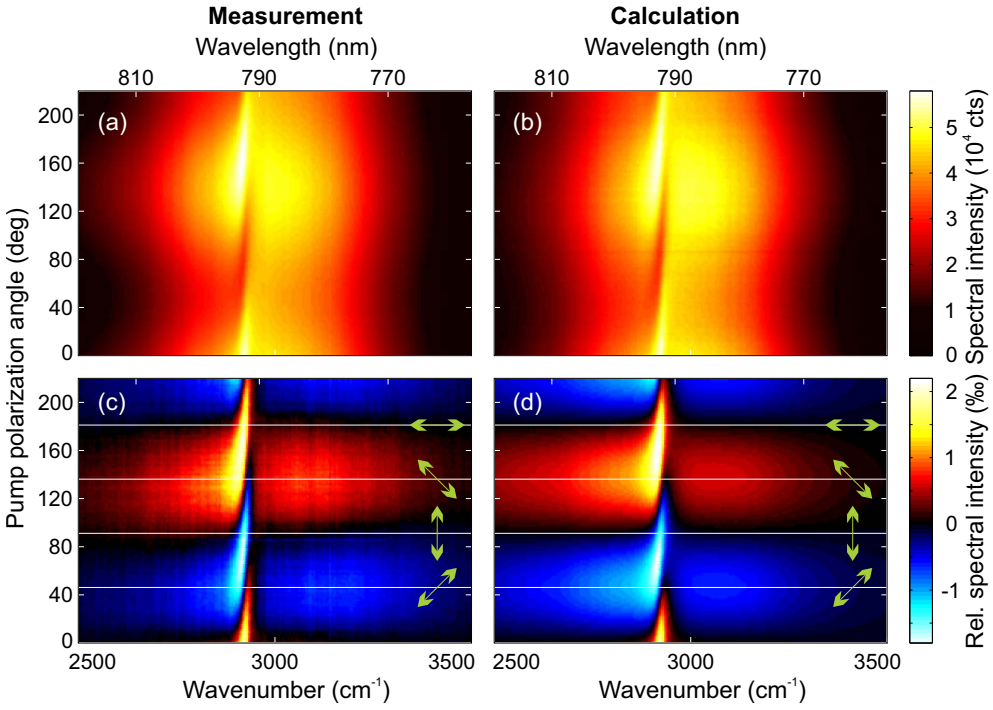

Figure 28: (a) Measured and (b) calculated II-FSRS spectrum dependent on the pump pulse polarization, (c) the same measured and (d) calculated spectra subtracted by the corresponding reference spectrum. The arrows in (c) and (d) indicate the pump polarization angle.

Stimulated Raman scattering was induced by superimposing the pump pulse such that it temporally and spatially overlapped with the probe pulses in the sample. In this case, the II-FSRS spectrum depended on the pump polarization angle as explained in Sec. 4.2.2. A corresponding measurement is shown in Fig. 28 (a), where successive spectra were taken at different pump polarization angles. The spectral intensity is shown in false colors on a linear scale. The dominant resonance of acetonitrile is easily identified in the probe spectrum at 792.4 nm on top of the aforementioned residual background (see Fig. 27 (a), red curve).

For a better visualization of the nonlinear contributions, Fig. 28 (c) shows the II-FSRS measurement with the residual background being subtracted. The color scale now refers to the spectral intensity relative to the incident probe pulse spectrum. From Fig. 28 (c) it is clearly visible that the spectral feature at the resonance changes from a gain signature at a horizontal pump pulse polarization, over a dispersive lineshape at 45° and a loss at vertical polarization to an inverted dispersive lineshape at 135°, continuously repeating this cycle.

The measurement was reproduced using the analytic model presented in Sec. 4.2.2. The Lorentzian resonance (Eq. 1) was fitted to the measurement with a width of $\Gamma = 28\,\mathrm{cm}^{-1}$ at a resonance frequency of $\Omega = 2921\,\mathrm{cm}^{-1}$. The incident probe pulse spectrum E_{in} (the blue curve in Fig. 27 (a)) and the retardation error

t(λ) (Fig. 27 (b)) were inserted into Eq. 11 and the result is plotted in Fig. 28 (b). Again, for a better visibility of the nonlinear contributions, the reference spectrum was subtracted, which resulted in the spectra depicted in Fig. 28 (d). As can be seen by comparing the calculation with the measurement in Fig. 28 (c), all features are well reproduced.

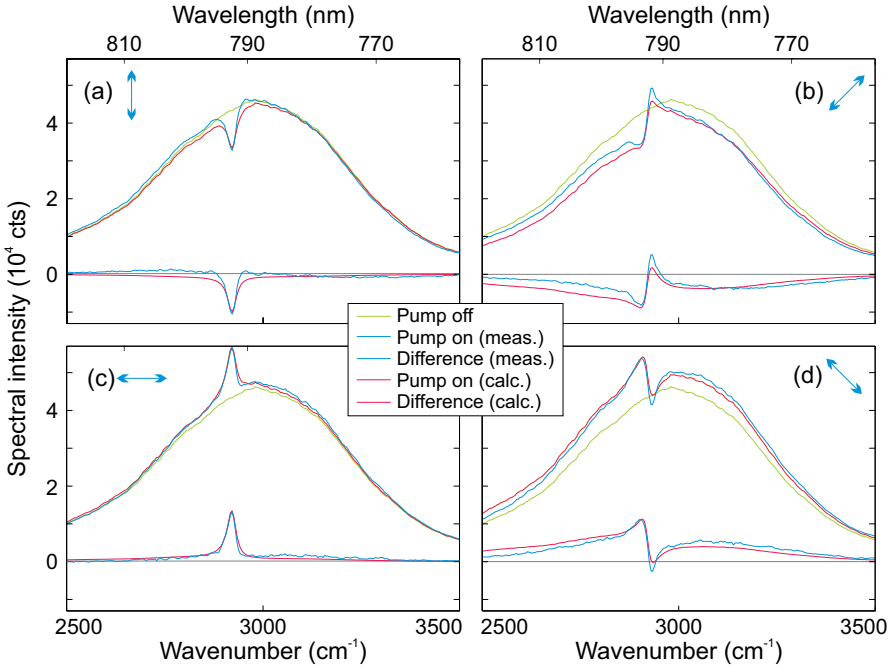

Figure 29: Measured (blue curves) and calculated (red curves) II-FSRS spectra at pump pulse polarization angle of (a) 0° (≡180°), (b) 45°, (c) 90° and (d) 135°.

For a direct juxtaposition, the significant pump pulse polarization angles (0° (≡180°), 45°, 90° and 135°) are marked with white-dashed lines in both Figs. 28 (c) and (d), and the corresponding cuts are shown in Fig. 29. The position, shape and width of the spectral lineshapes in the measurement (blue-dashed curves) are reproduced well from the calculations (red-dashed curves) for all polarization arrangements. After subtracting the residual background (green curve), the spectra in Figs. 29 (a) and (c) show a clear intensity Raman scattering signature (solid curves), only with a different sign. The critical alignment of the two imperfect QWPs mainly causes the slight variance in the baseline.

In Figs. 29 (b) and (d), the expected dispersive lineshapes are apparent, also differing in their sign. Additionally, the nonresonant XPM-induced phase shift lowers the signal for the case of a pump polarization angle of 45° (Fig. 29 (c)) and elevates it for 135° (Fig. 29 (d)), due to the interference conditions. These contributions are also well reproduced within the calculations (red curves).

In these II-FSRS measurements, the signal level of the Raman signatures (e.g. the loss feature in Fig. 29 (a), blue curve) is 10000 cts, resulting in a S/N-ratio of 156:1, while the S/B-ratio is 1:5. Comparing the FSRS loss spectrum (presented

in Sec. 3.3 and recapitulated in Fig. 30 (a)) and the II-FSRS spectra, it is clear that the visibility of the Raman signatures was improved significantly by the application of the in-line interferometer. Although the generated signal strength is slightly stronger in FSRS compared to II-FSRS, because here the application of the circularly polarized probe pulse and the detection through the crossed polarizer effectively reduced the signal, the background reduction in II-FSRS allows to exploit the dynamic range of the detector considerably more, and thus raises the S/B-ratio by a factor of three and the S/N-ratio by a factor of four.

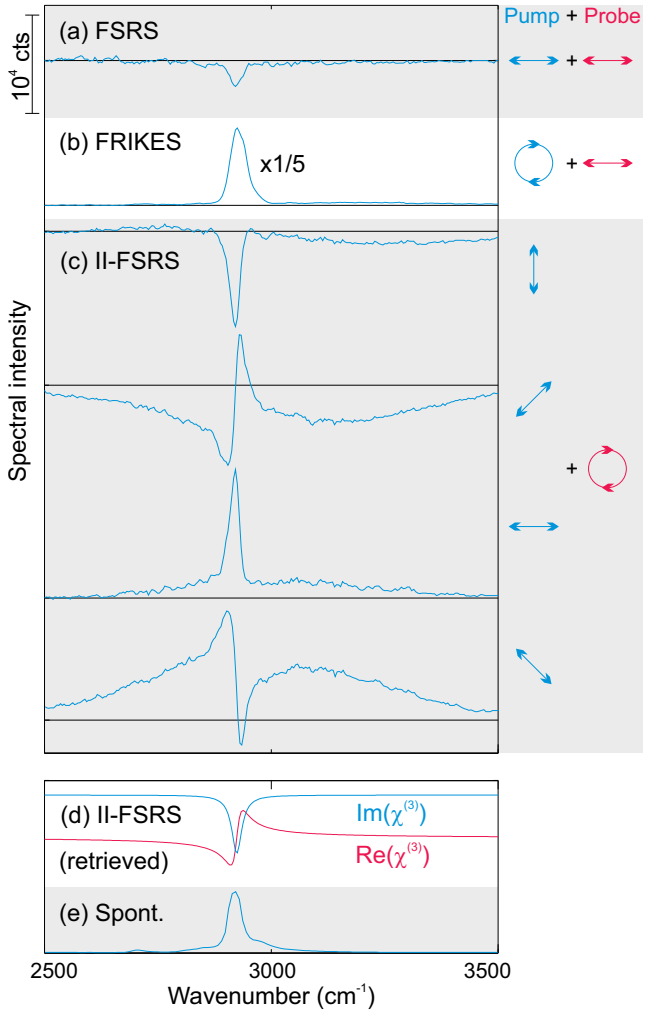

Figure 30: Comparison of the different spectroscopy methods. The FSRS (Sec. 3.3), FRIKES (Sec. 3.2) and II-FSRS spectra were obtained with the same pulse parameters, only with different orientations of polarization, as indicated by the arrows on the right side. The retrieved nonlinear susceptibility $\chi^{(3)}$ is shown in the plot below, together with the independently measured spontaneous Raman spectrum (Sec. 3.1) for comparison.

For a comparison of the different presented Raman scattering spectroscopy schemes, the measured spectra of acetonitrile are plotted on top of each other in

Fig. 30. With the exception of the spontaneous Raman scattering spectrum, all spectra were recorded with the same laser system, pulse parameters and spectrometer. The FSRS spectrum (Fig. 30 (a)) is intrinsically noisy, because a small signal is measured on a high background. The FRIKES spectrum (Fig. 30 (b)) is superior as far as the noise level is concerned, but it had to be recorded with a higher acquisition time, because of the low signal level, making it the slower scheme. The lineshapes of both FSRS and FRIKES resemble the spontaneous Raman scattering spectrum (Fig. 30 (e)). The quality (concerning signal level and noise level) of the II-FSRS measurement (Fig. 30 (c)) can be ranked in-between FSRS and FRIKES. A clear loss (gain) spectrum emerges in the case of vertical (horizontal) pump pulse polarization, while for a pump pulse polarization of $\pm 45°$ dispersive lineshapes are obtained. The dispersive lineshapes suffer from the background due to the nonresonant XPM contribution, but they also grant access to the phase of the resonance (imaginary and real part of $\chi^{(3)}$ as shown in Fig. 30 (d)), enhancing the spectroscopic information and thereby the spectral resolving power of II-FSRS.

4.3 HYPERSPECTRAL IMAGING

Coherent Raman scattering (CRS) techniques are widely applied to generate a label-free contrast in microscopic applications. As discussed earlier in this thesis, all CRS methods rely on the coherent excitation of vibrational resonances in the sample under investigation. The most prominent approaches to make use of molecule-specific Raman resonances as a contrast mechanism for a microscope employ two narrow-bandwidth picosecond pulses, with the difference frequency between these two matching one Raman resonance. These light fields are either used to generate a coherent anti-Stokes Raman scattered (CARS [15, 16]) signal, or to induce stimulated Raman scattering (SRS [17, 18]). With these schemes, high-speed acquisition of an image (up to video-rate [123]) is possible by probing one specific vibrational resonance in the sample. To change this contrast to another vibrational resonance, the central frequency of one of the pulses has to be changed. In this way, a multi-spectral image comprised of single images of different probed resonances is acquired. These images allow to identify the spatial distribution of different constituents with their characteristic spectral signatures in the sample [19]. The drawback of these schemes is the need for the stable and reproducible step-by-step frequency tuning of one of the pulses, which slows down the recording of images at different probed resonances.

Admittedly, the narrow-bandwidth approaches SRS and CARS matured in the last years in terms of the acquisition time per image, because they do not rely on slow spectrometers with a read out time in the order of milliseconds per pixel, but on fast photodiodes combined with lock-in techniques with an

acquisition time in the order of microseconds per pixel. However, together with the required frequency tuning of the laser and the subsequent recording of images at different narrow spectral bands, the acquisition time of a full broad-band hyperspectral data-set increases dramatically, proportional to the number of recorded spectral points. This required wavelength scanning reduces the advantage regarding the acquisition speed, compared to the alternative broad-bandwidth schemes. These schemes come into play, when the full Raman response is desired, for example, if the Raman spectrum of both, the fingerprint region as well as the C-H stretch region is of interest in microscopic investigations. Alternatively, so called hyperspectral images [139] can be acquired, including the full spectroscopic information at every pixel of the image. If a continuous-wave laser is incident to the sample, it induces spontaneous Raman scattering (Sec. 3.1), which shows a much lower signal level than coherent methods [10]. To apply this scheme to imaging, i. e., to restrict the capturing of the generated signal to a small volume in the focal region, the detection needs to be performed confocally [140], which additionally lowers the signal yield. This results in the necessity of a high integration time in the order of seconds per pixel. Bypassing this drawback, Plötz et al. [23] demonstrated hyperspectral imaging by applying FSRS [20] (Sec. 3.3) to microscopy, which was called femtosecond stimulated Raman microscopy (FSRM) and acquired hyperspectral data-sets in a coherent manner.

However, there are limitations in the sensitivity of the broad-bandwidth approach in FSRM, because a small signal (Raman gain or loss) is measured on a huge background. The sensitivity can be considerably increased by adding particular polarization optics like waveplates and polarizers to the FSRS-setup, as was presented in Sec. 4.2. In the resulting in-line interferometric femtosecond stimulated Raman scattering (II-FSRS), the background, namely the probe pulse spectrum, is reduced by the means of an in-line interferometer, before it is measured by the spectrometer. In this way, the dynamic range of the detector is exploited more efficiently, because the signal-to-background ratio is increased. Additionally, one may choose to set the polarization optics to get access to the spectral phase information of the resonances, or to restrict the acquired spectra to contain amplitude information only. In the latter case, the spectra exhibit traditional spontaneous Raman lineshapes and can easily be interpreted. As will be presented later, the live-observation of the sample with a standard transmission microscope allows for a quick pre-identification of an image section with the application of a broad-bandwidth pulse, because the full Raman spectrum is extracted from the focal volume in one shot.

In Sec. 4.3.1 the implementation of the II-FSRS scheme in amplitude measuring mode into a microscopy setup to record hyperspectral images is presented. It allows the acquisition of three-dimensional raster-scanned hyperspectral data-sets, which is shown for a sample of PMMA beads and a lipid droplet

in water as a demonstration in Sec. 4.3.2. A subsequent application of a principle component analysis displays the chemical selectivity of the method.

4.3.1 Experimental Microspectroscopy Setup

The schematic experimental setup of the II-FSRS microscope is shown in Fig. 31. The pump and probe pulses were derived, as before, from the laser system presented in Chap. 2. The pump pulse was a spectrally filtered pulse, extracted directly from the MOPA with a pulse energy of up to 100 nJ, a central wavelength of 1032 nm and a spectral bandwidth of 11 nm, corresponding to 103 cm^{-1}. The latter determined the spectral resolution for the presented measurements. An acousto-optic modulator (AOM) allows a fast switching of the pump pulse to acquire probe spectra with the pump turned on and off at each position in the sample. With no pump pulse present, the measurement of the probe pulse spectrum serves as a reference, so that the actual SRS induced changes on the probe pulse spectrum with the pump pulse present, can be easily extracted by calculating the difference of the two measurements. A neutral density filter (ND) is used to regulate the pump power and a linear polarization state is ensured by a polarizer (Pol2). The half-wave plate (HWP) rotates the pump polarization to the desired angle according to the favored mode of operation of the II-FSRS scheme (see Sec. 4.2). For the following proof-of-principle work, we do not investigate the phase-sensitive measurement capabilities of II-FSRS and focus on the pure Raman loss signatures, i. e., the measurement of the imaginary part of the nonlinear susceptibility $\chi^{(3)}$.

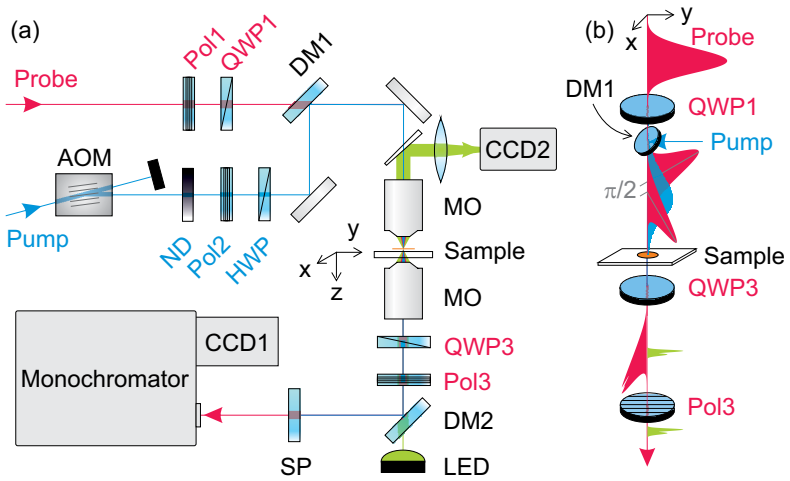

Figure 31: (a) Schematic experimental setup. ND: neutral density filter, Pol#: polarizer, QWP#: quarter-wave plate, HWP: half-wave plate, DM#: dichroic mirror, MO: microscope objective, CCD#: camera, SP: short-pass filter. (b) Schematic sketch of the II-FSRS scheme (for details see text).

The probe pulse again was a spectrally filtered portion of a supercontinuum (see Sec. 2.2). Essential for the II-FSRS approach was the circular polarization of the broadband probe pulse, which was generated with an achromatic quarter-wave plate (QWP1). Its fast axis was oriented at +45° so that the linear polarization after the polarizer (Pol1) was transformed into a circular state. This is also visualized in the schematic sketch in Fig. 31 (b), in which is shown how the probe pulse was split into two orthogonal polarization components with a relative phase shift of $\pi/2$. The circularly polarized probe pulse and the linearly polarized pump pulse were spatially merged with a dichroic mirror (DM1), which transmitted the probe pulse and reflected the pump pulse.

The upright inverted microscope was comprised of two apochromatic 40x microscope objectives each with a numerical aperture of 0.6. In-between these two, the sample was placed on a piezo-actuated scanning stage. For the presented measurements, the applied pump pulse contained 5 nJ of energy, corresponding to 5 mW of average power, such that the optical power of the pump beam at the focus was about 636 kW/cm^2. The transmitted light was sent through a second achromatic quarter-wave plate (QWP3) to transform the circular state of polarization of the probe pulse back into a linear state. Only polarization components orthogonal to this linear state of polarization were transmitted through polarizer Pol3. The residual pump pulse was blocked by a short-pass filter (SP) with a cut-off wavelength of 1000 nm. Finally, the probe beam was focused with a cylindrical lens onto the entrance slit of an imaging monochromator (Acton SP2500I from Princeton Instruments), wherein the spatially dispersed light was detected with a CCD-array (CCD1, Pixis 100 from Princeton Instruments).

All mentioned optics, especially the imaging microscope objectives, induced a temporal chirp onto the broad-bandwidth probe pulse due to chromatic dispersion. This chirp reduced the effective temporal overlap between the pump pulse and the spectral components of the probe pulse and thus limited the covered range of the measurement to an estimated 1000 cm^{-1}.

In order to image the sample with a widefield microscope simultaneously to the II-FSRS measurement, the light of a green LED was sent through the microscope from below. A dichroic mirror (DM2) was used to merge the green LED light into the beampath of the pump and probe pulse. Above the microscope a wedged glass substrate reflected a small portion of the transmitted green LED light through a lens onto a CCD camera (CCD2). The DM2 showed strong wavelength-dependent polarization changing properties for the reflection, which were undesired in this polarization-sensitive in-line interferometer. The use of such elements was feasible only outside the interferometer, meaning after polarizer Pol3. The wedged glass substrate, the microscope objectives and the sample itself did not show any noticeable alteration in the circularity of the probe pulse polarization. The dominant contribution and thus the limiting factor for the background suppression in the presented setup was the residual

wavelength-dependent retardation error of the achromatic quarter-wave plates as it was observed already in Sec. 4.2.

4.3.2 Experimental Results

The simultaneous monitoring of the transmission image of the green light from the LED allowed a live view onto the focal position within the current image section, where the II-FSRS spectrum was taken. As a demonstration, a sample of PMMA beads together with canola oil (lipid) in water was placed on a glass slide. The beads had a diameter of 26 µm and were clearly visible in the widefield image shown in Fig. 32 (a). A drop of canola oil adhered to the two shown beads and formed a bubble-like shape. A home-written LabView software allowed for the acquisition of the II-FSRS spectra, while simultaneously observing the transmission image in real-time. This live monitoring feature allowed to locate interesting spots within the sample and a fast pre-identification of the different constituents.

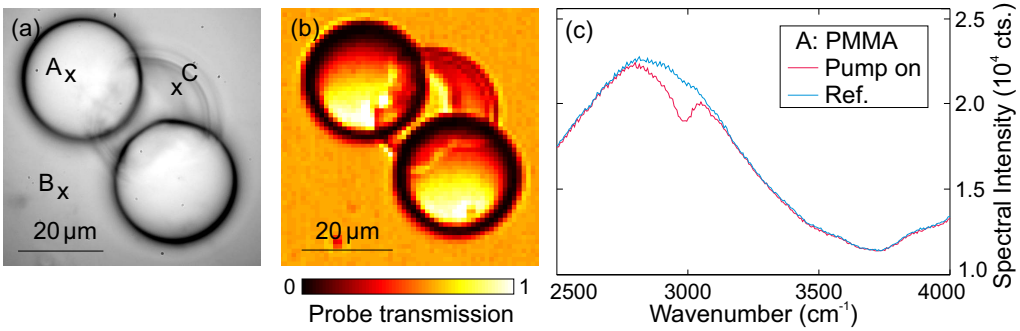

Figure 32: (a) Widefield image of PMMA beads (Position A) with canola oil (Position C) in water (Position B). (b) Integrated transmission of the probe pulse. (c) Transmitted probe pulse spectrum of a PMMA-bead (Position A in the sample) in absence (blue) and presence (red) of the pump pulse.

To demonstrate the imaging capabilities of the II-FSRS scheme, the sample was raster-scanned with the microscopy setup with a step size of 1 µm in x- and y-direction over a range of $60 \times 60\,\mu m^2$. At every point the transmitted probe pulse spectrum was recorded, one time as a reference and additionally with the pump pulse turned on, as described in Sec. 4.3.1. The CCD1 was set to an integration time of 10 ms, whereby almost the full dynamic range of the detector was exploited from the interferometrically reduced probe pulse spectrum. While the stage was held still, the transmission was rather stable, whereas it showed strong variations while the sample was moving. This was especially the case at the interfaces between the different constituents, because here, the transmitted probe pulse intensity strongly depended on the current position and the two subsequent probe pulse spectra (reference and with pump on) were measured at two different positions. The acquisition of two spectra and

the movement of the scanning stage to the next position together with a settling time took about 200 ms, so the recording of the presented hyperspectral data took about 12 minutes. The integrated transmission of the probe pulse recorded with the spectrometer is shown in Fig. 32 (b) in false colors. It matches the LED transmission image from Fig. 32 (a) very well, except being more coarse-grained due to the coarse raster scanning. The spatial resolution in Fig. 32 (b) is also lower, because firstly, the wavelength of the probe pulse is lower than the light from the green LED and secondly, the incident probe beam is not using the full aperture of the MO and thus reducing the effective NA. The reference probe pulse spectrum with the pump pulse turned off (AOM off) at the marked position "A" in Fig. 32 (a) is shown in Fig. 32 (c) as the blue line. With the pump pulse turned on, a clearly resolved dip occured at a wavenumber of about 2980 cm^{-1}.

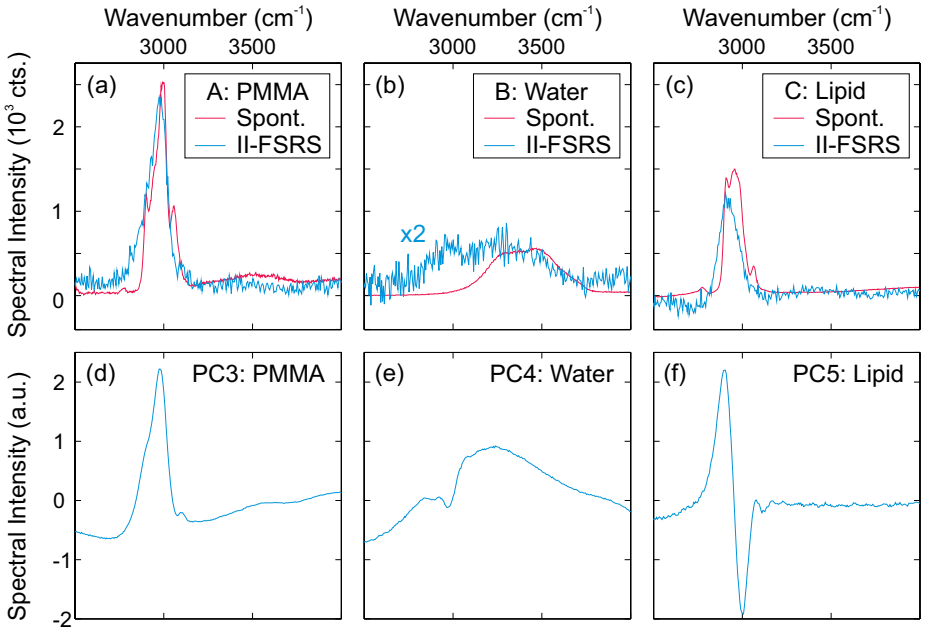

Figure 33: (a–c) Difference II-FSRS spectra (blue) and independently measured spontaneous Raman spectra (red) for different positions in the sample of PMMA beads with canola oil in water, representing PMMA (a, Position A), water (b, scaled with a factor of two for a better visibility, Position B) and the lipid droplet (c, Position C). (d–f) Relevant principal components (PC3–PC5) of the whole raw data-set.

Fig. 33 (a) shows the II-FSRS difference spectrum, calculated from the spectra shown in Fig. 32 (c) taken at position "A" as a blue curve. With a signal-to-noise ratio of about 45:1, the signal was well above the noise floor, because of the increased sensitivity of the II-FSRS scheme. In the same way, loss spectra at the positions "B" (Fig. 33 (b), blue line) and "C" (Fig. 33 (c), blue line) were calculated from the data-set and matched the Raman spectrum of water and canola oil, respectively. The spectral intensity of the broad Raman resonance of water

was rather low and centered at about 3300 cm^{-1}. For a better visibility, it was mutiplied by a factor of two. The Raman signature of the lipid droplet showed up at a lower central wavenumber than the PMMA spectum at about 2927 cm^{-1}. Together with these II-FSRS spectra, independently measured spontaneous Raman spectra are shown in Figs. 33 (a-c) in red. Although the spectral resolution was lower in the II-FSRS measurement, because of the aforementioned pulse properties, the correct position of the individual peaks and the general shape is displayed. The additional peak in the II-FSRS spectrum of water (Fig. 33 (b), blue line) at about 2930 cm^{-1} seems to result from a contamination in the sample with the three ingredients, because it is not visible in the spontaneous Raman spectrum (Fig. 33 (b), red line) of pure water.

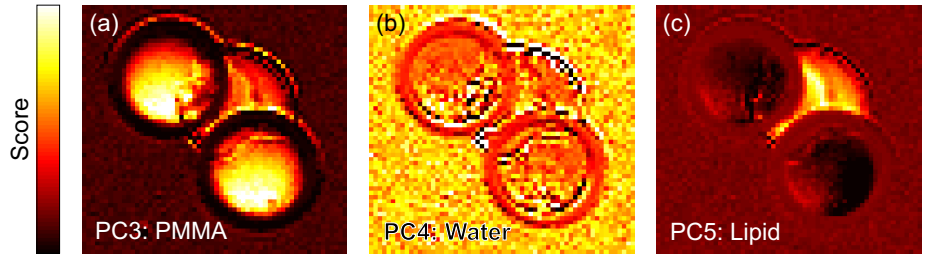

Figure 34: (a–c) Score distribution of PC3–PC5 of the PMMA beads with canola oil in water (details see text).

To interpret the hyperspectral image in more detail, a principal component analysis (PCA [141, 10, 142]) was performed with the full data-set in the presented spectral region of 2500 to 4000 cm^{-1} without any post-processing of the raw data. The PCA was selected among other analysis techniques, because it enables a straightforward evaluation of the hyperspectral data-set, without any knowledge or assumption about the sample and yielded results, which were easy to interpret, for the sample used in this work. While the first two principal components (PC) represented offsets generated by fluctuations in the transmission, the following three PCs (PC3–PC5) could be clearly identified as characteristic signatures of the three different substances in the sample and are shown in Fig. 33 (d–f). The PC3 and PC4 nicely reproduced the Raman spectra of PMMA and water, respectively. PC5 showed a maximum at the central position of the spectral feature of the lipid and a minimum at the PMMA peak, which was a result of the overlapping spectral peaks of the lipid and PMMA. The reduction of the dimensionality of the hyperspectral image to the three significant PCs, resulted in the pictures in Fig. 34 (a–c). Here, the score of the individual PCs are depicted for every pixel in false colors. The score of PC3 in Fig. 34 (a) is clearly highest within the two round beads, but it is also visible within the lipid droplet, because the spectral features of PMMA and of the lipid are overlapping (see Figs. 33 (a) and (c)). The surrounding water is rendered dark. The PC4 score distribution in Fig. 34 (b) is rather noisy, because of the low water signal (compare to Fig. 33 (b)), but still the beads as well as the lipid region

show a lower PC4 content. In Fig. 34 (c), the score of PC5 of the lipid shows a striking contrast to the beads and the water.

As a next step, the identical section of the sample was raster-scanned in all three spatial dimensions. The stepsize in every direction was set to 2 µm over a volume of 54 x 54 x 26 µm^3 resulting in an acquisition time of about 32 minutes. The same PCA procedure as before was applied to the raw data-set. The PC3 again showed the dominant PMMA Raman peak. Compared to the two-dimensional measurement in Fig. 34, here, the relative amount of the actual Raman signatures were lower than before, because the contributing constituents in the sample (beads and lipid) took less room relative to the scanned volume. Additionally, there were more structured or periodically modulated spectra present, mainly because of interference effects at the interfaces within the sample. These contributions were covered by PC4–PC7, followed by PC8 and PC9, which were identified as the Raman signature of water and the lipid, respectively. The different scores of the relevant PCs were rendered as isosurfaces in Fig. 35. The colors red, blue and green represent PC3 (PMMA), PC8 (water) and PC9 (lipid), respectively, while the level of the score sets the opacity of the isosurfaces. Again, no smoothing or interpolation has been applied for the data visualization. The "red" beads exhibit a spherical shape and the "blue" water fills the whole surrounding volume. In this three-dimensional rendering the actual shape of the "green" lipid droplet becomes apparent. It adhered flat to the bottom cover slip and stuck to the two beads, filling the gap in-between them. Due to noise in general and the overlapping spectral features of the lipid and the beads, there are some distortions from the ideal shapes, but the separate components are clearly distinguishable from one another.

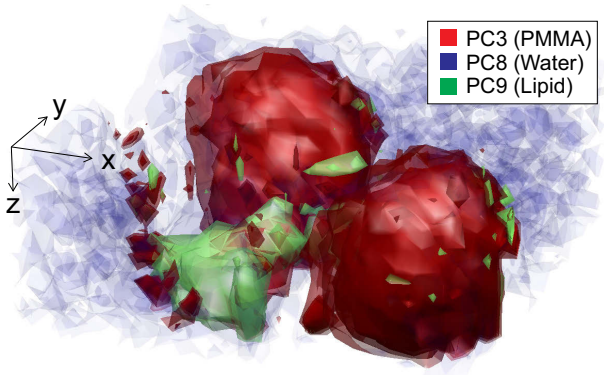

Figure 35: Three-dimensional isosurface rendering of the score of the PCs of the hyperspectral data-set of PMMA beads with canola oil in water of a volume of 54 x 54 x 26 µm^3 (for details see text).

As a second demonstration, a sample of PMMA and polystyrene (PS) beads was prepared and analyzed, as just presented. Both beads had a diameter of about 26 µm and consequently were not distinguishable from one another in a transmission image. But since the Raman resonance of PMMA (at 2927 cm^{-1})

and PS (measured to be located at 3053 cm^{-1}) are sufficiently distinguishable from one another, they are clearly discriminated by the PCA, resulting in the three-dimensional rendering shown in Fig. 36. Here also, the beads are rendered as spherical objects and are fully surrounded by water.

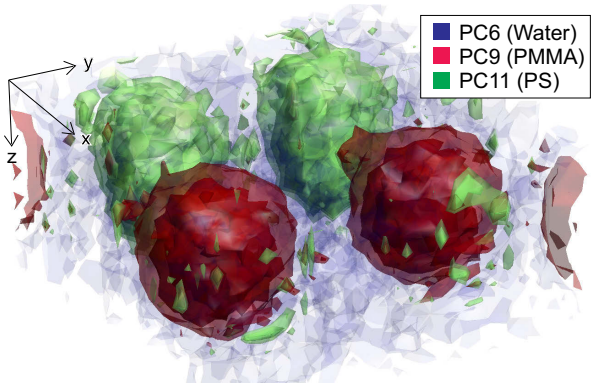

Figure 36: Three-dimensional isosurface rendering of the score of the PCs of a hyperspectral data-set of PMMA and PS beads in water of a volume of 56 x 60 x 28 μm^3 (for details see text).

4.4 CURRENT LIMITATIONS AND FURTHER IMPROVEMENTS

The presented experiments in the foregoing chapter demonstrated the high potential of the interferometric approach to acquire Raman spectra. Nevertheless, there are several opportunities of improvements in this proof-of-principle work of iFSRS, II-FSRS and the hyperspectral imaging. These improvements are addressed and discussed individually in the following.

The current *spatial resolution* is limited due to the relatively low numerical aperture (0.6) microscope objectives, which can easily be replaced by better optics with a higher numerical aperture. The rather low *spectral resolution* of about 100 cm^{-1} is determined by the spectral bandwidth of the pump pulse, so that narrow-bandwidth picosecond pump pulses will be used in future experiments to improve the spectral resolution by one order of magnitude. The application of longer pump pulses would indeed reduce the signal yield, because the efficiency of SRS scales with the peak power of the applied pump and probe pulses. However, a simultaneous compression of the actually applied temporally dispersed probe pulse would counteract the loss of efficiency. At the same time, the covered *spectral range* of the scheme would increase up to the full bandwidth of the broadband probe pulse due to the increased temporal overlap between the pump and probe pulses.

In the current II-FSRS setup, the birefringence of the components in the setup or the samples itself only showed a negligible effect to the signal-to-background ratio. The retardation error of the quarter-wave plates for the in-line interferom-

eter was the main limitation, so more performant optics, like Fresnel rhomb retarders, will considerably raise the *sensitivity* of II-FSRS. Increasing the signal-to-background ratio will also have a beneficial effect on the signal-to-noise ratio. The dominant contribution to noise is introduced by the detector of the spectrometer. With a further reduced background, the dynamic range of the detector could be exploited to a higher extent with the actual signal by being able to increase the applied probe pulse power or the integration time of the detector. As a result, the signal level would be elevated, while the detector noise would stay constant. The additionally induced temporal pulse stretching due to the material dispersion of the Fresnel rhomb retarders could be compensated for with the aforementioned compressor. By reducing the retardation error of the retarders, also the potential influence of the birefringence of the sample and the other components will have to be reconsidered. If a strong birefringence would be present, the amount of the interferometric reduction would be decreased, but even in the worst case of no reduction, the background would be limited to the level of standard FSRS. A realistic assessment of a biological sample with a birefringence of $\Delta n = 0.001$ [143] and a thickness of 4 µm would result in an influence comparable to the retardation error of the actually used achromatic waveplates.

With post-processing and/or averaging of the raw spectral data, it should be possible to improve the *general noise characteristics*. The *acquisition time* of the II-FSRS hyperspectral data is currently dominated by the settling time of the scanning stage (~ 100 ms), which could be drastically reduced by the implementation of galvanometric scanner mirrors. The data acquisition at one spatial position was mainly limited by the software, related to the implementation of an easy but inefficient way to save the spectra and a slow hardware communication, which is limiting the read-out time of the CCD. Resolving these data acquisition issues would further enhance the speed of the hyperspectral measurement at least by one order of magnitude.

4.5 SUMMARY AND CONCLUSION

In summary, this section showed interferometric approaches for a background reduction of FSRS measurements. The presented iFSRS scheme using an unbalanced Sagnac interferometer demonstrated a signal-to-background ratio improvement by a factor of 25. This enabled acquisition of clear iFSRS spectra with only a CCD-array spectrometer, which potentially offered very fast acquisition times, limited only by the read-out time of the spectrometer. In addition, it was shown that the interferometric measurement does not reduce the Raman signal to a simple loss signature in the spectrum, but revealed the phase shift, gathered within the nonlinear interaction, as a dispersive lineshape. The spectral (phase) shape of this line could be recreated based on the Lorentzian model,

such that access was gained not only to the amplitude, but also to the phase of the resonant $\chi^{(3)}$.

Additionally, II-FSRS, a novel interferometric scheme for the measurement of Raman scattering spectra was introduced and compared to the competing broad-bandwidth CRS schemes FSRS and FRIKES. II-FSRS exploited the advantages of an unbalanced in-line interferometer, where two probe pulse copies were distinguished by their polarization. It was shown that by only varying the polarization of the pump pulses, both, Raman loss and gain spectra as well as dispersive lineshapes could be achieved. This corresponded to directly measuring the intensity spectra, but also granted access to the phase of the coherent Raman signal, resulting in a characterization of the full complex response of the sample. Using a vibrational resonance of acetonitrile, very clear and distinct spectra were measured with a high signal-to-noise ratio of 156:1.

In contrast to iFSRS, the II-FSRS setup was simpler and rugged and could be realized by only adding two QWPs to the FSRS or FRIKES setup. This enabled the direct application of II-FSRS to microscopy, where it lead to an increased S/N-ratio compared to FSRS or to a faster acquisition time compared to FRIKES. Additionally the spectral resolution could be improved by utilizing the phase information.

Consequently, the hyperspectral imaging capabilities of the II-FSRS scheme were presented. The high sensitivity for the detection of stimulated Raman loss spectra allowed for an acquisition of hyperspectral data-sets in two and three dimensions with a rate of five spectra per second. The clear Raman signatures enabled the application of a principal component analysis to reduce the dimensionality of the measurement to the three test constituents of the samples: PMMA, lipid and water, or PMMA, PS, and water. A volumetric reconstruction of the sample revealed the structure and distribution of each of the different elements. This proof-of-principle demonstration clearly showed a high applicability of the II-FSRS scheme.

Apart from the improvements listed in Sec. 4.4, the continuation of this work will expand the potential of the interferometric measurement of nonlinear interactions into two directions: one direction will concentrate on the measurement of broader and more complex spectra with overlapping resonances and on the consequential application of the hyperspectral imaging capabilities to complex problems in life-sciences, e.g., imaging lipid distributions in cellular membranes [144]. Here we will investigate the potential to extract the amplitude and especially the phase information in order to analyze mixtures of unknown compounds with a high accuracy.

In another direction, the interferometric approach can be applied to narrowband SRS loss spectroscopy. By reducing the bandwidth, we should be able to improve the background reduction and thus the S/B-ratio in a narrow spectral

band. In this way, the method will be combined with lock-in techniques to push the threshold of detectable SRS to even fainter signals.

5 SUMMARY OF THE THESIS

This thesis was about the development of the combination of a highly adapted light source and a specialized spectroscopic scheme to generate a molecular specific contrast for the application to microscopic imaging. The focus of the light source was on a reasonable balance between the peak and average power of the pulses, in order to ensure an efficient nonlinear response and simultaneously a minimized thermal impact within light-matter interaction.

The master oscillator and power amplifier system (MOPA, Sec. 2.1) also met the requirements of various other nonlinear optical experiments, like optical nonlinear transverse mode conversion in few-mode fibers [103]. The fundamental fiber-based all-normal dispersion laser oscillator (Sec. 2.1.1) maintained a stable pulsed operation over weeks, while supporting a pulse duration of less than 300 fs. The connected chirped pulse amplification setup (Sec. 2.1.2) boosted the pulse power to over 4 µJ at a repetition frequency of 1 MHz, while keeping the influence of disturbing nonlinear effects to a minimum. The choice of the repetition frequency dictated the applicable pulse energy, which was limited either by a thermal or a nonlinear damage threshold, whereby a repetition frequency of 1 MHz was enabling a promising balance. The residual nonlinear phase distortions within the amplification processes were compensated for by a pulse shaper based on a liquid crystal spatial light modulator (Sec. 2.1.3). The automated pulse optimization algorithm allowed for a reliable day-to-day use of the system.

A direct application of the MOPA pulses was the generation of a highly stable and coherent supercontinuum in bulk media. These broad-bandwidth pulses were an essential element for pump-probe experiments, i. e. broad-bandwidth coherent Raman scattering, or to seed optical amplifiers (Sec. 2.2). The parameters of the MOPA pulse, namely the duration and pulse energy, were sufficient to induce self-focusing inside the crystal resulting in a filament, wherein the highly increased intensity enabled the exploitation of nonlinear effects, like self-phase modulation and plasma defocusing (Sec. 2.2.1). Optimal conditions were acquired in an experimental survey (Sec. 2.2.2), which revealed a strong dependence of the performance of, among others, the choice of the nonlinear medium, the incident pulse energy and the focusing conditions. The consequential spectral broadening was highly coherent and resulted in highly stable supercontinua. With the acquired optimal conditions, the emerging supercontinuum exhibited root mean square pulse-to-pulse fluctuations in the order of 1 %, and an energy content of a few tens of nanojoule, covering a spectral region of 600 to more than 1600 nm.

Besides the utilization of the supercontinum in broad-bandwidth coherent Raman scattering (CRS) experiments, the supercontinuum is also well suited to seed an optical parametric amplifier, which is directly pumped by a pulse of the MOPA. The implementation of the supercontinuum and the MOPA pulse to narrow-bandwidth optical parametric amplifiers (OPA) was presented in three different nonlinear crystals in Sec. 2.3. The periodically poled lithium niobate crystal (PPLN, Sec. 2.3.1) showed a good performance for the generation of tunable signal pulses with a central wavelength in the region of 1480 nm to above 1600 nm. The superior transmission of lithium indium selenide (LISE, Sec. 2.3.3), reaching up to a wavelength of 12000 nm, allowed the generation of signal pulses close to the pump wavelength and consequently, the idler pulses theoretically possessed a central wavelength of 10700 nm and thus were not directly absorbed in the crystal. In combination with a MOPA pulse, the signal pulse of the LISE-based OPA will enable the probing of Raman resonances with narrow-bandwidth CRS schemes in the fingerprint region, while the wavelength of the signal pulses of the PPLN-based OPA will match the C-H stretch region. Along with further improvements of the OPAs and the MOPA system, as discussed in Sec. 2.4, the application of the generated pulses to narrow-bandwidth CRS and other nonlinear experiments is part of future efforts.

The performed broad-bandwidth CRS experiments in Chap. 3, which directly applied the supercontinuum pulses, showed a high potential to be applied in hyperspectral imaging. Both, femtosecond Raman-induced Kerr-effect spectroscopy (FRIKES, Sec. 3.2) and femtosecond stimulated Raman scattering (FSRS, Sec. 3.3) allowed the one-step acquisition of broad Raman scattering spectra. But also individual disadvantages could be seen: the Raman-induced Kerr-effect within FRIKES shows a lower efficiency than stimulated Raman scattering in FSRS, but in the latter the signal is highly exceeded by a background (Sec. 3.4).

In contrast, the developed novel interferometric approaches to acquire FSRS spectra, as presented in Chap. 4, yielded a broad-bandwidth Raman response on a greatly reduced background and thus compensated the disadvantage of FSRS, concerning the disturbing background. Furthermore, the measured signal not only included the amplitude information of the involved Raman resonance, but also rendered the phase information, because an interferometer is inherently phase-dependent. The resulting dispersive lineshapes were obtained within interferometric FSRS (iFSRS, Sec. 4.1 and [119]) employing a Sagnac interferometer, which is intrinsically stable, because both interfering beams share the same path, traveling in reverse directions. By ensuring a pump pulse to probe pulse overlap only in one direction, the interferometer was unbalanced, resulting in an output, containing ideally only the nonlinear contribution of the pump-probe interaction. Apart from a residual background emerging from experimental imperfections, the iFSRS spectrum exhibited the Raman scattering

signal as a dispersive line with an improved signal-to-background ratio by a factor of 16 compared to FSRS. This interferometric approach however, is limited in terms of the application towards imaging, because the Sagnac interferometer performance is prone to spatial distortions induced, e. g. by a microscopic sample.

These restrictions of iFSRS were revoked in the further developed in-line interferometric FSRS (II-FSRS, [145]), which applied an in-line interferometer (Sec. 4.2) and yielded comparable results to iFSRS. The concept of II-FSRS is the separation of two probe pulse copies through different polarizations and a consequential pump-probe interaction depending on the pump pulse polarization. After rearranging the polarization of the two probe pulse components and their consequential interference, the Raman response was exposed in the resulting spectrum, depending on the pump pulse polarization. Either, the spectrum resembled a common Raman scattering intensity spectrum, or dispersive lineshapes (comparable to iFSRS spectra) were acquired. In both cases, the background was reduced by more than 25 dB and thus the signal-to-noise ratio was increased considerably. Additionally, the enlarged content of information within the dispersive lines actually raised the spectral resolution, exhibiting a narrower linewidth. On the other hand, the intensity spectra are easier to interpret, because they resemble the Raman scattering intensity spectrum.

The implementation of II-FSRS into a microscopic setup was shown in Sec. 4.3 and [146], where the observation of the sample in a standard transmission arrangement allowed an easy recognition of interesting spatial regions within the sample, while the continuous acquisition of Raman spectra enabled a live preidentification of the substance within the focus. Hyperspectral data-sets were acquired from the microscopic samples by raster-scanning the sample with a fixed focus position and were analyzed by applying a principle component analysis, displaying the molecular specificity of II-FSRS.

In conclusion, in this thesis a versatile light source in combination with easy to handle, yet fertile interferometric approaches to broad-bandwidth coherent Raman scattering spectroscopic schemes were developed. The high applicability of this comprehensive system to microspectroscopy is very promising for future research and with the suggested improvements (Sec. 4.4) especially interesting for investigations in the life sciences.

ACKNOWLEDGEMENTS

This work would not have been possible without the support of the following people, whom I would like to express my gratitude.

Firstly, I would like to thank Prof. Dr. Carsten Fallnich, who gave me the opportunity to work in his group – Optical Technologies – as a PhD student. His inspiring, but at the same time challenging, supervision of the activities, allowed this thesis and the connected publications to be filled with high quality scientific content. I would also like to express my gratitude towards Prof. Dr. Klaus Boller, who agreed to be the second adviser for this thesis.

I also have to thank Maximilian Bradler from the LMU München for his support concerning the supercontinuum generation with laser host materials, Andreas Gieselmann, who set up the applied spontaneous Raman spectrometer in the frame of his Diploma thesis and the Fraunhofer-Institute IOF Jena for providing the fused fiber end cap, used in the high power amplifier.

I further acknowledge the financial support from the DAAD and CeNoS for enabling various conference contributions and the funding by the flexible funding project FF-2013-09 within the frame of the cluster of excellence 'Cells in Motion' (EXC 1003). I gratefully acknowledge scientific equipment support of the state North Rhine-Westphalia and the Deutsche Forschungsgemeinschaft (DFG) within the DFG's Mayor Research Instrumentation Program by project INST 211/592-1 FUGG.

The whole group Optical Technologies provided a relaxed and exhilarated environment for the years that I have worked here so far, for which I am very grateful. Also special thanks to Dr. Petra Groß for the very helpful start of my work and the continuous support.

It was a great pleasure to supervise the Diploma thesis of Gerrit Hölscher, the Masters thesis (partially) of Martin Höhl and Benedikt Schürmann-Schlieker and the Bachelor theses of Markus Fischedick, Christian Egelkamp and Felix Neumann. I have learned a lot and also included some of your good results into this thesis.

There are some extraordinary friends along the long way, whom I would particularly like to thank: Dr. Michael Kues for the long and joyful companionship through all the semesters, Max Brinkmann for being a relaxed roommate, Dr. Sebastian Knitter for sharing his uncommon thoughts, Tim Hellwig for easing obligations and my dearest friends from home and everyone else for attending prolonged nights in Münster and wherever else.

At long last, my deepest gratitude lies within my family. I would like to thank my parents (Gabi and Rainer) for your complete and unexceptional support. Thank you Inga, my love and wife, for your unconditional love and devotion and for completing my life with our daughter Laila.

BIBLIOGRAPHY

[1] E. Abbe, "Beiträge zur Theorie des Mikroskops und der mikroskopischen Wahrnehmung", Arch. Mikroskop. Anat. **9**, 413–420 (1873).

[2] J. R. Loofbourow, "Microspectroscopy", J. Opt. Soc. Am. **40**, 317–325 (1950).

[3] E. R. Blout, G. R. Bird, and D. S. Grey, "Infra-Red Microspectroscopy", J. Opt. Soc. Am. **40**, 304–313 (1950).

[4] D. J. David, "The application of atomic absorption spectra to chemical analysis. A review", Analyst **85**, 779–791 (1960).

[5] H. Fujiwara, *Spectroscopic Ellipsometry: Principles and Applications*, (John Wiley and Sons, 2007).

[6] C. Parker and W. Rees, "Fluorescence spectrometry. A review", Analyst **87**, 83–111 (1962).

[7] C. V. Raman, "A new radiation", Indian J. Phys. **2**, 387–398 (1928).

[8] N. B. Colthup, L. H. Daly, and S. E. Wiberley, *Introduction to Infrared and Raman Spectroscopy*, (New York, 1975), third edition.

[9] G. J. Thomas Jr., "Raman spectroscopy of protein and nucleic acid assemblies", Annu. Rev. Bioph. Biom. **28**, 1–27 (1999).

[10] R. Salzer and H. W. Siesler, editors, *Infrared and Raman Spectroscopic Imaging*, (John Wiley and Sons, 2009).

[11] G. Grynberg and B. Cagnac, "Doppler-free multiphotonic spectroscopy", Rep. Prog. Phys. **40**, 791–841 (1977).

[12] F. Biraben, B. Cagnac, and G. Grynberg, "Experimental evidence of two-photon transition without Doppler broadening", Phys. Rev. Lett. **32**, 643–645 (1974).

[13] T. Hänsch, K. Harvey, G. Meisel, and A. Schawlow, "Two-photon spectroscopy of Na 3s-4d without Doppler broadening using a cw dye laser", Opt. Commun. **11**, 50–53 (1974).

[14] M. D. Levenson and N. Bloembergen, "Dispersion of the nonlinear optical susceptibility tensor in centrosymmetric media", Phys. Rev. B **10**, 4447–4463 (1974).

[15] X. Nan, J.-X. Cheng, and X. S. Xie, "Vibrational imaging of lipid droplets in live fibroblast cells with coherent anti-Stokes Raman scattering microscopy", J. Lipid Res. **44**, 2202–2208 (2003).

[16] C. L. Evans, E. O. Potma, M. Puoris'haag, D. Côté, C. P. Lin, and X. S. Xie, "Chemical imaging of tissue in vivo with video-rate coherent anti-Stokes Raman scattering microscopy", Proc. Natl. Acad. Sci. U.S.A. **102**, 16807–16812 (2005).

[17] C. W. Freudiger, W. Min, B. G. Saar, S. Lu, G. R. Holtom, C. He, J. C. Tsai, J. X. Kang, and X. S. Xie, "Label-free biomedical imaging with high sensitivity by stimulated Raman scattering microscopy", Science **322**, 1857–1861 (2008).

[18] Y. Ozeki, Y. Kitagawa, K. Sumimura, N. Nishizawa, W. Umemura, S. Kajiyama, K. Fukui, and K. Itoh, "Stimulated Raman scattering microscope with shot noise limited sensitivity using subharmonically synchronized laser pulses", Opt. Express **18**, 13708–13719 (2010).

[19] W. Min, "Label-free optical imaging of nonfluorescent molecules by stimulated radiation", Curr. Opin. Chem. Biol. **15**, 831–837 (2011).

[20] D. W. McCamant, P. Kukura, and R. A. Mathies, "Femtosecond broadband stimulated Raman: a new approach for high-performance vibrational spectroscopy", Appl. Spectrosc. **57**, 1317–1323 (2003).

[21] D. Heiman, R. W. Hellwarth, M. D. Levenson, and M. Graham, "Raman-Induced Kerr Effect", Phys. Rev. Lett. **36**, 189–192 (1976).

[22] S. Shim and R. A. Mathies, "Femtosecond Raman-induced Kerr effect spectroscopy", J. Raman Spectrosc. **39**, 1526–1530 (2008).

[23] E. Ploetz, S. Laimgruber, S. Berner, W. Zinth, and P. Gilch, "Femtosecond stimulated Raman microscopy", Appl. Phys. B **87**, 389–393 (2007).

[24] B.-M. Kim, M. D. Feit, A. M. Rubenchik, E. J. Joslin, J. Eichler, P. C. Stoller, and L. B. Da Silva, "Effects of high repetition rate and beam size on hard tissue damage due to subpicosecond laser pulses", Appl. Phys. Lett. **76**, 4001–4003 (2000).

[25] T. Shimada, W. Watanabe, S. Matsunaga, T. Higashi, H. Ishii, and K. Fukui, "Intracellular disruption of mitochondria in a living HeLa cell with a 76-MHz femtosecond laser oscillator", Opt. Express **13**, 9869–9880 (2005).

[26] D. E. Spence, P. N. Kean, and W. Sibbett, "60-fsec pulse generation from a self-mode-locked Ti:sapphire laser", Opt. Lett. **16**, 42–44 (1991).

[27] M. H. Niemz, *Laser-Tissue Interactions*, (Springer, 1996).

[28] J. E. Murray and W. H. Lowdermilk, "Nd:YAG regenerative amplifier", J. Appl. Phys. **51**, 3548–3555 (1980).

[29] W. H. Lowdermilk and J. E. Murray, "The multipass amplifier: Theory and numerical analysis", J. Appl. Phys. **51**, 2436–2444 (1980).

[30] G. Vaillancourt, "Operation of a 1-kHz pulse-pumped Ti:sapphire regenerative amplifier", Opt. Lett. **15**, 317–319 (1990).

[31] P. Nandakumar, A. Kovalev, and A. Volkmer, "Vibrational imaging based on stimulated Raman scattering microscopy", New J. Phys. **11**, 033026 1–9 (2009).

[32] A. Zumbusch, G. R. Holtom, and X. S. Xie, "Three-Dimensional Vibrational Imaging by Coherent Anti-Stokes Raman Scattering", Phys. Rev. Lett. **82**, 4142–4145 (1999).

[33] C. W. Freudiger, W. Min, B. G. Saar, S. Lu, and G. R. Holtom, "Label-free biomedical imaging with high sensitivity by stimulated Raman scattering microscopy", Science **322**, 1857–1861 (2008).

[34] Y. Ozeki, F. Dake, S. Kajiyama, K. Fukui, and K. Itoh, "Analysis and experimental assessment of the sensitivity of stimulated Raman scattering microscopy", Opt. Express **17**, 3651–3658 (2009).

[35] G. L. Hölscher, *Erzeugung und Verstärkung ultrakurzer Laserimpulse für nichtlineare Raman-Spektroskopie*, Diploma thesis, Westfälische Wilhelms-Universität Münster (2012).

[36] M. Fischedick, *Superkontinuumserzeugung in Laserwirtskristallen - Untersuchung zur spektralen Bandbreite und Leistungsstabilität*, Bachelor thesis, Westfälische Wilhelms-Universität Münster (2012).

[37] C. Egelkamp, *Aufbau und Charaktisierung eines optisch parametrischen Verstärkers basierend auf periodisch gepoltem Lithiumniobat*, Bachelor thesis, Westfälische Wilhelms-Universität Münster (2013).

[38] A. Chong, J. Buckley, W. Renninger, and F. Wise, "All-normal-dispersion femtosecond fiber laser", Opt. Express **14**, 660–662 (2006).

[39] R. L. Fork, O. E. Martinez, and J. P. Gordon, "Negative dispersion using pairs of prisms", Opt. Lett. **9**, 150–152 (1984).

[40] E. Treacy, "Optical pulse compression with diffraction gratings", IEEE J. Quantum Elect. **QE-5**, 454–458 (1969).

[41] R. Szipocs, K. Ferencz, C. Spielmann, and F. Krausz, "Chirped multilayer coatings for broadband dispersion control in femtosecond lasers", Opt. Lett. **19**, 201–203 (1994).

[42] J. Buckley, A. Chong, S. Zhou, W. Renninger, and F. W. Wise, "Stabilization of high-energy femtosecond ytterbium fiber lasers by use of a frequency filter", J. Opt. Soc. Am. B **24**, 1803–1806 (2007).

[43] A. Chong, W. H. Renninger, and F. W. Wise, "Properties of normal-dispersion femtosecond fiber lasers", J. Opt. Soc. Am. B **25**, 140–148 (2008).

[44] A. Chong, W. H. Renninger, and F. W. Wise, "All-normal-dispersion femtosecond fiber laser with pulse energy above 20 nJ", Opt. Lett. **32**, 2408–2410 (2007).

[45] J. W. Evans, "The Birefringent Filter", J. Opt. Soc. Am. **39**, 229–242 (1949).

[46] K. Kieu and F. W. Wise, "All-fiber normal-dispersion femtosecond laser", Opt. Express **16**, 11453–11458 (2008).

[47] R. Stolen and C. Lin, "Self-phase-modulation in silica optical fibers", Phys. Rev. A **17**, 1448–1453 (1978).

[48] G. P. Agrawal, *Nonlinear Fiber Optics*, (Academic Press, 2007), fourth edition.

[49] D. Strickland and G. Mourou, "Compression of amplified chirped optical pulses", Opt. Commun. **55**, 447–449 (1985).

[50] O. E. Martinez, "3000 Times Grating Compressor with Positive Group Velocity Dispersion: Application to Fiber Compensation in 1.3-1.6 μm Region", IEEE J. Quantum Elect. **QE-23**, 59–64 (1987).

[51] A. Monmayrant, S. Weber, and B. Chatel, "A newcomer's guide to ultrashort pulse shaping and characterization", J. Phys. B - At. Mol. Opt. Phys. **43**, 103001 1–18 (2010).

[52] A. Siegman, "Defining, measuring, and optimizing laser beam quality", Proc. SPIE **V**, 2–12 (1993).

[53] A. M. Weiner, "Femtosecond pulse shaping using spatial light modulators", Rev. Sci. Instrum. **71**, 1929–1960 (2000).

[54] D. Yelin, D. Meshulach, and Y. Silberberg, "Adaptive femtosecond pulse compression", Opt. Lett. **22**, 1793–1795 (1997).

[55] T. Baumert, T. Brixner, V. Seyfried, M. Strehle, and G. Gerber, "Femtosecond pulse shaping by an evolutionary algorithm with feedback", Appl. Phys. B **65**, 779–782 (1997).

[56] T. Brixner, A. Oehrlein, M. Strehle, and G. Gerber, "Feedback-controlled femtosecond pulse shaping", Appl. Phys. B **124**, 119–124 (2000).

[57] J. Prawiharjo, N. K. Daga, R. Geng, J. H. Price, D. C. Hanna, D. J. Richardson, and D. P. Shepherd, "High fidelity femtosecond pulses from an ultrafast fiber laser system via adaptive amplitude and phase pre-shaping", Opt. Express **16**, 15074–15089 (2008).

[58] F. He, H. S. S. Hung, J. H. V. Price, N. K. Daga, N. Naz, J. Prawiharjo, D. C. Hanna, D. P. Shepherd, D. J. Richardson, J. W. Dawson, C. W. Siders, and C. P. Barty, "High energy femtosecond fiber chirped pulse amplification system with adaptive phase control", Opt. Express **16**, 5813–5821 (2008).

[59] A. Efimov, M. D. Moores, N. M. Beach, J. L. Krause, and D. H. Reitze, "Adaptive control of pulse phase in a chirped-pulse amplifier", Opt. Lett. **23**, 1915–1917 (1998).

[60] F. G. Omenetto, B. P. Luce, and A. J. Taylor, "Genetic algorithm pulse shaping for optimum femtosecond propagation in optical fibers", J. Opt. Soc. Am. B **16**, 2005–2009 (1999).

[61] R. Eberhart and J. Kennedy, "A new optimizer using particle swarm theory", Proceedings of the Sixth International Symposium on Micro Machine and Human Science 39–43 (1995).

[62] R. V. D. Zwet, "Laser Pulse Shaping problem", Technical Report december (2009).

[63] D. Kane and R. Trebino, "Characterization of arbitrary femtosecond pulses using frequency-resolved optical gating", IEEE J. Quantum Elect. **29**, 571–579 (1993).

[64] K. W. DeLong, R. Trebino, J. Hunter, and W. E. White, "Frequency-resolved optical gating with the use of second-harmonic generation", J. Opt. Soc. Am. B **11**, 2206–2215 (1994).

[65] R. Trebino and K. DeLong, "Measuring ultrashort laser pulses in the time-frequency domain using frequency-resolved optical gating", Rev. Sci. Instrum. **68**, 3277–3295 (1997).

[66] R. Alfano and S. Shapiro, "Emission in the region 4000 to 7000 Å via four-photon coupling in glass", Phys. Rev. Lett. **24**, 584–588 (1970).

[67] P. Corkum, C. Rolland, and T. Srinivasan-Rao, "Supercontinuum generation in gases", Phys. Rev. Lett. **57**, 2268–2271 (1986).

[68] F. Shimizu, "Frequency Broadening in Liquids by a Short Light Pulse", Phys. Rev. Lett. **19**, 1097–1100 (1967).

[69] A. Brodeur and S. L. Chin, "Band-Gap Dependence of the Ultrafast White-Light Continuum", Phys. Rev. Lett. **80**, 4406–4409 (1998).

[70] P. Russell, "Photonic crystal fibers", Science **299**, 358–362 (2003).

[71] J. M. Dudley and S. Coen, "Supercontinuum generation in photonic crystal fiber", Rev. Mod. Phys. **78**, 1135–1184 (2006).

[72] A. Guandalini, P. Eckle, M. Anscombe, P. Schlup, J. Biegert, and U. Keller, "5.1 fs Pulses Generated By Filamentation and Carrier Envelope Phase Stability Analysis", J. Phys. B - At. Mol. Opt. Phys. **39**, S257–S264 (2006).

[73] M. Wittmann and A. Penzkofer, "Spectral superbroadening of femtosecond laser pulses", Opt. Commun. **126**, 308–317 (1996).

[74] A. Gaeta, "Catastrophic collapse of ultrashort pulses", Phys. Rev. Lett. **84**, 3582–3585 (2000).

[75] A. Couairon and A. Mysyrowicz, "Femtosecond filamentation in transparent media", Phys. Rep. **441**, 47–189 (2007).

[76] R. A. Ganeev, I. A. Kulagin, A. I. Ryasnyanskii, R. I. Tugushev, and T. Usmanov, "The nonlinear refractive indices and nonlinear third-order susceptibilities of quadratic crystals", Opt. Spectrosc. **94**, 561–568 (2003).

[77] Y. Furukawa, A. Yokotani, T. Sasaki, H. Yoshida, K. Yoshida, F. Nitanda, and M. Sato, "Investigation of bulk laser damage threshold of lithium niobate single crystals by Q-switched pulse laser", J. Appl. Phys. **69**, 3372–3374 (1991).

[78] J.-F. Bisson, Y. Feng, A. Shirakawa, H. Yoneda, J. Lu, H. Yagi, T. Yanagitani, and K.-I. Ueda, "Laser Damage Threshold of Ceramic YAG", Jap. J. Appl. Phys. **42**, L1025–L1027 (2003).

[79] M. Bradler, P. Baum, and E. Riedle, "Femtosecond continuum generation in bulk laser host materials with sub-μJ pump pulses", Appl. Phys. B **97**, 561–574 (2009).

[80] E. Riedle, M. Beutter, S. Lochbrunner, J. Piel, S. Schenkl, S. Spörlein, and W. Zinth, "Generation of 10 to 50 fs pulses tunable through all of the visible and the NIR", Appl. Phys. B **71**, 457–465 (2000).

[81] J. M. Klopf and P. Norris, "Probing nonequilibrium dynamics with white-light femtosecond pulses", Appl. Surf. Sci. **253**, 6305–6309 (2007).

[82] G. Cerullo and S. De Silvestri, "Ultrafast optical parametric amplifiers", Rev. Sci. Instrum. **74**, 1–18 (2003).

[83] L. Myers and W. Bosenberg, "Periodically poled lithium niobate and quasi-phase-matched optical parametric oscillators", IEEE J. Quantum Elect. **33**, 1663–1672 (1997).

[84] P. E. Powers, K. W. Aniolek, T. J. Kulp, B. a. Richman, and S. E. Bisson, "Periodically poled lithium niobate optical parametric amplifier seeded with the narrow-band filtered output of an optical parametric generator", Opt. Lett. **23**, 1886–1888 (1998).

[85] A. V. Smith, "SNLO nonlinear optics code", (2012).

[86] C. Cleff, P. Groß, C. Fallnich, H. L. Offerhaus, J. L. Herek, K. Kruse, W. P. Beeker, C. J. Lee, and K.-J. Boller, "Ground-state depletion for subdiffraction-limited spatial resolution in coherent anti-Stokes Raman scattering microscopy", Phys. Rev. A **86**, 023825 1–11 (2012).

[87] C. Cleff, P. Groß, C. Fallnich, H. Offerhaus, J. Herek, K. Kruse, W. Beeker, C. Lee, and K.-J. Boller, "Stimulated-emission pumping enabling sub-diffraction-limited spatial resolution in coherent anti-Stokes Raman scattering microscopy", Phys. Rev. A **87**, 033830 1–9 (2013).

[88] D. S. Chemla, P. J. Kupecek, D. S. Robertson, and R. C. Smith, "Silver thiogallate, a new material with potential for infrared devices", Opt. Commun. **3**, 29–31 (1971).

[89] P. Canarelli, Z. Benko, A. H. Hielscher, R. F. Curl, and F. K. Tittel, "Measurement of nonlinear coefficient and phase matching characteristics of $AgGaS_2$", IEEE J. Quantum Elect. **28**, 52–55 (1992).

[90] S. A. Andreev, I. N. Matveev, I. P. Nekrasov, S. M. Pshenichnikov, and N. P. Sopina, "Parametric conversion of infrared radiation in an $AgGaS_2$ crystal", Sov. J. Quantum Electron. **7**, 366–368 (1977).

[91] F. Rotermund, V. Petrov, and F. Noack, "Difference-frequency generation of intense femtosecond pulses in the mid-IR (4-12 μm) using $HgGa_2S_4$ and $AgGaS_2$", Opt. Commun. **185**, 177–183 (2000).

[92] E. C. Cheung, K. Koch, and G. T. Moore, "Silver thiogallate, singly resonant optical parametric oscillator pumped by a continuous-wave mode-locked Nd:YAG laser.", Opt. Lett. **19**, 631–633 (1994).

[93] T. Elsaesser, A. Seilmeier, W. Kaiser, P. Koidl, and G. Brandt, "Parametric generation of tunable picosecond pulses in the medium infrared using $AgGaS_2$ crystals", Appl. Phys. Lett. **44**, 383–385 (1984).

[94] L. Isaenko, I. Vasilyeva, A. Merkulov, A. Yelisseyev, and S. Lobanov, "Growth of new nonlinear crystals $LiMX_2$ (M=Al, In, Ga; X=S, Se, Te) for the mid-IR optics", J. Cryst. Growth **275**, 217–223 (2005).

[95] Y. Andreev, V. Atuchin, G. Lanskii, N. Pervukhina, V. Popov, and N. Trocenco, "Linear optical properties of $LiIn(S_{1-x}Se_x)_2$ crystals and tuning of phase matching conditions", Solid State Sci. **7**, 1188–1193 (2005).

[96] J.-J. Zondy, V. Vedenyapin, A. Yelisseyev, S. Lobanov, L. Isaenko, and V. Petrov, "$LiInSe_2$ nanosecond optical parametric oscillator", Opt. Lett. **30**, 2460–2462 (2005).

[97] V. Petrov, A. Yelisseyev, L. Isaenko, S. Lobanov, A. Titov, and J.-J. Zondy, "Second harmonic generation and optical parametric amplification in the mid-IR with orthorhombic biaxial crystals $LiGaS_2$ and $LiGaSe_2$", Appl. Phys. B **78**, 543–546 (2004).

[98] V. Kumar, M. Casella, E. Molotokaite, D. Polli, G. Cerullo, and M. Marangoni, "Coherent Raman spectroscopy with a fiber-format femtosecond oscillator", J. Raman Spectrosc. **43**, 662–667 (2012).

[99] M. Baumgartl, M. Chemnitz, C. Jauregui, T. Meyer, B. Dietzek, J. Popp, J. Limpert, and A. Tünnermann, "All-fiber laser source for CARS microscopy based on fiber optical parametric frequency conversion.", Opt. Express **20**, 4484–93 (2012).

[100] E. Ploetz, B. Marx, T. Klein, R. Huber, and P. Gilch, "A 75 MHz light source for femtosecond stimulated raman microscopy", Opt. Express **17**, 18612–18620 (2009).

[101] T. Walbaum, T. Hellwig, M. Schnack, and C. Fallnich, "Experimental realization of transverse mode conversion using optically induced transient long-period gratings", ArXiv:1308.3441v2 (2013).

[102] T. Hellwig, T. Walbaum, M. Schnack, and C. Fallnich, "Optically Induced Transverse Mode Conversion of Ultrashort-Pulses in Optical Waveguides", in *Nonlinear Optics*, NTh2A.5, (Optical Society of America, 2013).

[103] T. Hellwig, M. Schnack, T. Walbaum, S. Dobner, and C. Fallnich, "Experimental realization of transverse mode conversion using optically induced transient long-period gratings", in preparation for Opt. Lett. (2014).

[104] R. Faiman and K. Larsson, "Assignment of the CH stretching vibrational frequencies in the Raman spectra of lipids", J. Raman Spectrosc. **4**, 387–394 (1976).

[105] D. Wallach, S. Verma, and J. Fookson, "Application of laser Raman and infrared spectroscopy to the analysis of membrane structure", Biochim. Biophys. Acta. **559**, 153–208 (1979).

[106] P. C. Cross, J. Burnham, and P. A. Leighton, "The Raman spectrum and the structure of water", J. Am. Chem. Soc. **59**, 1134–1147 (1937).

[107] A. Owyoung, "Coherent Raman gain spectroscopy using CW laser sources", IEEE J. Quantum Elect. **14**, 192–203 (1978).

[108] R. F. Begley, A. B. Harvey, and R. L. Byer, "Coherent anti-Stokes Raman spectroscopy", Appl. Phys. Lett. **25**, 387–390 (1974).

[109] M. D. Duncan, J. Reintjes, and T. J. Manuccia, "Scanning coherent anti-Stokes Raman microscope", Opt. Lett. **7**, 350–352 (1982).

[110] J.-X. Cheng and X. S. Xie, "Coherent Anti-Stokes Raman Scattering Microscopy: Instrumentation, Theory, and Applications", J. Phys. Chem. B **108**, 827–840 (2004).

[111] E. T. Garbacik, J. L. Herek, and H. L. Offerhaus, "Rapid identification of heterogeneous mixture components with hyperspectral coherent anti-Stokes Raman scattering imaging", J. Raman Spectrosc. **43**, 651–655 (2012).

[112] B. Mallick, A. Lakhsmanna, and S. Umapathy, "Ultrafast Raman loss spectroscopy (URLS): instrumentation and principle", J. Raman Spectrosc. **42**, 1883–1890 (2011).

[113] D. Oron, N. Dudovich, and Y. Silberberg, "Femtosecond Phase-and-Polarization Control for Background-Free Coherent Anti-Stokes Raman Spectroscopy", Phys. Rev. Lett. **90**, 213902 1–3 (2003).

[114] J. Borysow, R. H. Taylor, and J. W. Keto, "Raman-Induced Kerr Effect Spectroscopy of Solutions", J. Raman Spectrosc. **20**, 203–208 (1989).

[115] D. W. McCamant, P. Kukura, and R. A. Mathies, "Femtosecond Time-Resolved Stimulated Raman Spectroscopy: Application to the Ultrafast Internal Conversion in beta-Carotene", J. Phys. Chem. A **107**, 8208–8214 (2003).

[116] D. W. McCamant, P. Kukura, and R. A. Mathies, "Femtosecond stimulated Raman study of excited-state evolution in bacteriorhodopsin", J. Phys. Chem. B **109**, 10449–10457 (2005).

[117] S. Shim and R. A. Mathies, "Development of a tunable femtosecond stimulated raman apparatus and its application to beta-carotene", J. Phys. Chem. B **112**, 4826–4832 (2008).

[118] H. L. Offerhaus, E. T. Garbacik, A. C. W. van Rhijn, A. L. Fussell, and J. L. Herek, "Phase aspects of (broadband) stimulated Raman scattering", Reviews in Analytical Chemistry **31**, 1–6 (2012).

[119] S. Dobner, C. Cleff, C. Fallnich, and P. Groß, "Interferometric background reduction for femtosecond stimulated Raman scattering loss spectroscopy", J. Chem. Phys. **137**, 174201 1–5 (2012).

[120] C. Wieman and T. W. Hänsch, "Doppler-Free Laser Polarization Spectroscopye", Phys. Rev. Lett. **36**, 1170–1173 (1976).

[121] G. Giraud, J. Karolin, and K. Wynne, "Low-frequency modes of peptides and globular proteins in solution observed by ultrafast OHD-RIKES spectroscopy.", Biophys. J. **85**, 1903–1913 (2003).

[122] V. Kumar, M. Casella, E. Molotokaite, D. Gatti, P. Kukura, C. Manzoni, D. Polli, M. Marangoni, and G. Cerullo, "Balanced-detection Raman-induced Kerr-effect spectroscopy", Phys. Rev. A **86**, 053810 1–7 (2012).

[123] B. G. Saar, C. W. Freudiger, J. Reichman, C. M. Stanley, G. R. Holtom, and X. S. Xie, "Video-rate molecular imaging in vivo with stimulated Raman scattering", Science **330**, 1368–1370 (2010).

[124] P. Groß, L. Kleinschmidt, S. Beer, C. Cleff, and C. Fallnich, "Single-laser light source for CARS microscopy based on soliton self-frequency shift in a microstructured fiber", Appl. Phys. B **101**, 167–172 (2010).

[125] Y. J. Chang, P. Cong, and J. D. Simon, "Optical heterodyne detection of impulsive stimulated Raman scattering in liquids", J. Phys. Chem. **99**, 7857–7859 (1995).

[126] E. O. Potma, C. L. Evans, and X. S. Xie, "Heterodyne coherent anti-Stokes Raman scattering (CARS) imaging", Opt. Lett. **31**, 241–243 (2006).

[127] B. Culshaw, "The optical fibre Sagnac interferometer: an overview of its principles and applications", Meas. Sci. Technol. **17**, R1–R16 (2006).

[128] K. U. Schreiber, T. Klügel, A. Velikoseltsev, W. Schlüter, G. E. Stedman, and J.-P. R. Wells, "The Large Ring Laser G for Continuous Earth Rotation Monitoring", Pure Appl. Geophys. **166**, 1485–1498 (2009).

[129] K. Sun, M. Fejer, E. Gustafson, and R. Byer, "Sagnac interferometer for gravitational-wave detection.", Phys. Rev. Lett. **76**, 3053–3056 (1996).

[130] R. Trebino and C. C. Hayden, "Antiresonant-ring transient spectroscopy", Opt. Lett. **16**, 493–495 (1991).

[131] M. C. Gabriel, N. A. Whitaker, C. W. Dirk, M. G. Kuzyk, and M. Thakur, "Measurement of ultrafast optical nonlinearities using a modified Sagnac interferometer", Opt. Lett. **16**, 1334–1336 (1991).

[132] N. Matsuda, R. Shimizu, Y. Mitsumori, H. Kosaka, and K. Edamatsu, "Observation of optical-fibre Kerr nonlinearity at the single-photon level", Nature Photon. **3**, 95–98 (2009).

[133] D. Zhang, M. N. Slipchenko, and J.-X. Cheng, "Highly Sensitive Vibrational Imaging by Femtosecond Pulse", J. Phys. Chem. Lett. **2**, 1248–1253 (2011).

[134] J. J. Song, G. L. Eesley, and M. D. Levenson, "Background suppression in coherent Raman spectroscopy", Appl. Phys. Lett. **29**, 567–569 (1976).

[135] M. J. Lagasse, D. Liu-Wong, J. G. Fujimoto, and H. A. Haus, "Ultrafast switching with a single-fiber interferometer", Opt. Lett. **14**, 311–313 (1989).

[136] M. A. van Dijk, M. Lippitz, D. Stolwijk, and M. Orrit, "A common-path interferometer for time-resolved and shot-noise-limited detection of single nanoparticles", Opt. Express **15**, 2273–2287 (2007).

[137] N. N. Akhmediev and A. Ankiewicz, *Soltions: Nonlinear Pulses and Beams*, (Chapman and Hall, London, 1997), first edition.

[138] R. C. Jones, "A New Calculus for the Treatment of Optical Systems", J. Opt. Soc. Am. **31**, 488 – 493 (1941).

[139] A. Gowen, C. Odonnell, P. Cullen, G. Downey, and J. Frias, "Hyperspectral imaging - an emerging process analytical tool for food quality and safety control", Trends Food Sci. Tech. **18**, 590–598 (2007).

[140] G. J. Puppels, F. F. M. de Mul, C. Otto, J. Greve, M. Robert-Nicoud, D. J. Arndt-Jovin, and T. M. Jovin, "Studying single living cells and chromosomes by confocal Raman microspectroscopy", Nature **347**, 301–303 (1990).

[141] M. Wall, A. Rechtsteiner, and L. Rocha, "Singular value decomposition and principal component analysis", in D. P. Berrar, W. Dubitzky, and M. Granzow, editors, *A Practical Approach to Microarray Data Analysis*, 91–109, (Kluwer, Norwell, MA, 2003).

[142] M. Miljković, T. Chernenko, M. J. Romeo, B. Bird, C. Matthäus, and M. Diem, "Label-free imaging of human cells: algorithms for image reconstruction of Raman hyperspectral datasets", Analyst **135**, 2002–2013 (2010).

[143] M. J. Everett, K. Schoenenberger, B. W. Colston, and L. B. Da Silva, "Birefringence characterization of biological tissue by use of optical coherence tomography", Opt. Lett. **23**, 228–230 (1998).

[144] M. Menke, V. Gerke, and C. Steinem, "Phosphatidylserine membrane domain clustering induced by annexin A2/S100A10 heterotetramer", Biochemistry **44**, 15296–15303 (2005).

[145] S. Dobner, P. Groß, and C. Fallnich, "In-line interferometric femtosecond stimulated Raman scattering spectroscopy", J. Chem. Phys. **138**, 244201 1–8 (2013).

[146] S. Dobner and C. Fallnich, "Hyperspectral imaging with in-line interferometric femtosecond stimulated Raman scattering spectroscopy.", J. Chem. Phys. **140**, 084201 1–6 (2014).

LIST OF PUBLICATIONS

JOURNALS

Publications relevant for this thesis

- S. Dobner and C. Fallnich, "Hyperspectral Imaging with In-Line Interferometric Femtosecond Stimulated Raman Scattering Spectroscopy", J. Chem. Phys. **140**, 084201 1-6 (2014).
- S. Dobner, P. Groß, and C. Fallnich, "In-line interferometric femtosecond stimulated Raman scattering spectroscopy", J. Chem. Phys. **138**, 244201 (2013).
- S. Dobner, C. Cleff, C. Fallnich, and P. Groß, "Interferometric background reduction for femtosecond stimulated Raman scattering loss spectroscopy", J. Chem. Phys. **137**, 174201 (2012).

Further publications

- T. Hellwig, M. Schnack, T. Walbaum, S. Dobner, and C. Fallnich, "Experimental realization of transverse mode conversion using optically induced transient long-period gratings", in preparation for Opt. Lett. (2014).
- S. Dobner, M. Höhl, N. M. Lüpken, and C. Fallnich, "Coherence-based axial point-spread function engineering for two-photon excited polymerization", published online first in Appl. Phys. B. (2014) DOI: 10.1007/s00340-014-5763-8.
- S. Dobner, N. Brauckmann, M. Kues, P. Groß, and C. Fallnich, "Broadband spectral shearing interferometry for amplitude and phase measurement of supercontinua", Appl. Phys. B **102**, 4 (2011).

CONFERENCE CONTRIBUTIONS (PEER-REVIEWED)

- S. Dobner, P. Groß, and C. Fallnich, "In-line interferometric Femtosecond Stimulated Raman Scattering Spectroscopy", Nonlinear Optics (NLO) NTh2B.5, Cohala Coast, Hawaii, USA (2013).
- S. Dobner, P. Groß, and C. Fallnich, "Cross-polarized Femtosecond Stimulated Raman Scattering", Conference on Lasers and Electro-Optics (CLEO Europe) CD42, München, Germany (2013).
- S. Dobner, C. Cleff, C. Fallnich, and P. Groß, "Interferometric femtosecond stimulated Raman scattering", Conference on Coherent Raman Scattering Microscopy (microCARS), Naurod, Germany (2012).
- S. Dobner, M. Kues, C. Cleff, C. Fallnich, and P. Groß, "Sagnac Interferometer for Background Reduction in Stimulated Raman Scattering Loss Specroscopy", Nonlinear Photonics NW1C.1, Colorado Springs, Colorado, USA (2012).
- C. Cleff, P. Groß, S. Dobner, C. Fallnich, H. L. Offerhaus, J. L. Herek, K. Kruse, W. P. Beeker, C. J. Lee, and K.-J. Boller, "Stimulated Emission Pumping Enabling Sub-Diffraction-Limited Spatial Resoution in CARS Microscopy", Nonlinear Photonics JM5A.14, Colorado Springs, Colorado, USA (2012).

CONFERENCE CONTRIBUTIONS (NON-PEER-REVIEWED)

- S. Dobner, C. Cleff, C. Fallnich, and P. Groß, "Interferometric Femtosecond Stimulated Raman Scattering", DPG Frühjahrstagung Q 37.2, Hannover, Germany (2013).
- S. Dobner, C. Cleff, P. Groß, and C. Fallnich, "Coherent Raman Scattering Spectroscopy", Advanced Optical Microscopy and Micromanipulation (AOMM), Münster, Germany (2013).
- S. Dobner, C. Cleff, P. Groß, and C. Fallnich, "Coherent Raman Scattering Light Sources", Advanced Optical Microscopy and Micromanipulation (AOMM), Münster, Germany (2013).
- P. Groß, C. Cleff, L. Kleinschmidt, J. Epping, S. Dobner, J. Brockhaus, and C. Fallnich, "Laserquellenentwicklung für CARS Mikroskopie", DPG Frühjahrstagung, Dresden, Germany (2011).
- S. Dobner, N. Brauckmann, M. Kues, P. Groß, and C. Fallnich, "SPIDER-Verfahren zur Charakterisierung von Superkontinua", DPG-Frühjahrstagung Q 48.2, Hannover, Germany (2010).